5-2021

Optical Linear and Optical and Magneto-Optical Nonlinear Effects in Plasmonic Nanostructures

Krishna Prasad Koirala
University of Tennessee, Knoxville, kkoiral2@vols.utk.edu

To the Graduate Council:

I am submitting herewith a dissertation written by Krishna Prasad Koirala entitled "Optical Linear and Optical and Magneto-Optical Nonlinear Effects in Plasmonic Nanostructures." I have examined the final electronic copy of this dissertation for form and content and recommend that it be accepted in partial fulfillment of the requirements for the degree of Doctor of Philosophy, with a major in Physics.

Hanno Weitering, Major Professor

We have read this dissertation and recommend its acceptance:

Gerd Duscher, Ramki Kalyanaraman, Marianne Breinig, Jian Liu, Tatiana Allen

Accepted for the Council:

Dixie L. Thompson

Vice Provost and Dean of the Graduate School

(Original signatures are on file with official student records.)

Optical Linear and Optical and Magneto-Optical Nonlinear Effects in Plasmonic Nanostructures

A Dissertation Presented for the

Doctor of Philosophy

Degree

The University of Tennessee, Knoxville

Krishna Prasad Koirala

May 2021

Dedicated to all who lost their lives to COVID-19

Acknowledgments

First and foremost, I would like to express my sincere gratitude to my advisors Dr. Gerd Duscher and Dr. Ramki Kalyanaraman for giving me the opportunity to work with them. For me, it was a great privilege to conduct my research at the University of Tennessee, Knoxville. I am deeply grateful to Dr. Gerd for the inspiration, motivation and valuable suggestion during experimentation, analyzing data and writing articles. He was a source to regain my lost confidence, with increased interest towards research at the middle of this journey. For his kindness, I will forever remain indebted to him. I greatly appreciate Dr. Ramki for his support and the generosity to share his lab, knowledge and experience even when he was not available on-site. I truly appreciate the time he gave to me to discuss the research work. I would also like to express my eternal gratitude to Dr. Hanno Weitering for agreeing to chair my PhD committee and providing support directly and indirectly throughout my graduate studies. I would like to thank my PhD committee members Dr. Marianne Breinig, Dr. Jian Liu and Dr. Tatiana Allen for their support and suggestions.

I immensely appreciate the opportunity provided by Dr. Dayakar Penumadu to characterize carbon fibers which help me to gain more experience in focused ion beam and scanning transmission electron microscopy-electron energy loss spectroscopy. Besides, I thank Dr. John Dunlop for training me electron and atomic force microscopy, sputtering, Dr. Michael Kohler for training X-ray diffraction, and Dr. Matthew F Chisholm for giving me the access to microscopy facilities at Oak Ridge National Lab (ORNL). I am very much thankful to current and past group members VP Sandireddy, Chenze Liu and Humaira Taz for their continuous help in the lab.

In addition, I want to sincerely thank all my collaborators for their cooperation:

- Hernando Garcia at Southern Illinois University-Edwardsville
- James Penner-Hahn and Aniruddha Deb at the University of Michigan-Ann Arbor
- Tatiana Allen and her students at the University of Tennessee-Chattanooga

Finally, I would like to thank my family for their endless love and belief in me. With the greatest thanks to my wife, Rubi Bhattarai Koirala, for her unconditional love, care, encouragement and giving me the biggest blessing of my life -my beautiful daughter, Adriana Koirala.

Abstract

The linear optical, and nonlinear optical and magneto-optical properties of plasmonic nanostructures offer important guidelines for designing nanoscale all-optical and quantum optical devices with ultra-fast response time. This dissertation work presents the study of those properties in Ag, FeAg and CoAg metallic nanostructures. While UV-Vis-NIR spectroscopy and modified Z-scan techniques were used to study the linear and nonlinear properties, electron energy-loss spectroscopy performed in scanning transmission electron microscopy mode was employed to investigate and evaluate those properties. This work also present the synthesis techniques of those nanostructures. The Ag and Co-Ag nanoparticles were synthesized by pulsed laser melting of thin films while Fe-Ag bimetallic arrays were fabricated by nanosphere lithography techniques. Near-spherical Ag nanoparticles were synthesized by Ultra Violet (UV) laser dewetting of Ag thin films under a glycerol fluid environment. Under a single 9 nanosecond laser pulse irradiation of the particles in air, the particles were changed into a near-hemispherical shape. The resulting changes in particle contact area and volume fraction in the dielectric media resulted in substantial shift in the wavelength and intensity of the dipolar and quadrupolar LSPR modes to the violet side of the visible spectrum. Fe-Ag bimetallic hexagonally ordered nanopyramidal arrays showed the giant negative nonlinear refraction and nonlinear Faraday rotation at telecommunication wavelength of 1550 nm. Further, the nonlinear response was dependent on the degree of overlap of the Fe nanopyramid on the Ag nanopyramid which influenced the strength of plasmon induced dipoles on the Ag nanopyramid. The analysis of optical spectra and electron energy loss spectra of Co-Ag nanoparticles led to detection of localized surface plasmons at the interface of two metals ever observed from bimetallic nanoparticles. These investigations

and findings generally advance the science of plasmonic nanostructures towards optical, magneto-optical and quantum-optical based applications.

Table of Contents

List of Tables

List of Figures

Chapter 1

Introduction

Plasmonics focuses on the interaction between electromagnetic waves (such as light) and valance electrons (plasma) in bulk, at surfaces, and at defects. Research in plasmonic nanostructures has led to devices with unique, and often unexpected optical/magneto-optical properties. For instance, plasmonic properties in metallic nanostructures can be finely tuned by changing the dielectric environment or dimensions of nanostructures [16]. These properties are exploited in molecular or chemical sensing because plasmons cause a very strong optical response. More exotic optical effects can be achieved with plasmonic meta-materials or wave-guides. Most interestingly, plasmonics offers a wide range of applications in any field which demands enhanced control and interaction of photons, such as in beam shaping, single bio-molecule detection, hot-electron and spin currents generation. With development of atomic scale fabrication and characterization techniques such as electron energy-loss spectroscopy, applications like lasing, optical cloaking and optical communications are on the horizon [17, 18, 19, 20, 21]. Nonlinear plasmonics is a new research area with a lot of promises in ultra-fast optical communications and quantum-information processing.

The work presented in this dissertation focuses on the effects of plasmonics in linear and nonlinear domains. In the linear optical domain, plasmonics demands active control of plasmon-induced resonant optical behavior. The existing technologies that modulate the plasmon-induced resonant wavelength are based on changing the dielectric environment or employing active dielectric substrates. This dissertation work presents for the first time

the reversible plasmonic resonance properties on a plasmonically passive substrate (fused quartz). Interestingly, this plasmon-induced reversible resonant wavelength was achieved by contact angle tuning of Ag nanoparticles with nanosecond *single* laser pulse. In addition to this, an analysis of electron energy-loss spectra and optical absorption spectra in a bimetallic plasmonic system is presented. This study has led to the direct detection of localized surface plasmons at metallic interface. This work was mainly motivated by enhanced plasmonic properties in bimetallic systems reported recently [22, 23]. In the nonlinear domain, the dissertation work focuses on the development of cost-effective novel bimetallic nano-arrays for application in technologically important wavelengths such as telecommunication wavelengths (1530-1570 nm). The enhanced nonlinear effects of plasmonic system have generally been reported at fundamental resonant wavelength which falls in visible or near infra-red regions (400 nm-1200 nm) in the case of Ag or Au nanostructures [24]. Here we aim to utilize the effect of two-photons absorption generally reported for semiconductors to enhance the nonlinearity at the energy of one photon. This dissertation work successfully presents a model system exhibiting *simultaneous* and extraordinarily large third-order refractive indices and photo-induced (nonlinear) Faraday rotation from Fe-Ag arrays at the telecommunication wavelength of 1550 nm mediated by plasmonic effects. We also put emphasis on quantitative analysis of electron energy-loss spectra to compare the plasmon-induced effects. In general, this dissertation work enriches the linear and nonlinear optical/magneto-optical regimens with plasmon-induced effects necessary for sensing, all-optical switching and quantum-optical information processing.

The plasmon-induced optical properties of metallic nanoparticles have been exploited for thousands of years. The classic example is the famous Lycurgus cup from the Roman era, which effectively displays a multitude of colors due to size-dependent optical properties of gold nanoparticles [25]. However, the systematic study of plasmonics can be traced back to as early as 1857 when Michael Faraday studied the optical properties of metallic colloids [26]. The study was further advanced by Gustav Mie who investigated the simulation of color effects created with gold particles using classical Maxwell equations [27]. However, the rediscovery of plasmons in a variety of contexts has clearly pushed the existing theory to the limit and points towards the interlinked nature of many phenomena and applications

in plasmonic [28, 29, 30, 31]. Based on the origin of plasma oscillations, the family of plasma oscillations can be divided into three parts: volume (bulk) plasmon, surface plasmon polariton and localized surface plasmon.

- **Volume plasmon**

  A volume (bulk) plasma oscillation is a coherent motion of electron gas density excited longitudinally (parallel to propagation direction). The frequency of these oscillations (in the $\mathbf{k} \sim 0$) is called plasma frequency and is given by $\omega_p = \sqrt{Ne^2/(\epsilon_0.m^*)}$. It depends on the volume density of conduction electrons (N), the electronic charge(e), the dielectric constant in vacuum (ϵ_0) and the effective mass of the electrons (m^*) [32]. The bulk plasma frequency is flat in $\mathbf{k}$ as shown in Figure 1.1(a). The Jellium model which is a quantum mechanical description, provides a good approximation to plasmon oscillation. According to it, the electrons in metal oscillate about the positive metal ion cores due to Coulomb interaction. The model treats the discrete positive nuclei in metals as continuous immobile positive charges in space and individual electron interacting via a screened Coulomb potential. The existence of bulk plasmon modes in thin films has experimentally been verified by electron energy-loss spectroscopy (EELS) [2, 33, 34].

- **Surface plasmon polariton (SPP)**

  Surface plasmon modes are lower energy modes than bulk modes supported by metal surfaces. The surface breaks transnational invariance which supports a plasmon mode normal to the surface as shown in Figure 1.1(b). In general, this mode can not couple with light due to momentum mismatch. However, it is possible to provide necessary momentum by a grating or using evanescent mode of light. The resulting mode is called surface plasmon polariton and has application in wave guiding and surface sensitive sensors [35, 36].

- **Localized surface plasmon (LSP)**

  LSP is a coherent and collective oscillation of free-electron gas density *confined* in a nanoparticle. The schematic illustration of LSP is shown in Figure 1.1(c). For the nanoparticles with size smaller than 20 nm, the problem can be effectively solved by

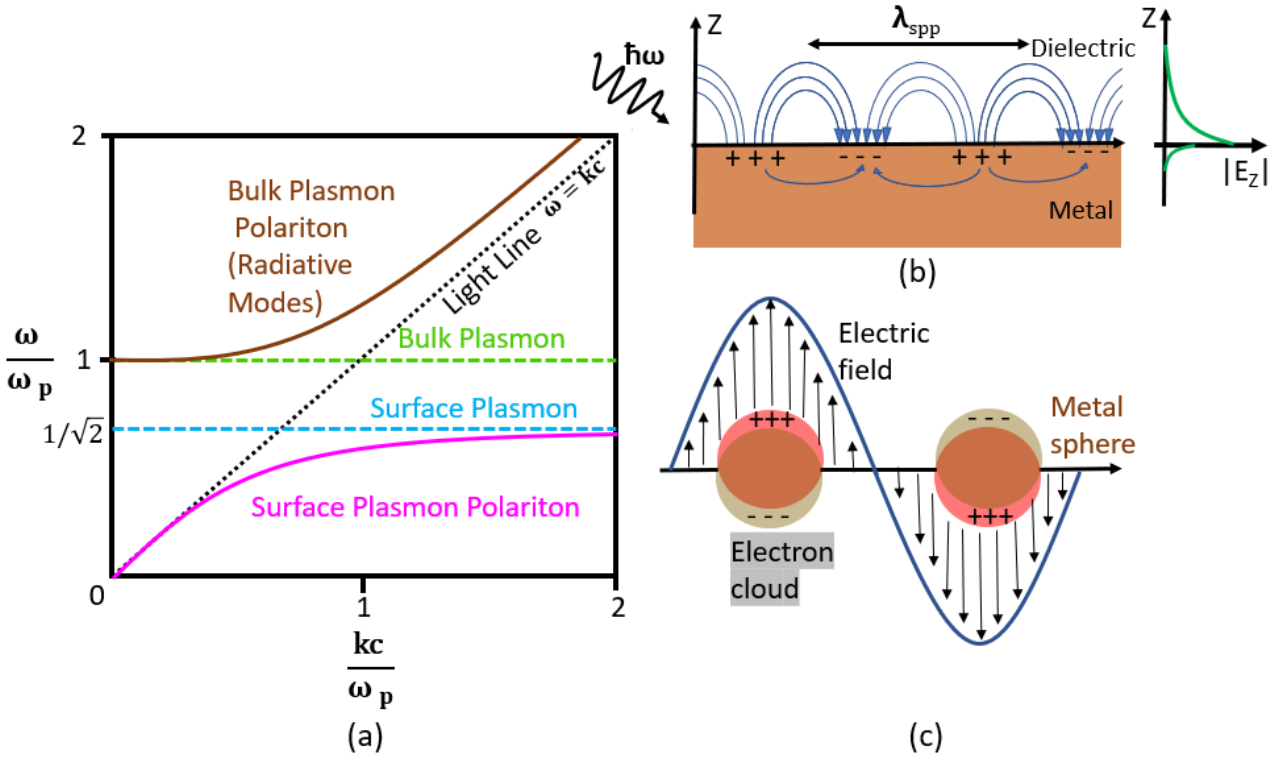

Figure 1.1: (a) Dispersion relations of plasmonic modes (b) Surface plasmon polaritons at the interface of a metallic thin film and a dielectric (c) Localized surface plasmon in a metallic nanosphere. Image adapted from [2]

the quasi-static approximation because the electric field phase can be assumed constant over the particles. However, the practically interested metallic nanoparticles are not always of deep subwavelength sizes. The LSP resonant behavior of such particles is sensitive to the refractive index (RI) of the surrounding medium, composition of the metal, and the geometrical features of the particle such as it's shape and aspect ratio [13, 28, 37, 38, 39]. The LSP induced tunable optical properties are suitable for a variety of applications from sensing, lasing, imaging to optical fibers [40, 41, 42, 43, 44, 45, 46, 47, 48, 49, 50, 51, 52].

This dissertation work mainly focuses on the study of LSP induced optical/magneto-optical properties of metallic nanostructures in both linear and nonlinear domains. A brief account on how the local environment and geometrical attributes of the nanostructures affect LSP resonance frequency is presented below.

- **Factors affecting LSP resonance wavelength in plasmonic nanostructures**

  The derivations in this section are adapted from Willets and Van Duyne [12]. The Mie theory gives the analytical solution of optical properties of metallic nanoparticles by solving Maxwell equations [27]. Within the limitation of spherical nanoparticle of radius r $\sim 0.1\lambda$, the extinction (absorption+scattering) cross-section of the nanoparticle ca be written as,

$$\sigma_{ext}(\lambda) = \frac{18\pi V \epsilon_{med}^{3/2}}{\lambda} \times \frac{\epsilon_{im}(\omega)}{\left[\epsilon_{re}(\omega) + G\epsilon_{med}\right]^2 + \left(\epsilon_{im}(\omega)\right)^2} \tag{1.1}$$

  where, V, ϵ_{re}, ϵ_{im}, ϵ_{med} are volume of the nanoparticle, real part of the dielectric function of metal, imaginary part of the dielectric function of metal and dielectric function of the surrounding medium respectively. G is the geometrical factor and equal to 2 for spherical nanoparticles. Considering the behavior of conduction band electrons as quasi-free particles, the dielectric response of these electrons in incident oscillating electromagnetic field of frequency ω is well described by Drude model [53] as,

$$\epsilon(\omega) = \epsilon_{re}(\omega) + i.\epsilon_{im}(\omega) = \epsilon_{core} - \frac{\omega_p^2}{\omega^2 + \tau^2} + i.\frac{\omega_p^2.\tau}{\omega.(\omega^2 + \tau^2)} \tag{1.2}$$

where, ω_p and τ are plasma frequency and collision (damping) frequency respectively. The size dependent collision frequency is expressed as,

$$\tau(r) = \tau_\infty + \frac{Mv_f}{2r} \tag{1.3}$$

with bulk relaxation frequency τ_∞, M is multiplying factor (for spherical particle M =2), and v_f is Fermi velocity. Also, the plasma frequency, $\omega_p = \sqrt{Ne^2/(\epsilon_0.m^*)}$ depends on the volume density of conduction electrons (N), the electronic charge(e), the dielectric constant in vacuum (ϵ_0) and the 'effective mass' of the electrons (m^*) [32]. The localized surface plasmon resonance (LSPR) occurs when extinction cross-section is maximized, i.e. $\epsilon_{re} = -2\epsilon_{med}$.

Accordingly [54],

$$\omega_{LSPR} = \frac{\omega_p}{\sqrt{2\epsilon_{med} + 1}} \tag{1.4}$$

or,

$$\lambda_{LSPR} = \lambda_p\sqrt{2\epsilon_{med} + 1} \tag{1.5}$$

For the particles with different shapes (other than spherical) with depolarization factor (L),

$$\lambda_{LSPR} = \lambda_p\sqrt{2\epsilon_\infty + (\frac{1}{L} - 1)\epsilon_{med}} \tag{1.6}$$

Where, ϵ_∞ is the high frequency contribution to the metal dielectric function. This gives an overall perspective of LSPR frequency control of metal nanoparticles. The $\omega_p = \sqrt{Ne^2/(\epsilon_0.m^*)}$ is affected by size, shape, composition of metals or alloys nanoparticles through n and m^*, while ϵ_{med} is affected by the surrounding medium. Further, the nanoparticles are also sensitive to interparticle separation enabling different resonance modes, Fano resonance and spectral splitting, to name a few [55, 56]. For the nanoparticles with dipolar coupling, the gap dependent plasmonic shift can be written as,

$$\frac{\Delta\lambda}{\lambda_{LSPR}} = Ae^{\frac{-d}{2r\Gamma}} \tag{1.7}$$

where, A is maximum fractional shift (coupling strength), d is particle separation, r is radius of particles and Γ is decay length of the electric field away from the particle surface.

The above discussion gives a general idea of LSPR behavior in plasmonic nanoparticles. I specifically discuss what magnitude of those effects is observed in Silver (Ag) nanostructures in the following paragraph.

- **LSPR quality in Ag nanostructures**

  The LSPR quality of metallic nanostructures which determines their applicability is limited by two important parameters namely resonance frequency (ω_{LSPR}) and quality factor, which is defined as $Q = \frac{\omega d \epsilon_{re}}{2\epsilon_{im}} = \frac{\omega_{LSPR}}{2\Delta\omega}$. There are only a handful of metals which showed resonance frequency in important visible wavelengths and good quality factors. These metals are Ag and Au. A comparison of resonant frequency and size and shape independent quality factor ($Q = \frac{\omega d \epsilon_{re}}{2\epsilon_{im}}$) of Ag and Au are shown in Figure 1.2. It is evident that the Ag has an extremely larger quality factor than Au metal nanostructures in visible and near-infrared regions. It has been reported that the optical cross-section of Ag is four times larger than Au [57].

Linear optical properties of plasmonic nanostructures

Strong light-matter interaction due to large scattering/absorption cross-section in plasmonic nanostructures generates unique linear optical properties. The attributes that describe the linear optical properties of the material are absorbance, transmittance, extinction coefficient, and refractive index. Ag nanostructures show unusual plasmon induced linear optical properties influenced by the factor described above. The refractive index dependent of LSPR wavelength for spherical Ag nanoparticle are shown in Figure 1.3. Further, extinction, absorption and scattering spectra obtained for Ag nanostructures with different geometrical features are presented in Figure 1.4.

These tunable linear optical properties dependent on encompassing matrix and geometrical attributes of plasmonic nanostructures have a significant impact on nonlinear optical

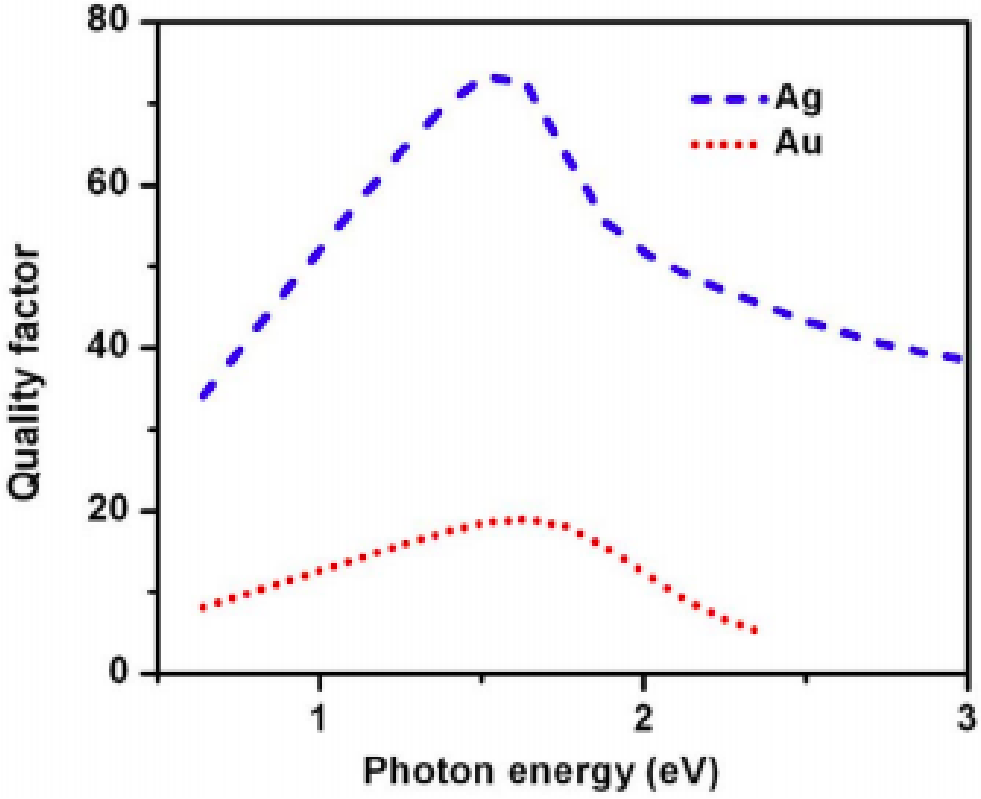

Figure 1.2: Shape independent quality factor versus resonance frequency for plasmon resonances in Ag and Au metals. Image from [3]. Copyright [3]

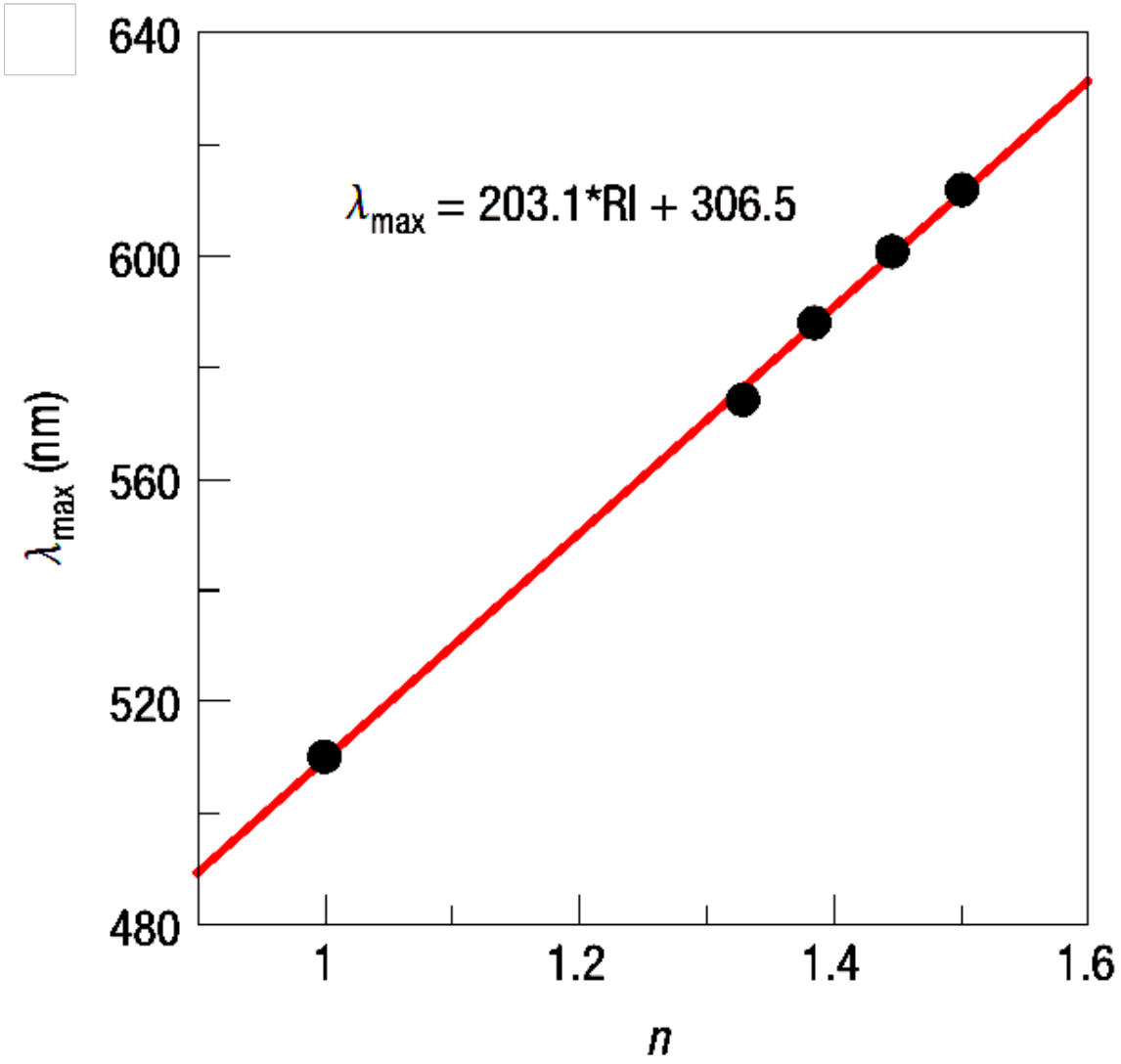

Figure 1.3: Plot showing the linear relationship between the surrounding refractive index n and the LSPR λ_{LSPR} of Ag spherical nanoparticles. Image from [4]. Copyright [4]

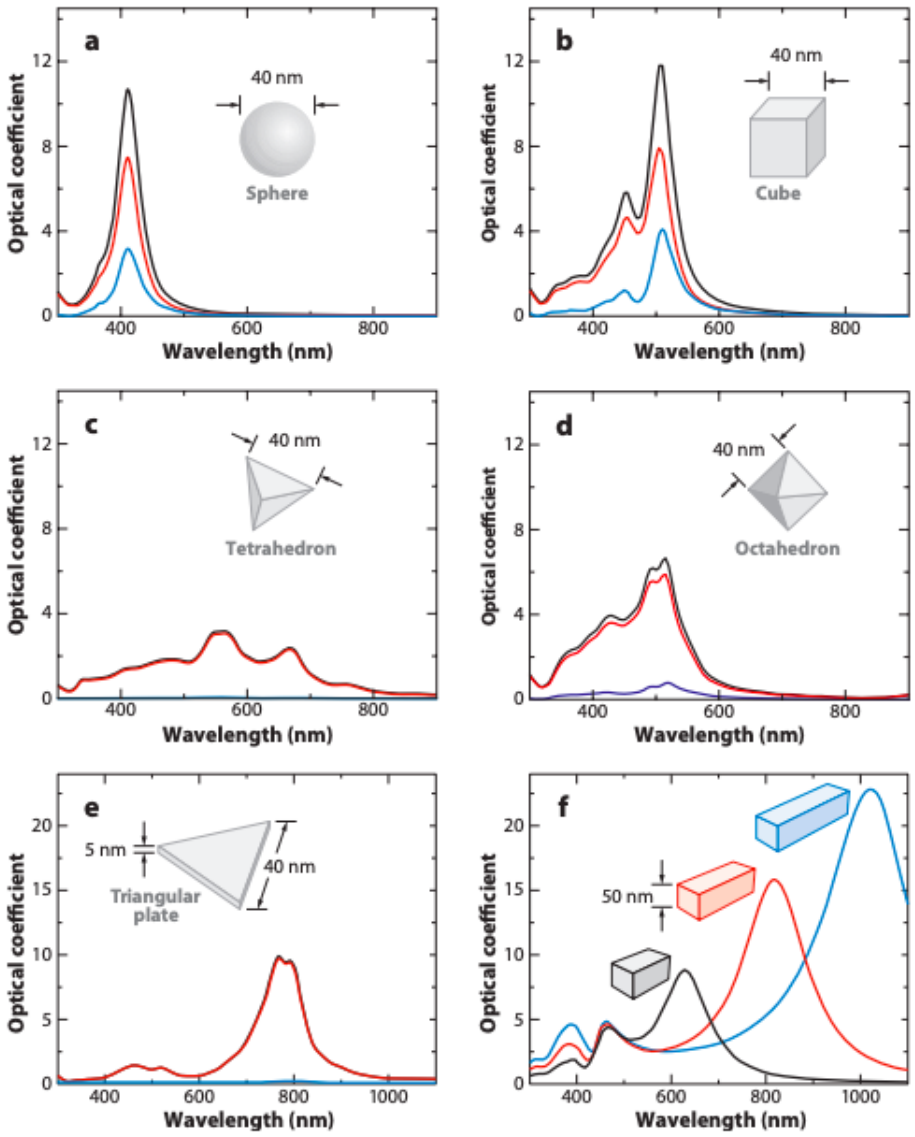

Figure 1.4: "Extinction (black), absorption (red), and scattering (blue) spectra calculated for Ag nanoparticles of different shapes: (a) a sphere (b) a cube, (c) a tetrahedron, (d) an octahedron, and (e) a triangular plate. (f) Extinction spectra of rectangular bars with aspect ratios of 2 (black), 3 (red), and 4 (blue)" [5]. Image from [5, 6, 7]. Copyright [5, 6, 7]

behavior. This behavior generally arises due to local field enhancement. In the following subsection, I discuss optical nonlinearity in plasmonic nanostructures.

Nonlinear optical properties of plasmonic nanostructures

The plasmonic nanostructures manipulate the incident electromagnetic field which enhances the various nonlinear phenomena to the plasmonic nanostructures themselves or the other media near their vicinity. There are two ways of contribution towards the nonlinearity of plasmonic nanostructures [24, 58]

- due to local field enhancement at the fundamental frequency
- coupling of outgoing nonlinear signal to radiative LSP modes or manipulation of local interference between various nonlinear sources

The simplest model to understand the plasmonic nanostructures is a nanosphere which has been extensively studied with regards to optical nonlinearity. The contributions to the second harmonic generation (SHG) of nanospheres are generally attributed to surface and bulk terms. However in noble metal, due to symmetry (centrosymmetry), the bulk contribution is forbidden. The SHG in plasmonic nanoparticles can only be due to a surface term where symmetry breaking occurs. Another important factor contributing to nonlinearity is geometrical ordering which affects the circular dichroism in SHG due to geometrical chirality. It has been demonstrated that the chiral G-shaped gold particles exhibits a strong SHG-circular dichroism (CD) effect attributed to enatiomerically sensitive plasmon modes, with strongest signal at fundamental wavelength of plasmonic resonance [58, 59]. Recently, large third order nonlinear refraction (four orders of magnitude larger than in silica) has been reported from gold meta-surface at off-resonant wavelength of 1550 nm [60] . This behavior was attributed to the morphology of the metasurface which arises due to collective interaction between the nanospheres.

Nonlinear magneto-optical properties of plasmonic nanostructures

Magneto-plasmonic nanostructures are generally composed of noble metals and ferromagnetic metals/alloys and plasmonic and magnetic properties coexist. Magneto-plasmonic

nanostructures show very unique magneto-optical properties generally due to spectral overlap of plasmonic transition and magneto-optical transition [61]. The magneto-optical properties of such systems are generally studied in two modes: in reflection mode as magneto-optical Kerr effect (MOKE) and in transmission mode as Faraday or Voigt effect. The change in magneto-optical response from the system arises due to the influence of the magnetic field in the effective dielectric permittivity of the system. Plasmon-enhanced magneto-optical Faraday rotation has been demonstrated in a number of magneto-plasmonic systems such as gold-coated γ-Fe_2O_3, core-shell Co-Ag nanoparticles, a colloidal solution of spinel ferrite and Ag amongst others [62, 63, 64]. Nonlinear Magneto-Plasmonic (NMP) systems are generally studied as nonlinear MOKE which arises due to nonlinear plasmonic and magnetic plasmonic properties. The most often studied nonlinear effect is magnetic second harmonic generation (MSHG) which contains magnetic components of the second-order nonlinear susceptibility tensor. For a system with magnetization M induced spontaneously or due to an external magnetic field, the second-order nonlinear polarization is [65]

$$P_{NL}(2\omega) = \epsilon_0 \chi^{el} E(\omega) E(\omega) \pm \epsilon_0 \chi^{mag}(\pm M) E(\omega) E(\omega) \tag{1.8}$$

Here the magnetic contribution to second harmonic generation is described by the last term in Eq. 1.8 and the total MSHG signal is given by

$$I_{2\omega} = (P_{NL}(2\omega))^2 \tag{1.9}$$

To the best of my knowledge, no nonlinear Faraday process has been studied in magneto-plasmonic structures at telecommunication wavelength of 1550 nm

While plasmonic nanostructures exhibit rich set of optical and magneto-optical properties due to strong enhanced light-matter interaction, in the following section, I will briefly discuss the theoretical aspect of optical and magneto-optical properties of solid material in linear and nonlinear regimen.

1.1 Optical and magneto-optical properties in solid

The optical and magneto-optical properties of a material tell how it interacts with incident electro-magnetic fields and are dependent on compositions, structures, and symmetry of the material and its constituents. These properties are generally measured in terms of frequency dependence reflectance, absorbance and polarization rotation. The most important material property which describes the electronic and optical nature of the material is its dielectric function. It also allows for a comparison of response of materials on interaction with photons, electrons and their fields. In the macroscopic limit, the interaction of material with electric and magnetic fields of incident electro-magnetic waves are described by Maxwell's equations [66, 67]. They are,

$$\nabla \cdot \mathbf{E} = 4\pi\rho^{total} \tag{1.10}$$

$$\nabla \times \mathbf{E} = \frac{-1}{c}\frac{\partial \mathbf{B}}{\partial t} \tag{1.11}$$

$$\nabla \cdot \mathbf{B} = 0 \tag{1.12}$$

$$\nabla \times \mathbf{B} = \frac{1}{c}\frac{\partial \mathbf{E}}{\partial t} + \frac{4\pi}{c}\mathbf{J}^{total} \tag{1.13}$$

Here, $\mathbf{E}$ and $\mathbf{B}$ are electric and magnetic fields respectively; ρ^{total} and $\mathbf{J}^{total}$ are total charge and current densities respectively. The fields are macroscopic here. Further, total charge density can be expressed as $\rho^{total} = \rho^{free} + \rho^{bound} = \rho^{ext} + \rho^{bound}$, while total current density can be expressed as sum of free and bound current densities $\mathbf{J}^{total} = \mathbf{J}^{free} + \mathbf{J}^{bound} = \mathbf{J}^{cond} + \mathbf{J}^{ext} + \mathbf{J}^{bound}$. By introducing the properties of medium with polarization ($\mathbf{P}$)- electric dipole moment per unit volume and magnetization ($\mathbf{M}$)-magnetic dipole moment per unit volume, we get

$$\rho^{bound} = \rho^{pol} = -\nabla.\mathbf{P} \tag{1.14}$$

and,

$$\mathbf{J}^{bound} = \mathbf{J}^{pol} + \mathbf{J}^{Mag} = \frac{\partial \mathbf{P}}{\partial t} + c\nabla \times \mathbf{M} \tag{1.15}$$

1.1.1 Optical properties of linear optical medium

Within the linear approximation,

$$\mathbf{P} = \chi_E \mathbf{E} \tag{1.16}$$

$$\mathbf{M} = \chi_M \mathbf{H} \tag{1.17}$$

$$\mathbf{J}^{cond} = \sigma \mathbf{E} \tag{1.18}$$

$$\mathbf{D} = \epsilon E \tag{1.19}$$

$$\mathbf{B} = \mu \mathbf{H} \tag{1.20}$$

Here, $\chi_E, \chi_M, \sigma, \epsilon$ and μ are the electric susceptibility, magnetic susceptibility, conductivity (optical), dielectric function and magnetic permeability of the medium. Using vector identity in isotropic medium with no external charge sources ($\rho^{ext} = 0$), we can readily derive the wave equation as,

$$\nabla^2 \mathbf{E} = \frac{\epsilon\mu}{c^2}\frac{\partial^2 \mathbf{E}}{\partial t^2} + \frac{4\pi\sigma\mu}{c^2}\frac{\partial \mathbf{E}}{\partial t} \tag{1.21}$$

For the single plane wave solution as the optical experiments are generally performed with monochromatic light,

$$\mathbf{E} = \mathbf{E}_0 e^{i(\hat{\mathbf{q}}\cdot\mathbf{r} - \omega t)} \tag{1.22}$$

Where $\hat{\mathbf{q}}$ is a complex propagation constant and ω is the frequency of the light. The real and imaginary parts of $\hat{\mathbf{q}}$ represent wave vector and the attenuation of wave inside the solid respectively [68]. From Eq. 1.21 and Eq. 1.22,

$$\hat{q}^2 = \mu\frac{\omega^2}{c^2}(\epsilon + i\frac{4\pi\sigma}{\omega}) \tag{1.23}$$

and, in terms of complex refractive index (with attenuation), $\hat{\mathbf{q}}$ can be expressed as,

$$\hat{q} = (\frac{\omega}{c})\hat{n} = (\frac{\omega}{c})(n + ik) \tag{1.24}$$

Here n is the index of refraction and k is the extinction coefficient. Substituting Eq. 1.24 in Eq. 1.22 and defining the absorption coefficient (α) as fractional change in intensity, we get

$$\alpha = -\frac{1}{E^2}\frac{dE^2}{dr} = 2\omega k/c = 4\pi k/\lambda \tag{1.25}$$

Also from Eq. 1.23 and Eq. 1.24, and defining complex dielectric function $\hat{\epsilon}$ as $\epsilon_{re} + i\epsilon_{im}$, we get the famous Kramers-Kronig dispersion relation [69] as,

$$\epsilon_{re} = (n^2 - k^2)/\mu \tag{1.26}$$

$$\epsilon_{im} = 2nk/\mu = 4\pi\sigma/\omega \tag{1.27}$$

Considering the behavior of conduction band electrons as quasi-free particles, the dielectric response of these electrons in incident oscillating electromagnetic field of frequency ω is well described by Drude model [53] as,

$$\epsilon(\omega) = \epsilon_{re}(\omega) + i.\epsilon_{im}(\omega) = \epsilon_{core} - \frac{\omega_p^2}{\omega^2 + \tau^2} + i.\frac{\omega_p^2.\tau}{\omega.(\omega^2 + \tau^2)} \tag{1.28}$$

where, ω_p and τ are plasma frequency and collision (damping) frequency respectively. Also, the plasma frequency, $\omega_p = \sqrt{4\pi Ne^2/(m^*\epsilon_{core})}$ which is a characteristic frequency at which the material changes from a metallic to dielectric, depends on the volume density of conduction electrons (N), the electronic charge(e), the dielectric constant in vacuum (ϵ_{core}) and the 'effective mass' of the electrons (m^*) [32]. It should be noted that the real part of dielectric function at plasma frequency vanishes. The condition for the existence for plasma frequency is $\epsilon_{core} > \frac{4\pi ne^2\tau^2}{m^*}$. A band diagram for the noble metals are shown in Figure 1.5. Since d bands lie well below the Fermi level, at low energy, only intraband transition of "conduction electrons" are possible. The medium-brown color arrow in the left shows transition of d band electrons to conduction band formed by hybridized outer s and p band. The red arrow in left and right show for intra-band transition. When the photon energy is lower than the Debye energy ($\hbar\omega_D$), a simultaneous absorption of a phonon occurs to satisfy

momentum conservation as shown in right arrows. On the left side, the absorption of a photon results in either absorption or emission of a phonon.

The reflectivity of solids at normal incidence is

$$R = \frac{(n-1)^2 + k^2}{(n+1)^2 + k^2} \tag{1.29}$$

Also, the intensity of light in absorbing media after traversing the distance x is

$$I = I_0(1-R)e^{-\alpha x} \tag{1.30}$$

where α is absorption coefficient.

1.1.2 Optical properties of nonlinear optical medium

The concept of nonlinear optics was first introduced when the second harmonic generation (SHG) was discovered by Franken et. al. in 1961 [70]. At high intensity, light-matter interaction led the changes in the macroscopic properties (polarization, reflection, absorption and susceptibility) as a function of interacting intensity. The nonlinear response of an optical medium can be described by the power series expansion of the polarization of the medium in terms of the incident electric field. The propagation of electromagnetic wave and electric field ($\mathbf{E}$) dependent polarization ($\mathbf{P}$) of a nonlinear system can be expressed as [67]

$$\nabla^2\mathbf{E} - \frac{\epsilon\mu}{c^2}\frac{\partial^2\mathbf{E}}{\partial t^2} = \frac{4\pi}{c^2}\frac{\partial\mathbf{P}}{\partial t} \tag{1.31}$$

$$\mathbf{P} = \epsilon_0\chi_E^{(1)}\mathbf{E} + \mathbf{P_{NL}} = \epsilon_0(\chi_E^{(1)}\mathbf{E} + \chi_{EE}^{(2)}\mathbf{EE} + \chi_{EEE}^{(3)}\mathbf{EEE} + \chi_{EEEE}^{(4)}\mathbf{EEEE} + ...) \tag{1.32}$$

where, $\chi^{(i)}(i$=1,2,3...) is the i^{th} order susceptibility and is described by $(i+1)^{th}$ rank tensor. However, for homogeneous and isotropic materials such as noble metals, they can be expressed in terms of scalar quantities.

Second-order nonlinear process

For the incident electromagnetic field consisting of two superimposed monochromatic waves, the electric field is expressed [71] as

$$\mathbf{E} = \mathbf{E_1} e^{i\omega_1 t} + \mathbf{E_2} e^{i\omega_2 t} + cc \tag{1.33}$$

Here, ω_1 and ω_2 are frequencies of two interacting waves. In nonlinear wave mixing, more than one nonlinear processes present in the light-matter interaction simultaneously. However, the desired nonlinear signal can be enhanced by decreasing the other nonlinear processes through phase matching condition in nonlinear polarization. The second-order nonlinear optical processes in terms of polarization are described as follows:

- **second harmonic generation (SHG):** photons with the same frequency interact to generate a new photon with twice the energy of incident photons

$$\mathbf{P^{(2)}}(\mathbf{2}\omega_\mathbf{1}) = \epsilon_0 \chi^{(2)}_{E_1 E_1} \mathbf{E_1 E_1} \tag{1.34}$$

$$\mathbf{P^{(2)}}(\mathbf{2}\omega_\mathbf{2}) = \epsilon_0 \chi^{(2)}_{E_2 E_2} \mathbf{E_2 E_2} \tag{1.35}$$

- **sum frequency generation (SFG):** photons with different frequencies annihilate to produce the third photon

$$\mathbf{P^{(2)}}(\omega_\mathbf{1} + \omega_\mathbf{2}) = 2\epsilon_0 \chi^{(2)}_{E_1 E_2} \mathbf{E_1 E_2} \tag{1.36}$$

- **difference frequency generation (DFG):** photons with different frequencies annihilates in conjugation way. Unlike other process, it produces photons with a new frequency as well as fundamental frequencies. One of the examples is optical parametric amplification (OPA).

$$\mathbf{P^{(2)}}(\omega_\mathbf{1} - \omega_\mathbf{2}) = 2\epsilon_0 \chi^{(2)}_{E_2 E_2^*} \mathbf{E_1 E_2^*} \tag{1.37}$$

- **optical rectification (OR):** quasi-static polarization

$$\mathbf{P^{(2)}}(\omega_\mathbf{1} - \omega_\mathbf{2}) = 2\epsilon_0 \chi^{(2)}_{E_1 E_2}(\mathbf{E_1 E_1^*} + \mathbf{E_2 E_2^*}) \tag{1.38}$$

Third order nonlinear process

In general, the third-order nonlinear process is a four-wave mixing process where three waves mix and generate a fourth wave at the same time. In this process, we can observe several nonlinear processes like THG, SFSHG, DFSHG, DFSFG, and NFG. Here I focus on the intensity-dependent refractive index and nonlinear absorption (two-photon absorption process) process, which is the technique used in this dissertation work. Within the dipolar approximation for centrosymmetric material, the second-order process vanishes and hence,

$$\epsilon = \epsilon_0[\chi_E^{(1)} + 3\chi^{(3)}_{EEE}|E|^2] \tag{1.39}$$

or

$$n = n_0 + n_2 I \tag{1.40}$$

Here n_2 is defined in terms of sum of the real part of the third order electronic susceptibilities $\chi^{(3)}(-\omega : \omega, \omega, -\omega) + \chi^{(3)}(-\omega : \omega, -\omega, \omega) + \chi^{(3)}(-\omega : -\omega, \omega, \omega)$. The schematic of transition between ground state and excited state is shown in Figure 1.6.

The intensity dependent process which is ultrafast leads to many important phenomena required for all-optical signal processing. They are

- **Self phase modulation (SPM):** Due to varying refractive index with intensity, ultrafast pulses traversing the medium produces the phase shift of $\phi = (n_0 + n_2 I).L_{eff}.\frac{2\pi}{\lambda}$. Self phase modulation produces a nonlinear phase shift of $\phi_{SPM} = n_2 I.L_{eff}.\frac{2\pi}{\lambda}$. This effect can be observed by spectral broadening/optical soliton.
- **Cross phase modulation (XPM):** When two or more signals having different frequencies are transmitted simultaneously from optical media, the nonlinear phase evolution of the one signal depends also on the intensity of the other signals which is called cross phase modulation. The nonlinear phase shift of signal A is given

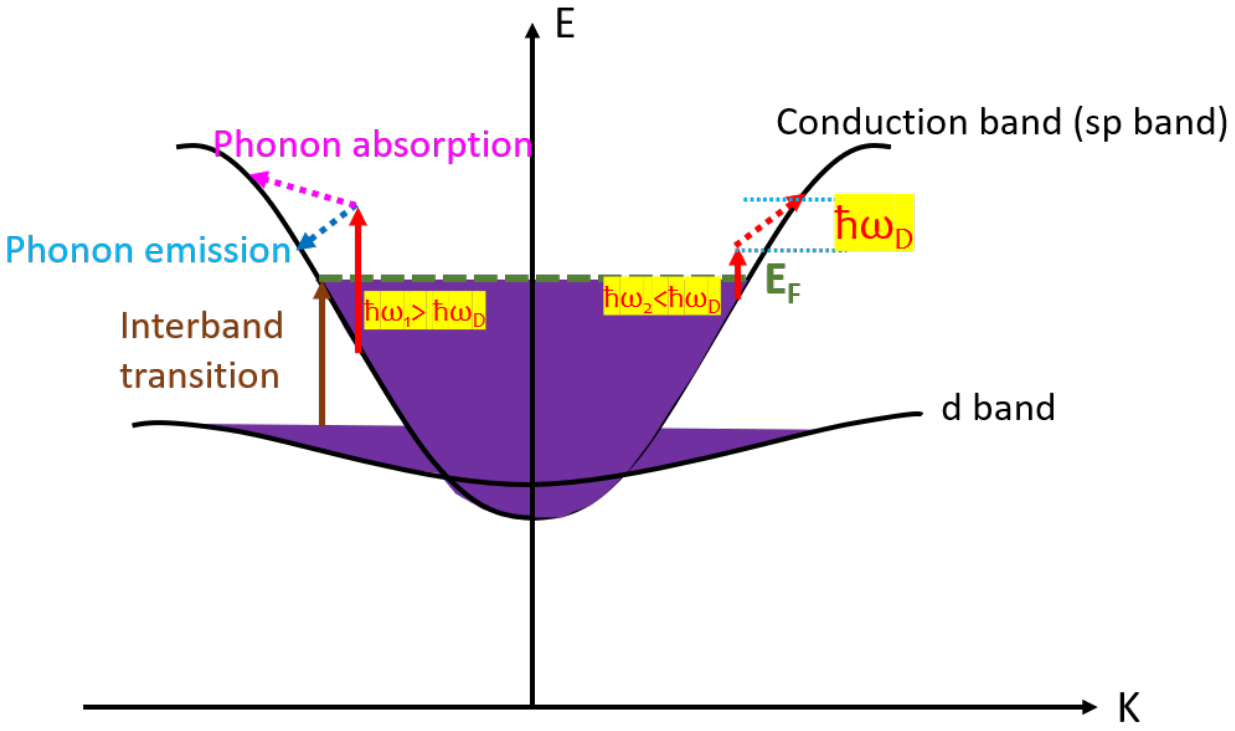

Figure 1.5: Schematic band diagram for a noble metal. $\hbar\omega_D$ is Debye energy.

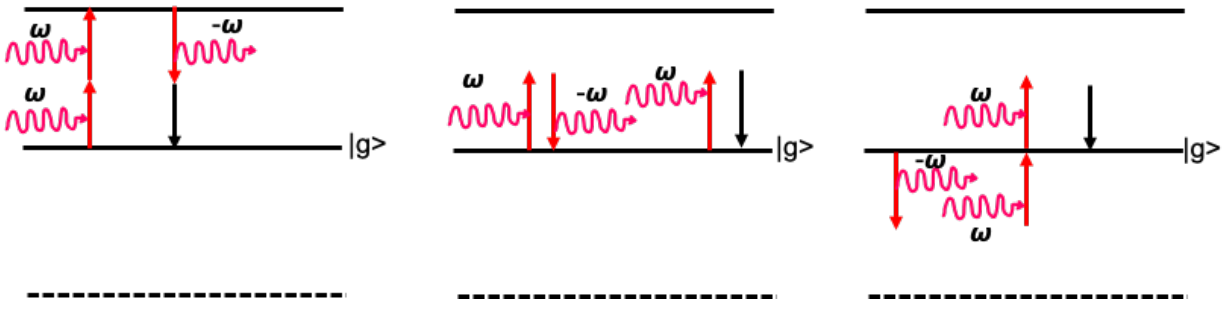

Figure 1.6: Schematic of transition diagrams for $\chi^{(3)}(-\omega : \omega, \omega, -\omega), \chi^{(3)}(-\omega : \omega, -\omega, \omega) and \chi^{(3)}(-\omega : -\omega, \omega, \omega)$ respectively (from left to right)

by $\phi^A_{XPM} = n_2 I^B . L_{eff} . \frac{2\pi}{\lambda}$, where I^B is the intensity of the signal B. It gives to pulse compression of ultrafast pulses and has application in quantum nondemolition measurement, optical demultiplexing, wavelength conversion amongst others.

1.1.3 Linear and Nonlinear magneto-optical medium

The well-known magneto-optical effects like Kerr rotation in reflection mode and Faraday rotation in transmission mode arise due to magnetization of the medium where time reversal symmetry breaks. The dielectric permittivity of a material system in magnetic field (due to ferromagnetic material or due to external magnetic field) can be expressed [67] as

$$\epsilon = \begin{bmatrix} \epsilon'_{xx} & \epsilon'_{xy} + ig_z & \epsilon'_{xz} - ig_y \\ \epsilon'_{xy} - ig_z & \epsilon'_{yy} & \epsilon'_{yz} + ig_x \\ \epsilon'_{xz} + ig_y & \epsilon'_{yz} - ig_x & \epsilon'_{zz} \end{bmatrix}$$

Then the relation between displacement field and electric field can equivalently be expressed as,

$$\mathbf{D} = \epsilon \mathbf{E} = \epsilon' \mathbf{E} + i\mathbf{E} \times \mathbf{g} \tag{1.41}$$

Here $\mathbf{g}$ is pseudo vector called gyration vector and can be expressed as

$$\mathbf{g} = \epsilon_0 \chi_{\mathbf{M}} \mathbf{H} \tag{1.42}$$

where $\chi_{\mathbf{M}}$ is magneto-optical susceptibility of the medium. Inserting the equation 1.41 in plane wave equation (obtained using vector identity in Maxwell's equations),

$$\nabla \times \nabla \times \mathbf{E} = -\frac{1}{c^2} \frac{\partial^2 \mathbf{D}}{\partial t^2} \tag{1.43}$$

Then the wave equation becomes

$$n^2[\hat{e} - \hat{q}(\hat{q}.\hat{e})] - n_0^2 \hat{e} + i(\hat{e} \times \mathbf{g}) = 0 \tag{1.44}$$

or,

$$(\hat{q} \pm \frac{\mathbf{g}}{2n_0})^2 = n_0^2 \tag{1.45}$$

With complex propagation vector $\hat{q} = (\frac{\omega}{c})\ \hat{n}$, The refractive indices with right and left circularly polarized light is finally expressed as

$$n_\pm^2 = n_0^2 \pm \mathbf{g} \tag{1.46}$$

In linear regime, the polarization rotation of linearly polarized light is expressed [67] as,

$$\theta_F = \frac{\omega L}{2c}[n_- - n_+] \tag{1.47}$$

For a photoinduced process, where the refractive indices are dependent on the intensity of incident light, following equation 1.40, the right and left refractive indices can be expressed as, $\tilde{n}_+ = n_+ + n_{2+}I$ and $\tilde{n}_- = n_- + n_{2-}I$. Then, polarization angle becomes,

$$\tilde{\theta}_F = \frac{\omega L}{2c}[\tilde{n}_- - \tilde{n}_+] = \frac{\omega L}{2c}[\Delta n + \Delta n_2 I] = \theta_F + \theta_2 I = \theta_F + \theta_{NL} \tag{1.48}$$

Here $\theta_{NL} = \theta_2 I$ is photo induced modification of rotation angle. This is the phenomenological consideration and can be derived by microscopic quantum mechanical consideration. For the medium without magnetic field, the relation between polarization of media with incident electric field and magnetic field from electromagnetic wave can be expressed as

$$\mathbf{P} = \epsilon_0(\chi_E^{(1)}\mathbf{E} + \chi_{E'}^{(1)}\dot{\mathbf{B}} + \chi_{EE}^{(2)}\mathbf{EE} + \chi_{E'E'}^{(2)}\mathbf{E\dot{B}} + \chi_{EEE}^{(3)}\mathbf{EEE} + \chi_{E'E'E'}^{(3)}\mathbf{EE\dot{B}} + \chi_{EEEE}^{(4)}\mathbf{EEEE} + ...) \tag{1.49}$$

and with applied magnetic field $\mathbf{H}$,

$$\mathbf{P} = \epsilon_0(\chi_E^{(1)}\mathbf{E} + \chi_{EE}^{(2)}\mathbf{EE} + \chi_{EH}^{(2)}\mathbf{EH} + \chi_{EEE}^{(3)}\mathbf{EEE} + \chi_{EEH}^{(3)}\mathbf{EEH} + \chi_{EEEE}^{(4)}\mathbf{EEEE} + \chi_{EEEH}^{(4)}\mathbf{EEEH}...) \tag{1.50}$$

1.1.4 Nonlinearity at telecommunication wavelengths

All-optical signal processing is one of the effective ways to overcome the physical limits of electronics (where the data transfer is limited by mobility of electrons) in telecommunications. However, the linear optics doesn't allow for light to light alteration. Therefore, large and ultrafast optical and magneto-optical nonlinearity is very much desired for optical communication functionalities like all-optical switching, optical isolation, pulse limiting, multiplexing, demultiplexing, high sensitive magnetometry and quantum information processing [72, 73, 74, 75, 76, 77, 78, 79, 80, 81]. The wavelength-dependent optical and magneto-optical properties of metal nanostructures are an area of active research due to a variety of potential applications. One area of particular interest is their nonlinear optical (NLO) and nonlinear magneto-optical (NLMO) properties at or near the telecommunication wavelengths (such as between 1530 nm -1570 nm), that result from utilizing suitably engineered materials design [82, 83, 84]. Silicon has been considered to be a promising material for all-optical logic at telecommunication wavelength due to its linear optical transparency and a large nonlinear refractive index of $n_2 = 4{\times}10^{-5}$ cm^2/GW. However, its ultimate performance is limited by a weak nonlinear figure of merit of $F = 0.35$ defined by $F = \frac{n_2}{\beta\lambda}$, where β is the nonlinear absorption coefficient and λ is the wavelength of the incident light [85]. Graphene has also been regarded as a promising material due to the very high n_2 of 102 cm^2/GW at the telecommunication wavelength. However, it is unlikely to address the current demand of high-performance optical devices due to the challenges with making high-quality graphene for mass production as well as its zero bandgap which results in broadband optical absorption [86]. Many other 2D materials have been proposed for all-optical devices, including hexagonal boron nitride (h-BN), metal oxides, perovskites and metal dichalcogenides [87, 88, 89, 90, 91, 92, 93, 94]. Despite exciting advances, outstanding challenges remain in the large-area-growth of low defect materials along with intrinsic materials limitations, such as a Faraday rotation limited by the cyclotron frequency of the system. The current state-of-the-art in the field of strong Faraday rotators at telecommunication wavelengths are based on linear response of bulk synthetic materials and solely driven by yttrium iron garnet (YIG) [95]. Nonlinear Faraday

properties have been generally investigated for cold atoms and atomic vapors at or near the laser wavelengths (energies) of their hyperfine transition energies regions, and for some dilute magnetic semiconductors like CdMnTe at or near their optical band gap energies, which are far from the telecommunication wavelength [80, 96, 97]. To the best of our knowledge, the nonlinear Faraday process has not been studied on any material systems at or near the telecommunication wavelengths. Partially motivated by these limitations and the many unusual plasmonic and magneto-plasmonic properties of metallic nanostructures that have been discovered recently, there is continuing interest among the nonlinear optics and magneto-optics community to explore plasmonic nanostructures at the important 1550 nm [98, 99, 100, 101, 102].

1.2 Synthesis of plasmonic nanostructures

There are many techniques used in synthesis of plasmonic nanostructures. Based on fundamental methodologies, these can be categorized into two- (i) Bottom-up approach and (ii)Top-down approach.

Bottom-up approach

Bottom-up approach is a spontaneous organization in which pattern formation occurs due to the system approaching equilibrium due to reduction in free energy. On surfaces, the methods for bottom-up approach are generally chemical synthesis, self-assembly and self-organization methods.

- **Chemical synthesis:** It is an old, simple and cost-effective route for nanostructure synthesis compared to lithography. The basic mechanism involving these techniques is to start from metal-containing complexes which are dissolved in solvent. The metal ions are reduced into neutral metal atoms by reducing agents contained in the solvent. Then, metal nuclei form as the reaction progresses. The size of the nuclei is determined by the amount and concentration of reducing agent while the stability is maintained by using capping agents. For example, spherical Ag nanoparticles can be obtained

by reduction of $AgNO_3$ using ascorbic acid as reducing agent and citrate as stabilizer [103].

- **Self-assembly:** Self-assembly is a simple and cost-effective method for producing an ensemble of nanoparticles [8]. Self-assembly is spontaneous process. This method is also possible for producing directionality and long-range ordering in ensembles by controlling the alignment of nanoparticles [104, 105]. A schematic and SEM image of the self-assembly process is shown in Figure 1.7. In this process, first, capped metal nanoparticles are dissolved in an organic solvent. As the solvent evaporates, capped nanoparticles are brought together due to intermolecular forces.

- **Self-organization:** Self-organization is also an inexpensive method compared to lithography techniques. Examples of self-organization processes are pulsed laser melting/dewetting of thin films. Melted metal films self-organize into nanoparticles without external driving forces [106]. Self-organization is a non-equilibrium process. The structures of Ag thin film showing self-organization processes is shown in Figure 1.8.

Top-down approach

Top-down approach is lithography techniques where resists and masks are used to define patterns. It generally begins with a pattern generated on a larger scale and then reduced to nanoscale.

- **Photolithography** The most used top-down approach is photolithography. In this process, light is used to transfer a geometric pattern to a photosensitive chemical photoresist on the substrate. The schematic process of photolithography is shown in Figure 1.9.

- **Electron beam lithography** In this process, the energetics electrons are used to draw required shapes on a surface which covered with electron-resist [107]. Here the electron beam changes the solubility of the resist through the mask which enables the

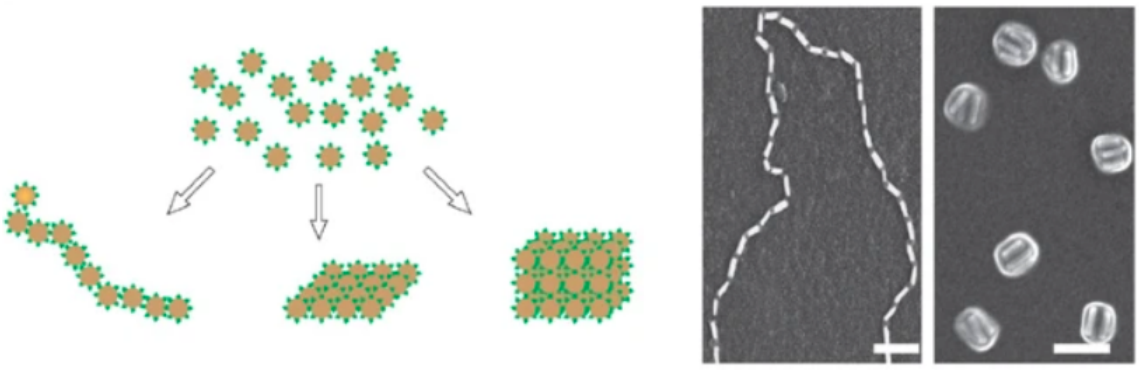

Figure 1.7: (Left)Schematic image showing the organization of nanoparticles in chains, 2D sheets and 3D structures. (Right) Scanning electron microscope images of self-assembled gold nano rods into chain and side-to-side aggregated bundles. The scale bar is 100 nm. Image from [8, 9]. Copyright [8, 9]

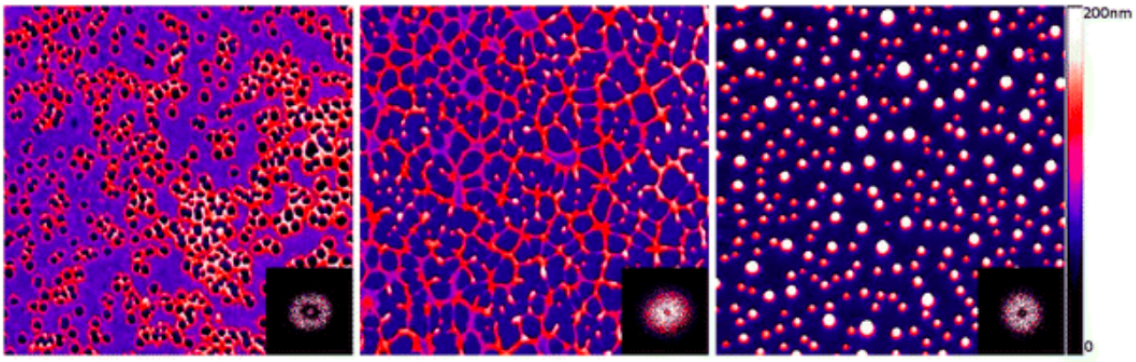

Figure 1.8: The evolution of morphologies after pulsed laser-induced spontaneous dewetting and self-organization of an thin Ag metal film on SiO_2 substrates: irradiation with laser of T(left) 10 pulses (middle) 1,000 pulses, (right) 10,000 pulses. Image from [10]

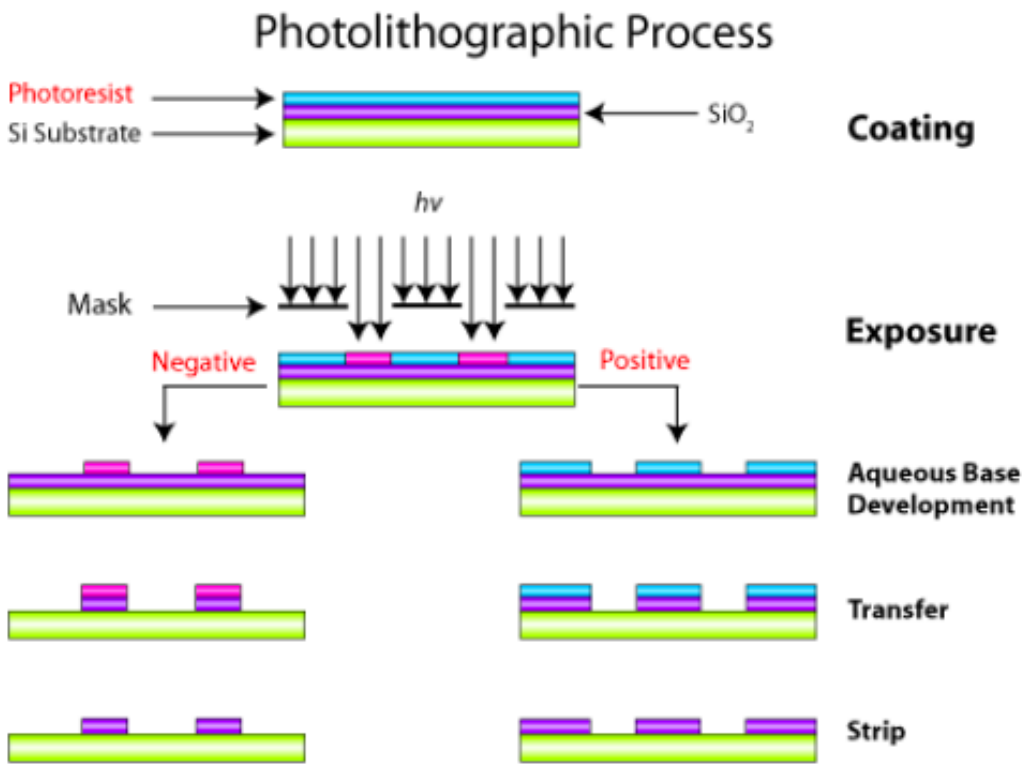

Figure 1.9: Photolithographic process: photoresist solution (generally polymer) is coated onto a flat substrate. Then this photoresist is exposed to light through a mask. The photoresist undergoes a chemical reaction induced by light. In the case of a positive photoresist, the irradiated parts break down and become more soluble than the unexposed regions. In a negative photoresist, light-induced photochemical crosslinking of the photoresist, which renders the exposed regions insoluble in the developer. Image from [11]. Copyright [11]

removal of either exposed or unexposed parts depending on whether the resistor is positive or negative respectively.

- **Ion-beam lithography** Like electron beam lithography uses electrons and photolithography uses photons, in ion-beam lithography, the energetic ions are used to fabricate custom nanostructures. Generally, Gallium ions are used due to their large atomic mass which enhances the effect of sputtering.

- **Nanosphere lithography** Nanosphere lithography is an inexpensive fabrication technique compared to other lithography techniques. It creates hexagonal and controlled nanopyramidal of different sizes. In this process, first, the mask is prepared on the desired surface which is a monolayer of polystyrene beads. Second, the desired metal is deposited onto masked substrates. Finally, the hexagonal arrays of metallic nanopyramidal structures are obtained by chemical etch out (generally, sonication in ethanol) of polystyrene beads. A schematic of the procedure is shown in Figure 1.10.

1.3 Scope of this dissertation work

This dissertation work resulted in a discovery of a model system which exhibits an extraordinarily large nonlinear optical and magneto-optical effects at the telecommunication wavelength of 1550 nm. About three orders larger in nonlinear refractive index and four orders larger in nonlinear figure of merit than typically reported for metallic nanoparticles as well as six orders larger in magneto-optical susceptibility than dilute magnetic semiconductor at the telecommunication wavelength of 1550 nm was observed [83, 96, 108, 109, 110]. This discovery is unique because it is the first demonstration of a single material exhibiting such a combination of enormous nonlinear optical and magneto-optical effects. Detailed experimental studies using optical and electron energy-loss studies via scanning transmission electron microscopy established the effect that the behaviors are mediated by matching of two photon resonance conditions and a synergistic behavior between Fe and Ag nanopyramids arising via plasmonic effects. The direct consequence of this discovery could be to revolutionize external field control of "plasmon-spin-photon" interaction from a single system

and its optimization for all-optical, magneto-optical and quantum information processing. Aside from this work, the analysis of linear optical properties from bimetallic nanoparticles and a work demonstrating a mechanism showing a tunable optical response from plasmonic nanoparticles on plasmonically passive substrates will also be discussed. The experimental data collected from state-of-the-art electron microscopes as well as nonlinear spectroscopies used in this work were used to discuss the results and draw conclusions.

Plasmonic or hybrid-plasmonic nanostructures exhibit interesting linear optical/magneto-optical properties [111, 112, 113]. These properties are suitable for various applications such as sensing, energy harvesting, optical/magneto-optical communication, catalysis amongst others [4, 114, 115, 116, 117]. These applications are based on resonant interaction of incident electromagnetic fields (either from photons or swift electrons) with free electron gas of the nanostructures called surface plasmon resonance (SPR). When nanostructure size is comparable to or smaller than wavelength of light, the free electron gas on the surface of nanostructures exhibit locally confined oscillation and the specific oscillation frequency is called localized surface plasmon resonance (LSPR) frequency. In case of plasmonic metals also called noble metals (Ag, Au, Cu), LSPR can be tuned from visible to near infra-red region either by changing the nanostructures geometry or by altering dielectric environment. Also, in order to tune plasmon mediated optical and magneto-optical properties, noble metals have been integrated with other materials like Fe, Co, Ni, which have also shown to exhibit improved activity and stability [22, 23]. To shed further light on enhanced LSPR behavior from bimetallic nanoparticles reported previously [23], this dissertation work details the analysis of CoAg bimetallic nanoparticles with better energy (0.15 eV) and spatial (1.8 Å) resolution obtained for the nanoparticles with a higher degree of crystallinity. With those improved experimentation, we reported the direct detection of the interface *localized* surface plasmons in bimetallic interface which was suggested (theoretically) to exist about sixty years ago [31, 118].

Another important field of study in plasmonics is active plasmonics which modulates the LSPR characteristics such as resonance wavelength and intensity in a fast time scale. In noble (plasmonic) metal nanostructures, this can be achieved by changing the dielectric properties, modifying the charge carrier density, and spacing between the nanoscale materials. For

example, the refractive indices of dye molecules have been altered within the time scale of a few seconds under exposure by a HeCd laser with subsequent LSPR shift from the supporting Au nanorods of $\sim$ 20 nm in the visible wavelength [119]. Phase-change materials like Germanium Antimony Telluride (Ge_3Sb_2Te6) have shown to offer reversible refractive index response to femtosecond pulsed laser heating with $\sim$ 1000 nm shift in the resonance wavelength in the mid-infrared regime, as seen with Au or Al plasmonics rods [120, 121]. Changing the gap between nearby plasmonic nanoparticles has been demonstrated with negatively charged Au nanoparticles covered with bis(p- sulfonatophenyl)-phenylphosphine and plasmonic shifts of $\sim$ 50 nm in visible range have been achieved in the time scale of a few seconds [122]. Graphene has recently been realized as a tunable plasmonic media due to electrically-controllable charged carrier density but appears to be limited to switching in the millisecond to second time scales due to RC phase delay [123]. The common nature of these previously reported research works is that the modulation of LSPR was obtained either by changing the dielectric environment or interacting with active dielectric substrate. The modern LSPR based sensor could demand the plasmonic nanoparticles with modulating LSPR properties in plasmonically passive substrates like quartz to detect the maximum sensitivity of the interacting system in desired wavelength in ultrafast response time. This dissertation work has presented the first time the *reversible* plasmonic resonance properties on plasmonically passive substrate (fused quartz) based on contact angle tuning of Ag metal nanoparticles with heating from nano-second laser pulses.

While linear optical properties of plasmonic nanostructures have been investigated for a long time in great detail, in recent years, their responses in nonlinear domains are of particular interest. [124, 125, 126, 127, 128]. It is because nonlinear behaviors of a material system driven by plasmonic properties could overcome the limitation observed in photonic and nanoelectronic materials. Particularly, the plasmonic materials could process optical signals in ultra-fast response time unlike in photonic materials which are limited by diffraction of light and in nanoelectronic which are limited by mobility of electrons. However, the plasmonic materials exhibiting exciting nonlinear optical properties in important wavelengths such as telecommunication wavelength (1530 nm - 1570 nm) has rarely been reported [129]. Carefully engineered plasmonic metal nanostructures with strong nonlinear optical properties

in desired wavelengths could provide a fascinating platform opening up the application in all-optical communication. Mediated by plasmon induced near field confinement, nonlinear plasmonic nanomaterials possess ability to process signals at high speed fulfilling demand for high-data-rates, broader bandwidths, low power consumption, and denser on-chip integrability in telecommunication wavelengths [130, 131, 132, 133]. In addition, the current research has paid much attention to induce optical nonlinearity and optically generate spin waves via interaction of resonant plasmonic materials with ferromagnetic material arising from inverse Faraday effect [134, 135, 136]. These materials possess ability to produce ultra-short magnetic field pulses near their vicinity. However, if one finds a nanomaterial system exhibiting *simultaneous* enormous nonlinear optical and nonlinear Faraday properties and mediated by plasmonics, it opens up an avenue for ultra-fast optical switching of nonlinear magnetism in nanometer scale. This material could also possess unparalleled ability to process complex magneto-optical signals necessity for more efficient quantum computing circuits as it offers both phase and polarization degrees of freedom. To the best of our knowledge, such material/s have never been reported. Initially motivated by this concept, based on the result and analysis of this dissertation work, we now offer a model system of extraordinarily large nonlinear optical and nonlinear Faraday properties from bimetallic nano arrays mediated by plasmonic effects (evaluated by STEM-EELS) at the telecommunication wavelength of 1550 nm. These observed effects on a single system could also contribute fundamentally in the field of new techniques which provide a bridge for the burgeoning fields of nonlinear plasmonics and nonlinear spintronics at technologically important wavelengths.

1.4 Outline of this dissertation

In order to understand the linear and nonlinear properties of plasmonic nanostructures, a systematic evaluation of plasmonic nanostructures by means of photons and electrons sources is performed.

Chapter 2: Experimental methods and techniques

In this chapter, I describe the various experimental methods and characterization techniques with a brief information of the instruments used, employed for the research tasks performed for this dissertation work.

Chapter 3: Detection of localized plasmons in interfaces from bimetallic nanoparticles by STEM-EELS

This chapter covers the observation of localized plasmons in the interface of bimetallic nanostructures. The excitation of those types of plasmonic nanostructures by means of optical sources and electrons beam and their effect on the observed properties will be discussed. In a previous study, our group reported an observation of electron-energy loss peak when a monochromatic electron beam passes near the Co side of CoAg bimetallic nanoparticles. This electron-energy loss behavior was attributed to excitation of "ferroplasmons" [23]. However, the origin of such plasmons was not determined to our satisfaction. The primary reason was due to insufficient spatial and energy resolution of the instruments. In this work, we present a detailed analysis of CoAg bimetallic nanoparticles with better energy (0.15 eV) and spatial (1.8 Å) resolution obtained for nanoparticles with a higher degree of crystallinity. With these improved experimental conditions, we now report the observation of localized interface plasmons from metal-metal interfaces in CoAg bimetallic nanoparticles by means of scanning transmission electron microscopy - electron energy-loss spectroscopy (STEM-EELS).

Chapter 4: Switchable LSPR by resettable contact angle in nanostructure

In this work, we introduce a new approach to reversible switching of plasmonic behavior in the UV-visible regime within nanosecond timescales through contact angle tuning of silver nanoparticles. Our idea relies on the change in resonance wavelength and intensity of the dipolar and quadrupolar plasmonic modes when nanoparticles change their contact area and volume fraction within a dielectric. Using the dynamic form of the Maxwell-Garnett (M-G) effective medium theory [137], we first show that changing an array of

Ag nanoparticles between spherical to hemispherical shape, while keeping the individual nanoparticle volume conserved leads to a substantial shift in the resonance wavelengths and intensities. Specifically, the plasmonic resonance wavelengths redshift while the intensity ratio of the quadrupole to dipole resonances decreases in going from the spherical to hemispherical shape. The magnitude of these changes depends upon the particle size and volume fraction in the dielectric media consisting of the quartz contact surface and surrounding air. Recently, it was experimentally demonstrated by Prasad et al [138] that it is possible to change the contact angle of Ag nanoparticles by nanosecond pulsed laser irradiation in various fluid ambient like air, water, and glycerol. Here, we have used a glycerol environment to first synthesize near-spherical shaped Ag nanoparticle arrays using UV pulsed laser irradiation. Subsequent irradiation in air produced near-hemispherical particle arrays and resulting changes in the optical plasmonic behavior. We have also investigated the resetting behavior and the ability to switch between the two states over multiple cycles. We begin first by presenting the key ideas based on the dynamic M-G theory. This is followed by details of the experimental technique and subsequently the detailed results, analysis and conclusions.

Chapter 5: Nonlinear optical and magneto-optical properties in bimetallic arrays

This chapter covers the nonlinear optical and magneto-optical properties of Fe-Ag nanostructures in telecommunication wavelength of 1550 nm. We will discuss the observation of giant nonlinearity in those nanostructures and potential origin. There is a pressing need to discover magneto-optical materials and devices with better performance and lower cost that operate at telecommunication wavelengths. Here we report the discovery of giant negative nonlinear refraction and nonlinear Faraday rotation at 1550 nm using an array of bimetallic Fe-Ag nanopyramids. This system exhibited a very large third-order nonlinear refractive index (n_2 = -2.32 cm^2 /GW) and nonlinear figure of merit (F = 2.3). The same system also exhibited an extraordinarily large magneto-optical susceptibility ($\chi_i{}^4$= 6.5 × 1 0^{-12} esu) and photoinduced nonlinear Faraday rotation of up to 2.5 radian/μm at a magnetic field of 0.5 T. The nonlinear response was dependent on the degree of overlap of the Fe nanopyramid on the Ag nanopyramid which influences the strength of plasmon-induced

dipoles on the Ag nanopyramid. This nanoscale system opens up a rich new set of possibilities in utilizing magneto-plasmonic materials to miniaturize future multifunctional devices at telecommunication wavelengths.

Chapter 6: Conclusions and future work

A summary of this dissertation work and potential direction of future work pertaining to optical and magneto-optical plasmonic structures is discussed.

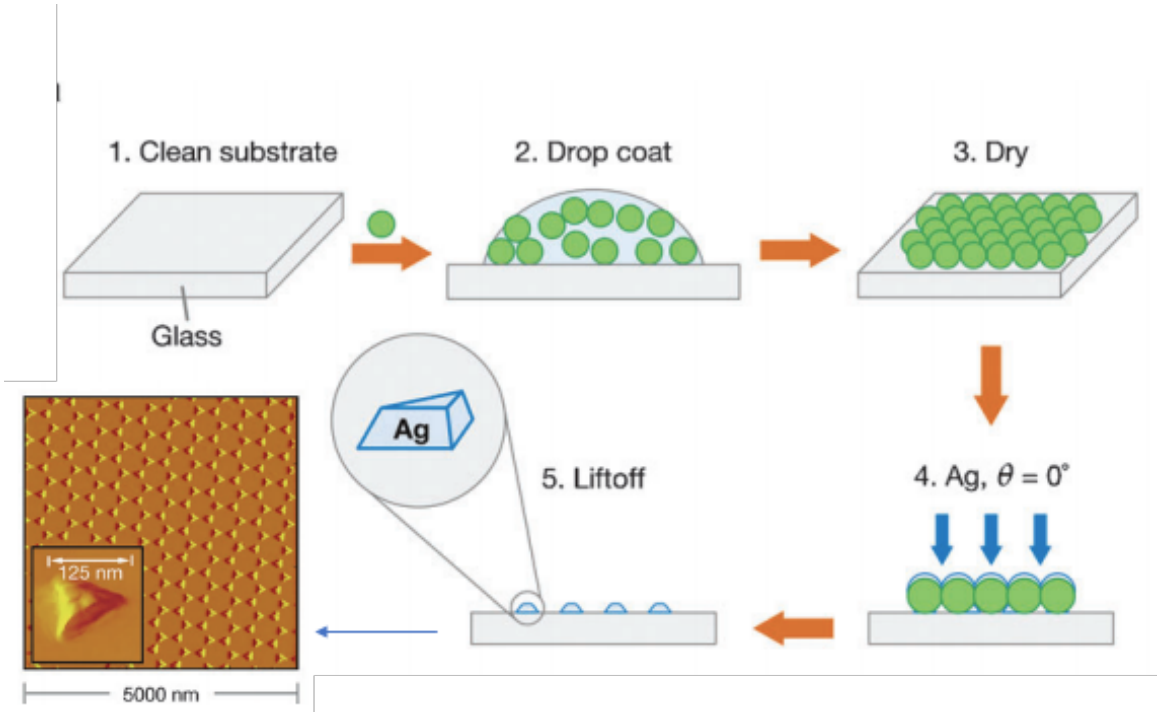

Figure 1.10: Schematic of nanosphere lithography process. Image taken from [12]. Copyright [12]

Chapter 2

Experimental methods and techniques

In this study I used a number of synthesis and characterization methods. The synthesis methods are discussed in subsection 2.1 while characterization methods are discussed in subsection 2.2.

2.1 Synthesis

2.1.1 Sample preparation

Thin film deposition

The substrates for Ag films deposition were prepared by cutting fused quartz and SiO_2/Si substrates into the size of 5 mm $\times$ 5 mm. The substrates were then sonicated in acetone, ethanol and deionized (DI) water. The substrates were then dried with nitrogen gas.

Thin films were deposited by the electron-beam (e-beam) evaporation technique. This is a well-established technique for depositing films of varying thicknesses in vacuum. First, target materials (in the form of nuggets or ingots) are placed inside crucibles, which are then heated by means of a current passed through a filament placed very close to the crucible. In fact, the electrons emitted due to high voltage between the filament and the hearth collides with the target material and causes them to evaporate or sublime. The deposition will take place inside a vacuum chamber at a base pressure.

For this dissertation work, I deposited Ag thin films of 2 nm to 20 nm onto quartz substrates using electron beam evaporator; a Mantis QUAD-EV-HP e-beam source was used. The Mantis QUAD-EV-HP e-beam evaporator is shown in Figure 2.1(a) and the schematic of evaporating technique is shown as in Figure 2.1(b). The base pressure of 1 $\times 10^{-8}$ Torr and room-temperature conditions were used for deposition. The typical deposition rate was 4 nm/min under this condition. The deposition rate was periodically calibrated using atomic force microscopy imaging for different vacuum pressures and flux currents.

Nanosphere lithography (NSL)

The substrates for NSL preparation were quartz, glassy carbon and Silicon Nitride membrane window TEM grids. The quartz wafers were cut into pieces of 5 mm $\times$ 5mm and sonicated in a 5:1:1 volume ratio mixture of ammonium hydroxide, DI water and hydrogen peroxide for 15 minutes followed by DI water for 5 minutes. The sonication of this mixture of solution enhances the hydrophilic nature of the quartz substrates.

The NSL mask preparation was performed as described in Prasad et al. [13]. The steps of mask preparation method is shown in Figure 2.2 . First a microdroplet of volume 50 μL with 1:7 by volume ratio of polystyrene beads (500 nm diameter) solution (in water) and ethanol was prepared in a cuvette. Then, deionized water was dropped gradually along the edge of a clean petri-dish using a dropper until the dry circular area of approximately 1 cm^2 with three phase contact line of air, petri dish glass and water were achieved.

Then microdroplet of PS beads+ethanol was transformed into a dry region of the petri dish. As this droplet has less surface energy than petri dish glass, it spreads into a thin fluid layer. Once the thin layer comes contact into water layer, the convective fluid flow occurs from thin fluid layer to water layer owing to Marangoni effect [water surface energy is higher than ethanol]. Due to the hydrophilic nature of PS bead and convective fluid flow, the PS beads float on the water layer in the monolayer form. Then a 0.02 % (v/v) solution of triton-X in DI water was added to compact the polystyrene beads. The polystyrene bead was then transferred onto the quartz substrates. For TEM sample preparation, the method described by Malasi et al. [14] was employed. The schematic of the technique is shown in Figure 2.3.

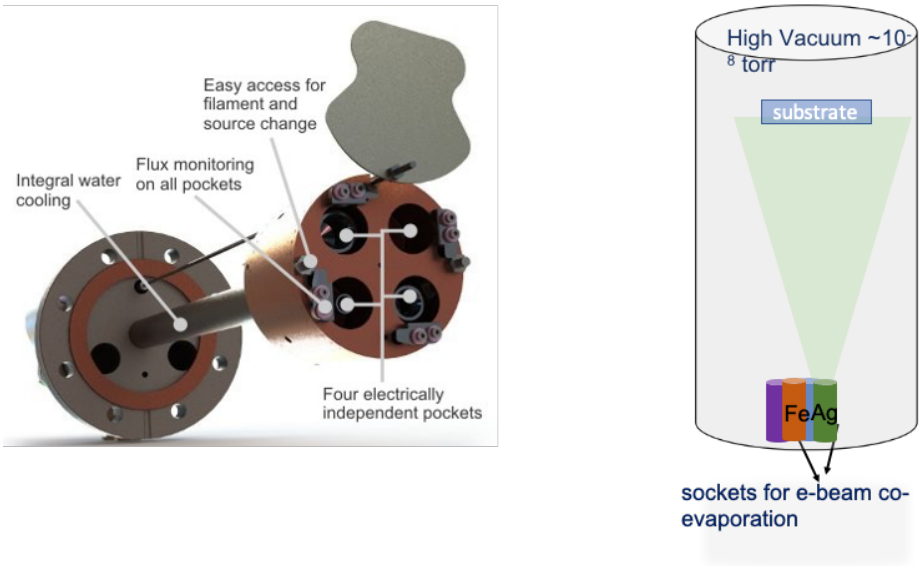

Figure 2.1: (a) Mantis QUAD-EV-HP e-beam evaporator (b)schematic diagram for e-beam evaporator.

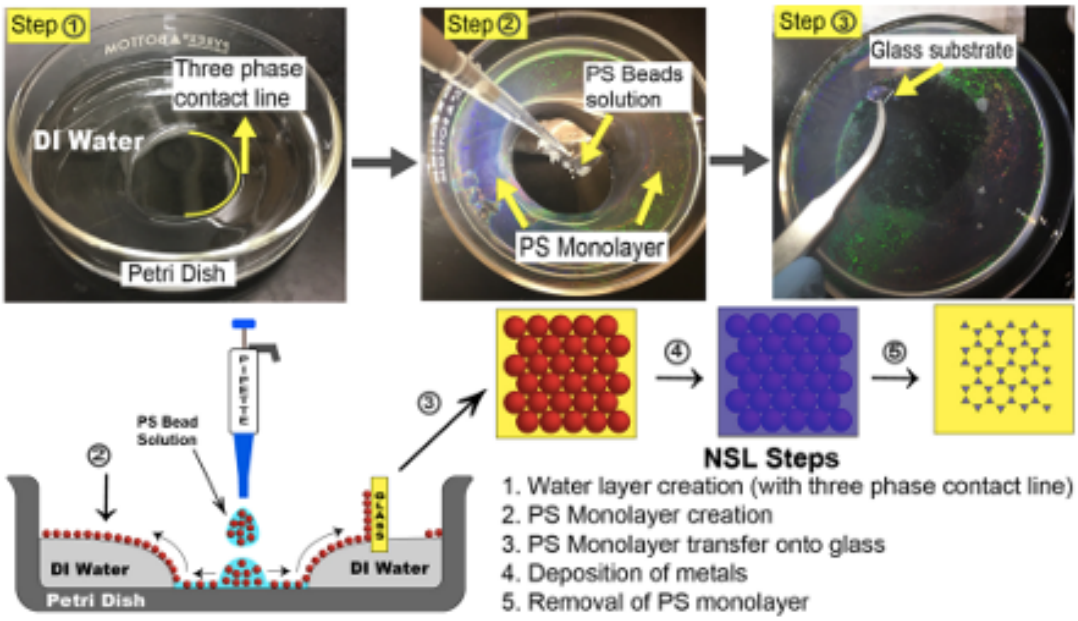

Figure 2.2: (a) NSL mask preparation method. Image taken from [13]. Copyright [13]

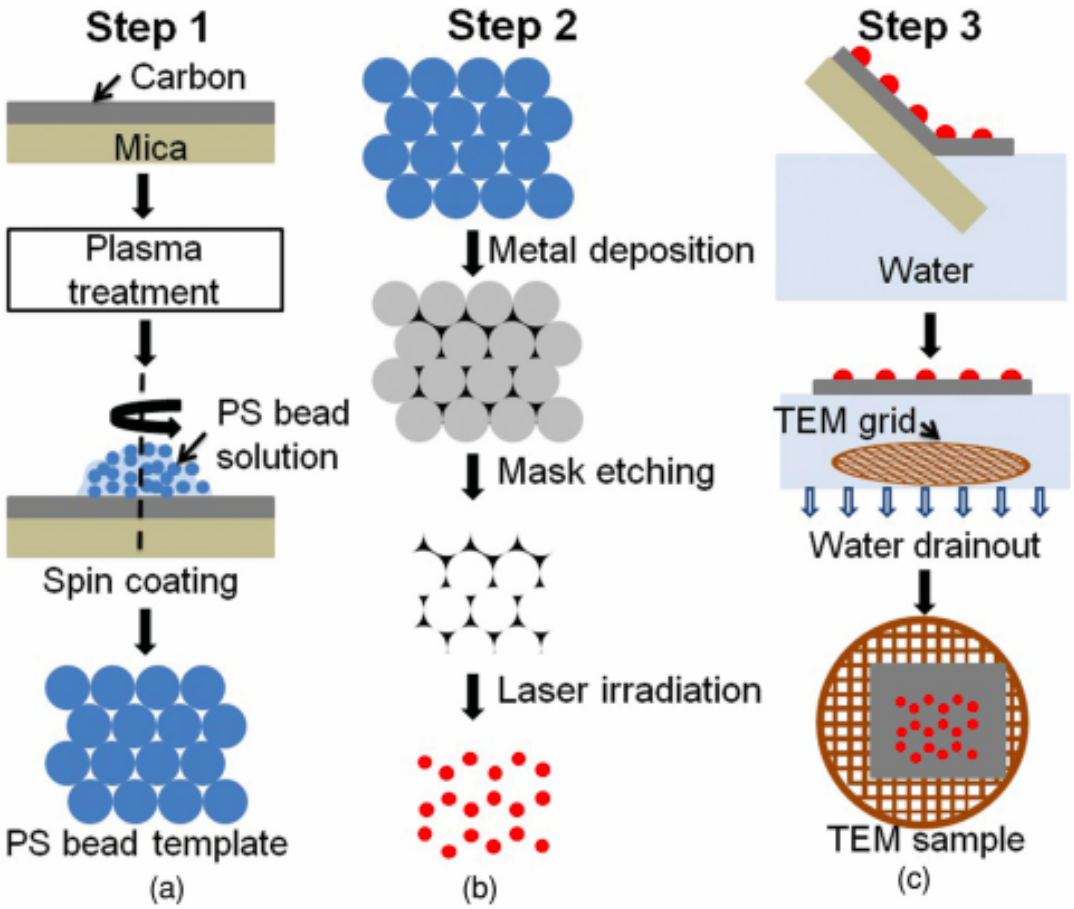

Figure 2.3: The schematic showing the major steps for the TEM sample preparation. (a) NSL template formation. (b) Fabrication of nanostructures and (c) Float-off the carbon substrate with metal nanostructures on the water surface which is then captured on the TEM grid by draining the water. Image taken from [14]. Copyright [14]

Later, metal vapors were used to deposit on the substrates through the interstices of the ordered beads. To fabricate Fe-Ag partially overlapped nanopyramidal structures, we first deposit Ag metal vapor at an angle of 5° (175°) off to the normal of the masked substrate. Then Fe metal vapors are deposited on the substrate at an angle of 5° (185° degrees) off to the normal of the masked substrate so that the partial overlap of the Fe and Ag triangles are achieved.

2.1.2 Thin film dewetting by nanosecond pulsed laser irradiation

Quanta-Ray Pro-Series Nd:YAG LASER system was used to irradiate the thin Ag film. Typically, I used 266 nm wavelength, 9 ns pulse width and 50 Hz repetition rate at normal incidence by unfocused linearly polarized laser beam with area 1 mm × 1mm at the required fluency. The water droplet of 100 μL was placed on the top of a thin film surface and was irradiated with a single pulse with laser fluency of 100 mJ/cm^2. The schematic set up of pulsed laser irradiation of Ag thin films is shown in Figure 2.4. After irradiation the samples were dried for optical and microscopy characterizations.

2.2 Characterization

2.2.1 Scanning electron microscopy

Surface morphology and contact angle behavior of nanoparticles were characterized using the scanning electron microscopy. I used ZEISS Merlin SEM instrument at an accelerating voltage of 2 kV to 10 kV. The plan view morphology of nanoparticles was used to determine diameters while the side view morphology was used to determine the contact angles of nanoparticles. The Figure 2.5 shows the plan view and side view morphology of the nanoparticles synthesize in glycerol and air. The details about calculating the contact angles from SEM images are described by Prasad et al [138].

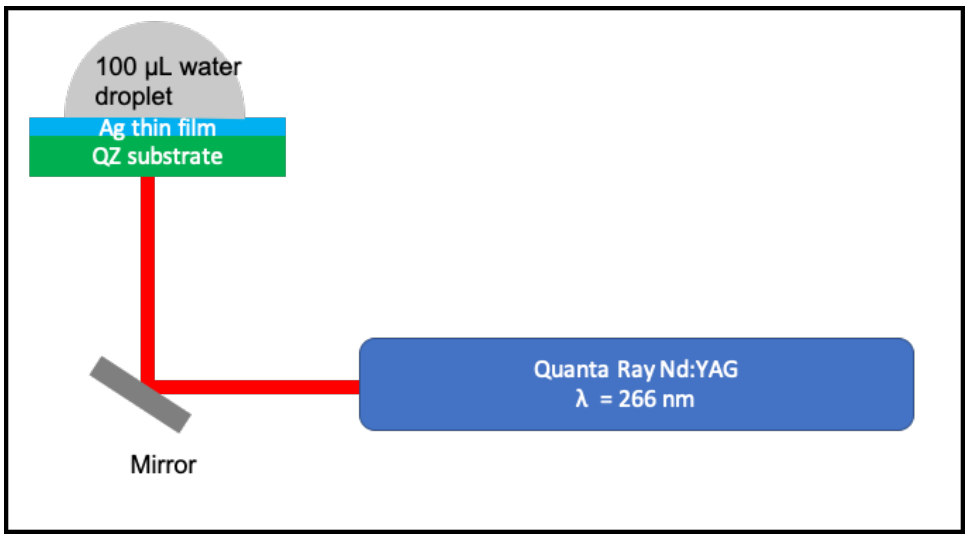

Figure 2.4: (a) Schematic experimental set up of pulsed laser irradiation of Ag thin films

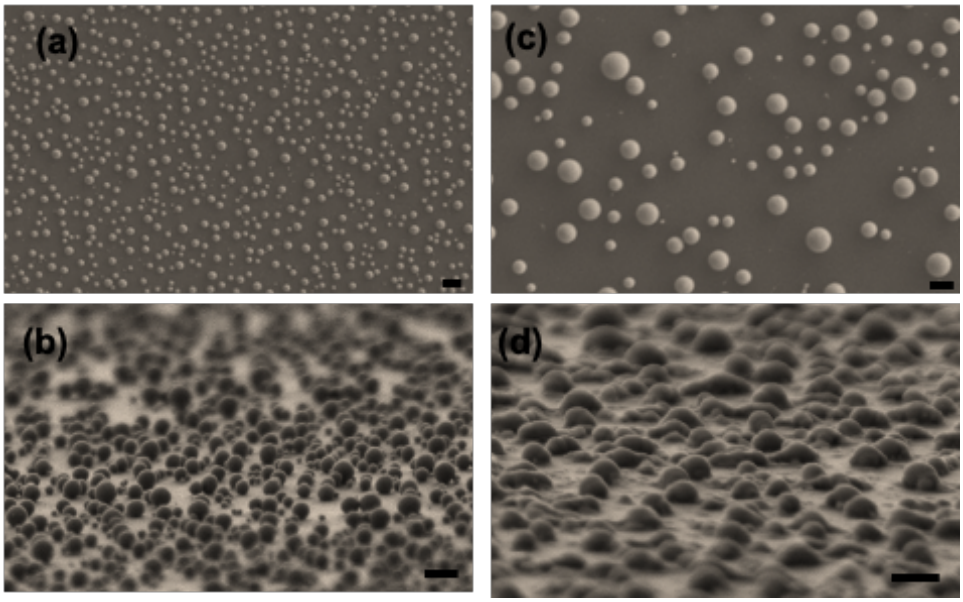

Figure 2.5: SEM image of (a) plan view and (b) side view of Ag nanoparticles formed from Ag thin film under glycerol by irradiating the Ag film at laser fluency of 100 mJ/cm^2 for 60 pulses; SEM image of (c) plan view and (d) side view of Ag nanoparticles formed from Ag thin film in air by irradiating the Ag film at laser fluency of 100 mJ/cm^2 for 60 pulses (scale bar is 200 nm)

SEM image analysis

SEM images of Ag nanoparticles for size distribution, diameters and spacing were analyzed using ImageJ-NIH software [139]. SEM image of Ag nanoparticles with 512 ×512 pixel resolution and its fast Fourier transform (FFT) images are shown in inset of Figure 2.6(a). To find the length scale by quantifying the FFT image; first, the wavenumber (K) of FFT is calculated by ((2πR/512)/length(nm) of a unit pixel) is determined. Then, average distance between neighboring nanoparticles is calculated using the relation $\Gamma = 2\pi/K$. To determine the size of the particles, first the image was converted into binary format and appropriate threshold was used to get the solid black particles and white background as in Figure 2.7. Then the area of each particle was determined by ImgeJ and later the area was converted into diameter of the particles.

2.2.2 Atomic force microscopy

Thickness, surface roughness of thin films and height of metallic nanostructures were studied by using Asylum MFP3D Atomic Force Microscopy in standard AC mode in air. In AC mode, the cantilever is oscillated mechanically by a piezoelectric actuator. The name "AC mode" comes from the tip oscillation like that of AC current. The line scan was used to analyze the image using Gwyddion image analysis software [140]. The AFM images showing the nanopyramid height is shown in Figure 2.8.

2.2.3 Transmission electron microscopy

The transmission electron microscopy methods is a powerful tools to study the material structural and chemical properties. This involves many techniques such as selected area electron diffraction (SAED), high resolution transmission electron microscopy (HRTEM), electron energy loss spectroscopy (EELS) amongst others. In SAED, the sample is subjected to parallel beams unlike in convergent beam electron diffraction (CBED-diffraction from very small region). SAED pattern originates when constructive interference of the coherently scattered electron waves by the specimen occurs. This is achieved by inserting an aperture at the image plane of the objective lens. It is recommended to use the condenser aperture

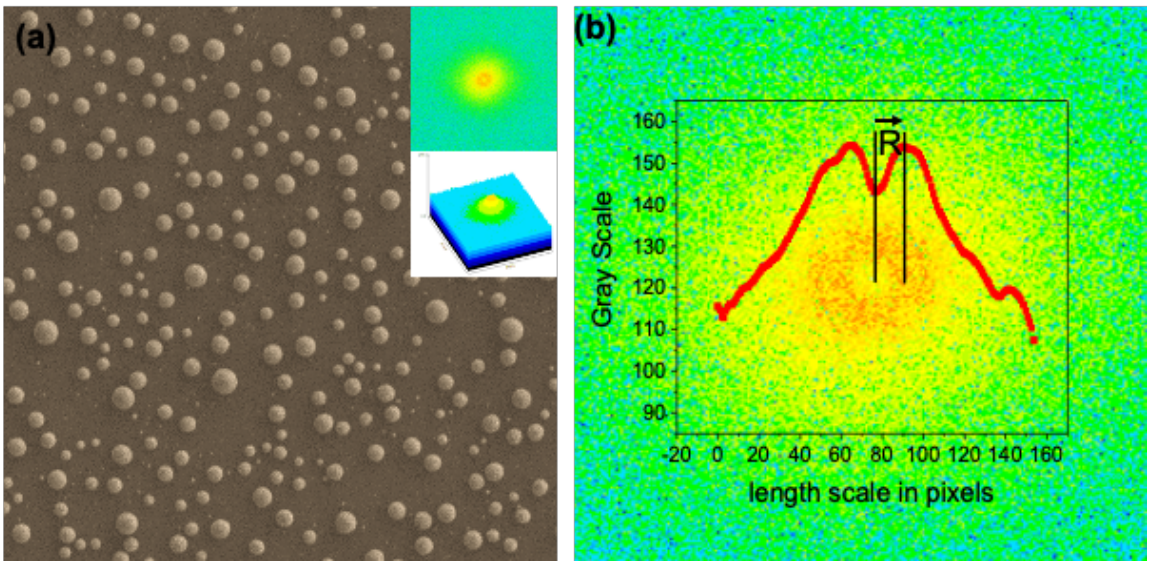

Figure 2.6: (a)SEM image of Ag nanoparticles of size 512×512 pixels: top and bottom insets show the FFT image with 2D and 3D views (b) Line profile of FFT image

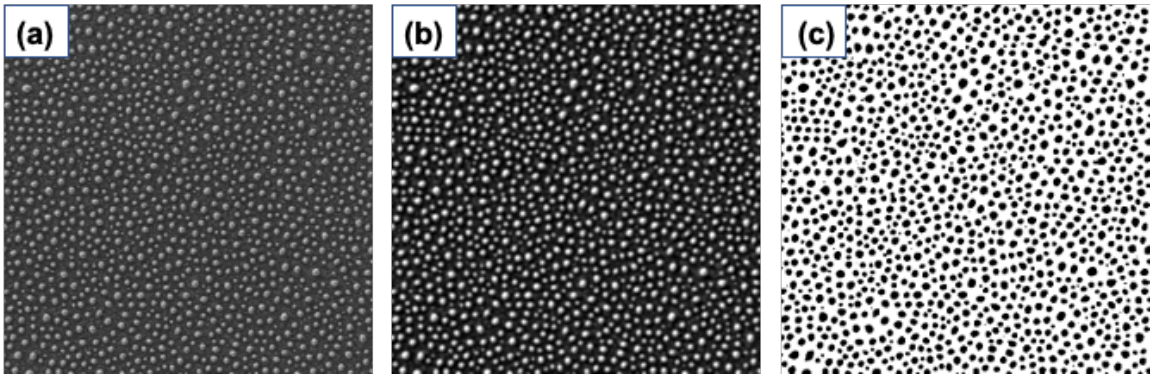

Figure 2.7: (a)Original SEM image (b) image after band-pass filtering (c) image after binary formatting. Size is 512×512 pixels

(Kohler illumination) to define the field of illumination which gives more precision of the selected area. Each spots in SAED pattern satisfy diffraction condition. SAED pattern provides several information about material properties such as material phases, orientations of crystals, crystal defect density, poly-crystallinity, amorphousity etc. An HRTEM image also called phase contrast images is produced by an interference pattern of the electron wavefunction with itself after it is diffracted from the specimen. This image is useful to understand the atomic structures and can be interpreted with fast Fourier transform (FFT) analysis. EELS is an advance TEM technique where analysis of monoenergetic electrons are done after interaction of them with specimen. This technique can be used to extract the information of material systems about atomic composition, chemical bonding, electronic properties, surface properties, pair distance distribution functions and excitation energy of surface plasmons amongst others [32]. Cathodoluminescence is an electromagnetic phenomena in which electrons incident on a material cause the emission of photons. It can be used to map the local density of states of photonic nanocrystals and plasmonic nanomaterials [141]. In this thesis work, I have used Libra 200 MC Microscope. In order to image the quality and crystallinity of nanostructures, the imaging at acceleration voltage of 200 keV was performed. The imaging was performed at low magnification (31 K) as well as high magnification (630 K). The imaging of gold nanoislands sputtered on Carbon substrates at different magnification obtained to calibrate the magnifications are shown in Figure 2.9.

Electron energy-loss spectroscopy (EELS)

EELS in STEM mode was performed in Libra 200 MC Microscope. It has five different dispersions namely 0.025, 0.05, 0.1, 0.25 and 0.4 eV/channel which corresponds to energy range of about 60, 120, 240 550 and 2000 eV respectively. The energy resolution of the spectrum is determined by using different monochromator (MCR) slits (0.5 μm, 3 μm, 5μm, 60μm). In our experiments, we have used MCR slits of 0.5 μm which gives energy resolution upto 0.10 eV. The software used for spectra acquisition is the Digital Micrograph from Gatan, Inc. In the low-loss spectrum in EELS, the information about optical properties of material particularly plasmons excitation were extracted. For this dissertation work, we measured the low-loss spectrum of Ag, Co-Ag and Fe-Ag nanostructures to get the information about

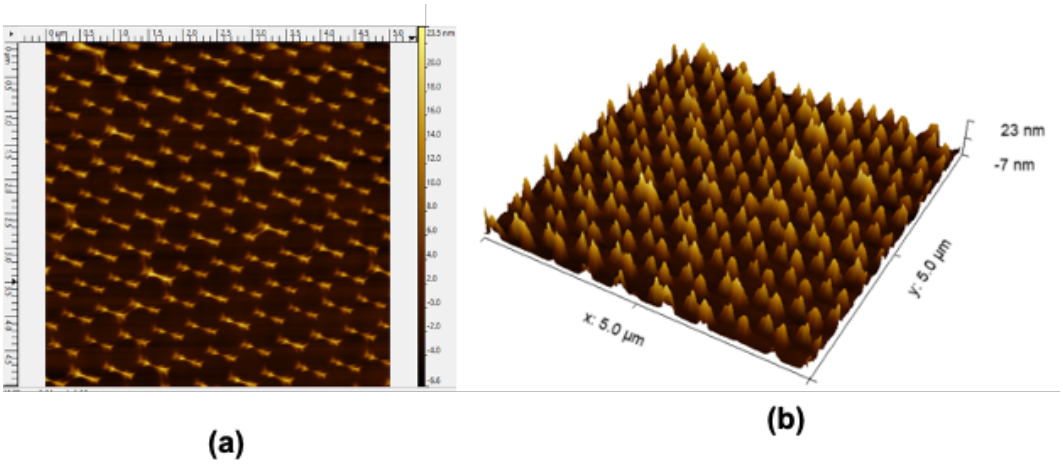

Figure 2.8: (a) 2D view and (b) 3D view of atomic force microscopy image of Fe-Ag nanopyramidal hexagonal arrays

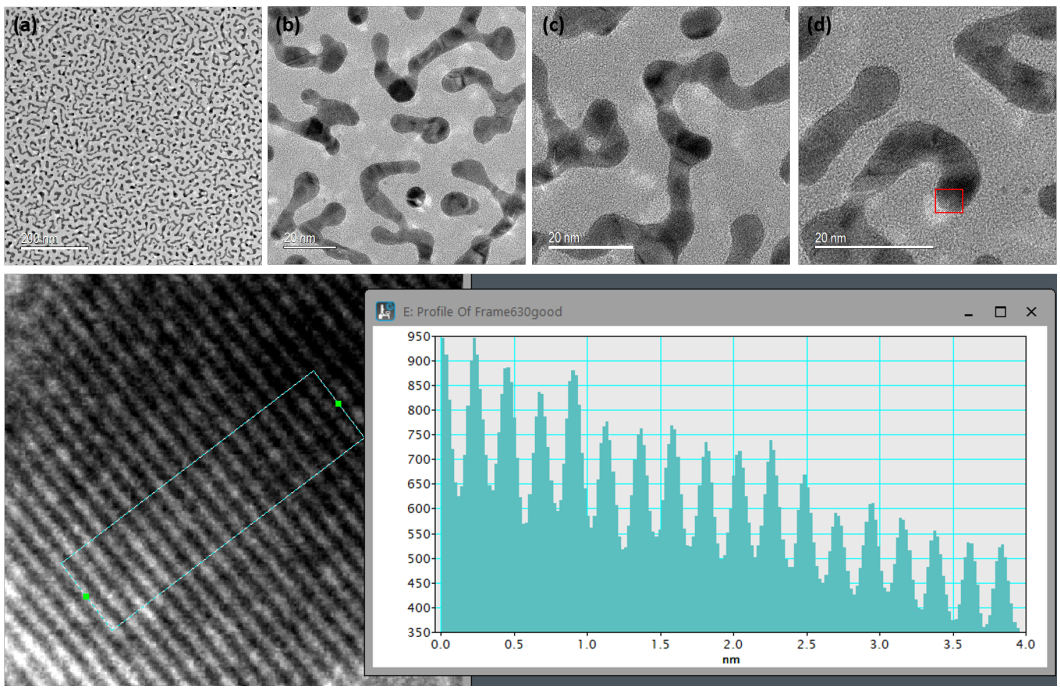

Figure 2.9: TEM micrographs of Gold islands at magnification of (a) 31 K (b) 250 K (c) 430 K (d) 630 K; Bottom image - Au <111> surface showing intensity profile. The measurement here shows the average Au <111> plane spacing is 0.228 nm

plasmons loss and an EELS map was used to examine the plasmon loss behavior in the region of interest (ROI). We took the EELS map pixel by pixel where each pixel is specific to electron beam with same exposure time.

Quantification of EELS

The absolute quantification of EELS was needed to compare optical data with EELS data as well as EELS data among different nanostructures. Quantification of EELS was performed using Jupyter notebook where EELS intensity was converted into scattering probability per unit energy-loss. The scattering probability was obtained by dividing the total intensity of spectrum by total intensity under zero loss. A multiplication of the Lorentzian functions was used to approximate the zero loss peak while plasmon loss peaks were fit by Gaussian function.

2.2.4 UV-Vis-NIR spectroscopy

UV-Vis-NIR spectrophotometry refers to absorption spectroscopy or reflectance spectroscopy in part of the ultraviolet and infrared, and the full visible spectral regions. The UV-Vis-NIR spectroscopy can be used to study the resonant absorption due to plasmon excitation as well as to measure the thickness and optical properties of thin films. Optical properties for the Ag and CoAg nanoparticles, and Fe-Ag arrays were measured by the HR2000+ES spectrometer from Ocean Optics in the transmission mode. It contains unpolarized light from deuterium and halogen sources and probe area of 600 μm. In our experiment, the optical spectra were collected with acquisition time of 0.1 sec. Further, the output spectra were averaged over 100 scans to increase the signal to noise ratio. The transmission spectra were later converted into absorption mode by using Beer Lambert law of optical absorption as $Absorpton = Ln(100/Transmission(\%))$.

2.2.5 Nonlinear optical measurements

A schematic of experimental set up to calculate the value of n_2 and β is shown in Fig. 2.10 . First, for the open aperture configuration, we used a 1550 nm fiber laser with a pulse

duration of 64 fs, and an average power of 20 mW which was incident on an electrically focused tunable lens (EFTL).

The samples were placed at distance f_s from the EFTL. The output of the lens impinged in the sample and the intensity in the sample was controlled by changing the focal length of the EFTL with applied current. The transmitted laser beam was detected with a Ge-photodetector, and the normalized transmittance was used to calculate the value of β using the relation as,

$$T(f) = \frac{1}{B(f)} \int ln\{1 + B(f)sech^2(\rho)\}d\rho, \rho \to 0, \infty \tag{2.1}$$

with

$$B(f) = \beta(1 - R)I_o(f)L_{eff} \tag{2.2}$$

Here, L_{eff} is the effective sample thickness given by $L_{eff} = \frac{(1-e^{-\alpha L})}{\alpha}$, L being sample thickness and α being linear absorption coefficient. Also, R is reflection coefficient and I_o is peak intensity of the beam which is a function of focal length. Also, ρ is expressed as $\rho = \frac{2ln(1+\sqrt{\tau})}{\tau}$ with τ being full width at half maximum pulse duration.

Second, the samples were tilted at an angle of θ with respect to the laser beam direction and the light reflected by the sample surface was analyzed to measure the n_2. The normalized reflected beam intensity can be expressed as

$$R_N(f, \theta) = 1 + Re\left[\frac{2n_o^3 cos\theta - 4n_o^2 sin^2\theta cos\theta}{n_o^4 cos^2\theta - n_o^2 + sin^2\theta}\right]\left[\frac{(n_2 + ik_2)I_o}{\sqrt{n_o^2 - sin^2\theta}}\right]\left\{\frac{1}{1 + (\frac{f_s - f}{Z_0(f)})^2}\right\} \tag{2.3}$$

Here, $f, Z_0(f), \theta, n_o$ and k_2 are the focal length of EFTL, Rayleigh range, angle between normal to the incident beam and sample surface, linear refractive index and extinction coefficient respectively.

2.2.6 Linear Faraday rotation

In the typical Faraday rotation experiment the Intensity of the laser beam arriving at detector is given by

$$I = MA_0^2 cos^2(\phi - \theta) \tag{2.4}$$

where M is a proportionality factor which depends on the conversion efficiency of the detector, and ϕ is the relative angle between polarizer and the analyzer.

For maximum sensitivity, ϕ should set to 45°, therefore the intensity is given by

$$I = \frac{MA_0^2}{2}[1 + sin2\theta] \tag{2.5}$$

where θ is the angle of rotation due to magnetic field is given by

$$\theta = VBd \tag{2.6}$$

where, V is Verdet constant, d is thickness of the sample. In the experiment the laser intensity is beam modulated at a frequency Ω and therefore the intensity become oscillatory given by,

$$I = \frac{MA_0^2}{2}[1 + sin2\theta]sin(\Omega t) \tag{2.7}$$

the photodetector converts light intensity into current. So the detector reads an ac current given as,

$$i_{ac} = \frac{MA^2}{2}[1 + sin2\theta] \tag{2.8}$$

and the lock-in amplifier measures the rms value as,

$$I_{ac} = \frac{i_{ac}}{\sqrt{2}} = \frac{MA^2}{2\sqrt{2}}[1 + sin2\theta] \tag{2.9}$$

and at zero magnetic field, $\theta = 0$,

$$I_{ac}(B = 0) = \frac{MA^2}{2\sqrt{2}} \tag{2.10}$$

and for small θ, Sin$(2\theta) \sim 2\theta$,

$$\frac{I_{ac}}{I_{ac}(B = 0)} = 1 + 2\theta = 1 + 2.VBd \tag{2.11}$$

For the analyzer set at 45° and -45°

$$\frac{I_{ac}}{I_{ac}(B=0)} = 1 + sin(2\theta), for + 45° \tag{2.12}$$

$$\frac{I_{ac}}{I_{ac}(B=0)} = 1 - sin(2\theta), for - 45° \tag{2.13}$$

2.2.7 Nonlinear Faraday rotation

The nonlinear magnetic (nonlinear Faraday effect) activity of the nanostructures were measured using a standard Faraday rotation experimental set up as shown in Figure 2.11. This is a combination of f-scan and polarization rotation. In this experiment the laser with a linear polarized light is focused on the sample by the electrically focused tunable lens (EFTL) and a regular f-scan is taking with as a function of applied magnetic field, in the Faraday configuration, the DC magnetic field produced by a R-K electromagnet, was varied from 0 upto 0.5 T in steps of 0.1. We record the transmission of the laser beam of wavelength 1550 nm as a function of current in the EFTL at some fixed value of the magnetic field, after the the beam is pass through a Thomson polarizer oriented at 45° angle with respect to the incoming polarization when there is no magnetic field applied.

The dependence of the transmission of the laser beam on the magnetic field can be understood as interplay between the intensity of the beam and magnetic field and it is known as the nonlinear Faraday effect, or photoinduced Faraday rotation. The transmitted intensity of the beam is affected by two photon absorption given by

$$I(f) = \frac{I_o(f + f_s)}{1 + \beta I_o(f + f_s) L_{eff}} \tag{2.14}$$

and the polarization angle of rotation ($\Delta\Theta$) can be expressed [142] as

$$\Delta\Theta = VHL_{eff} - \frac{\chi_i^4}{2\chi_i^3} Hln\left\{1 + \beta I_o(f + f_s) L_{eff}\right\} \tag{2.15}$$

Where, H is the applied magnetic field and V is the Verdet constant, and $\chi_i^4$and χ_i^3 are the imaginary components of the fourth-order nonlinear and third-order nonlinear

susceptibilities. The first term in Eq. 2.15 corresponds to the linear Faraday effect, while the second term is the photo-induced contribution to the nonlinear rotation. The transmittance of the beam passing through the analyzer can be calculated using Malus's law in the small angle approximation and optimizing for sensitivity as,

$$T(f) = \{1 - \beta I_o(f + f_s)L_{eff}\} \left[1 + VHL_{eff} - \frac{\chi_i^4}{2\chi_i^3} Hln\{1 + \beta I_o(f + f_s)L_{eff}\}\right] \quad (2.16)$$

In terms of the absorption coefficient α and two-photon coefficient (β), the above expression can be written as,

$$T(f) = \{1 - \beta I_o(f + f_s)L_{eff}\} \left[1 + VHL_{eff} - \frac{3\alpha}{4\epsilon_0 nc\beta} Hln\{1 + \beta I_o(f + f_s)L_{eff}\}\right] \quad (2.17)$$

The above expression contained information about the linear and nonlinear Faraday effect, so careful must be taken if 2.17 is used to obtain the Verdet constant, this will show as an offset of the low intensity portion of the trace , that will be lost if the transmittance is normalized. From the experimental data, on our case, it was clear that there is not linear Faraday rotation (zero offset in the wings as function of the B-field) and the rotation is due to pure photoinduced Faraday effect, in this case the above expression can be written as,

$$T(f) = \{1 - \beta I_o(f + f_s)L_{eff}\} \left[1 - \frac{3\alpha}{4\epsilon_0 nc\beta} Hln\{1 + \beta I_o(f + f_s)L_{eff}\}\right] \quad (2.18)$$

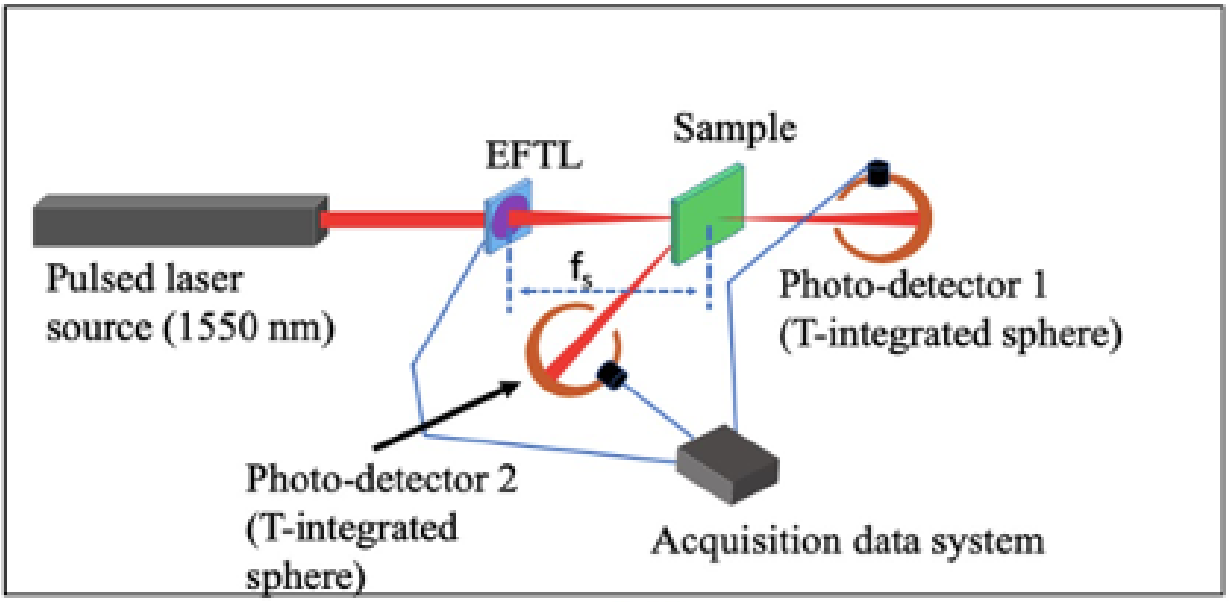

Figure 2.10: (a) Schematic diagram for experimental setup of f-scan method

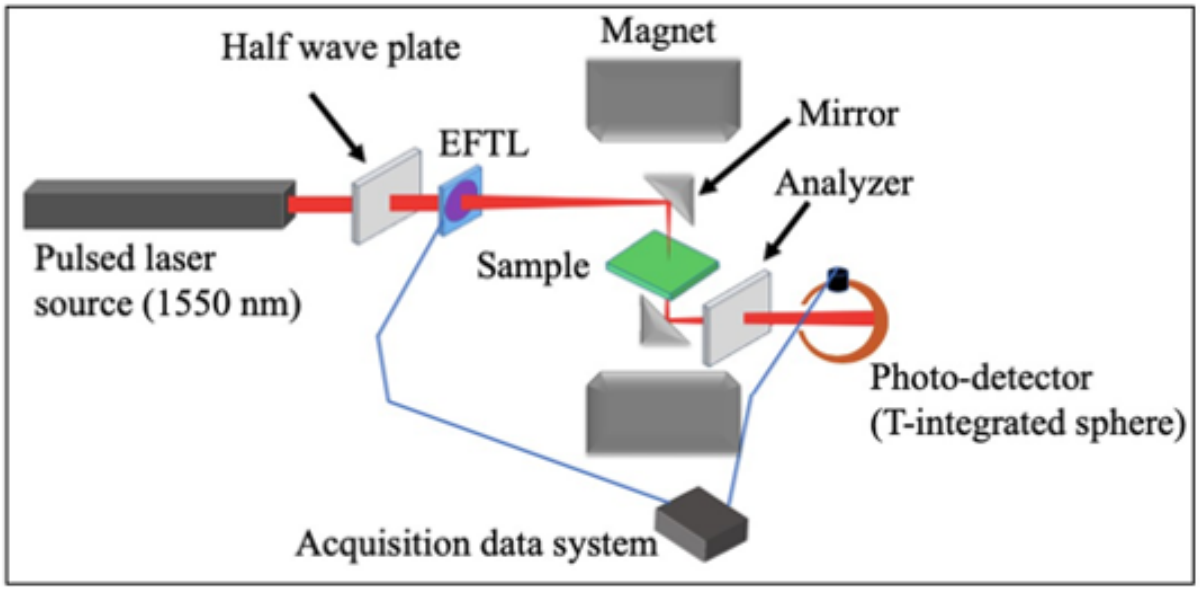

Figure 2.11: (a) Schematic diagram for experimental setup of the nonlinear-polarization rotation F-scan method,

Chapter 3

Detection of localized interface plasmons

(This work is a continuation of the work reported in [1] and published in *Plasmonics* [118])

3.1 Introduction

Tailoring of photon-matter interaction in solid material is critical for surface plasmon resonance (SPR) based sensing. This can be achieved from suitable material with interface engineering. The modified plasma oscillations in metal-metal interfaces are highly sought-after phenomena in plasmonics, however, such a localized nature of this oscillation has never been reported. Here, we present the first evidence of localized interface plasmons from CoAg bimetallic nanoparticles by employing scanning transmission electron microscopy - electron energy-loss spectroscopy (STEM-EELS). We found that the localized interface plasmons oscillates with a frequency in between in-plane dipole mode and quasiplanar mode. Moreover, we observed that the localized interface plasmon resonance is stronger than in-plane dipole LSPR which was characterized by comparing the quality factor of the energy-loss peaks. Such interface plasmon resonance was not distinctly observed from ensembles of CoAg nanoparticles by optical excitation incident normally, however, a broader in-plane dipole mode was observed compared to similar pure Ag nanoparticles. This direct detection of plasmons confined to the interface region could drive to future engineering of bimetallic interfaces with improved plasmonic activity.

Interface plasmonic properties of metallic nanoparticles have been of great interest towards localized surface plasmon resonance (LSPR) based sensing [143, 144, 145]. In the case of the metal-dielectric interface, the LSPR effect has been well studied in the past [102, 146, 147, 148, 149]. In addition, a significant number of studies have been focused on LSPR response of metal-semiconductor interfaces, with several works reported in the literature [50, 150, 151, 152]. However, the observation of localized plasmon resonance behavior at metal-metal interface has not been reported yet, while the existence of spatially localized interface plasmons between two metals was suggested by Stern et al. long time ago [31]. Thenceforward, most of the theoretical and experimental works were merely focused on identifying the characteristics interface plasmons (propagating or standing) frequency from bimetallic interface [153, 154, 155].

The direct detection of localized plasmonic behavior at bimetallic interface has been challenging. One of the reasons is due to difficulty in fabrication of sharp and robust atomic interfaces between two metals in bimetallic nanoparticles, which, with their sizes comparable to light waves, are able to excite localized plasmons. Another reason is, while most studies on those types of nanoparticles are performed by means of optical excitation, sufficient spatial resolution of material interfaces could not be achieved. Moreover, a comprehensive theoretical understanding of interface plasmonics has not been developed yet. It is because the existing theory is based on the dielectric function of the surrounding matrix and fails to account for modified chemical bonds and subsequent charge density and effective mass of electrons at the interface. Partly motivated by these limitations, the understanding of plasmon behavior from electron energy-loss spectroscopy and crystallinity in the interface region could improve the present state-of-the-art in interface plasmonics.

Our group previously reported an observation of electron energy-loss peak when a monochromatic electron beam passed near the Co side of a CoAg bimetallic nanoparticle. This electron-energy loss behavior in low-loss spectrum was attributed to excitation of "ferroplasmons" [23]. However, the origin of such plasmons was not determined to our satisfaction. The primary reason was due to the nanocrystalline nature of the two different materials within the nano-particles . In this work, we present detailed analysis of CoAg bimetallic nanoparticles with even better energy (0.15 eV) and spatial (1.8 Å)

resolution obtained for nanoparticles with higher degree of crystallinity. With these improved experimental conditions, we now report the observation of localized interface plasmons at the metal-metal interface in CoAg bimetallic nanoparticles by means of scanning transmission electron microscopy - electron energy-loss spectroscopy (STEM-EELS). Here, we begin first by comparing plasmon induced optical absorption modes excited by broadband light wave with the Eigen-frequencies obtained from plasmon induced EELS for an ensemble of Ag nanoparticles. This will identify the observed correlation of plasmon induced resonance modes such as intensities and peak positions excited by different sources viz. photons and electrons. Second, we present the nature and strength of localized interface plasmons oscillation by comparing its plasmon energy and quality factor with those of in-plane dipole and quasi-planar (QP) mode, which is a superposition of higher order modes.

3.2 Methods

Ag films of 5 ± 0.2 nm, 8 ± 0.2 nm and CoAg bilayer films of (3+5) ± 0.2 nm thickness were deposited on carbon on mica in a base vacuum pressure of 6 × 10^{-8} torr at room temperature by the e-beam evaporation method (Model Mantis QUAD-EV-C). Prior to deposition, the quartz substrates were cleaned ultrasonically in ethanol, acetone and DI water, for 30 minutes at each step, respectively. The TEM samples were prepared by the method suggested by Malasi et al [14]. The single layer and bilayer films were irradiated with UV pulsed laser of wavelength 266 nm having a pulse width of 9 ns (Model Quanta-Ray Pro-Series Nd:YAG LASER) for 50 pulses at laser fluency of 100 mJ/mm^2. The resulting nanostructures were then investigated by high resolution imaging using a ZEISS Merlin scanning electron microscope (SEM) in plan view orientations. The crystalline structure and elemental distribution in selected samples were further examined by high-angle annular dark field imaging (HAADF) and electron energy-loss spectroscopy (EELS) by ZEISS Libra 200 MC in TEM as well as STEM mode at the acceleration voltage of 200 kV. The nanoparticles distribution from SEM image was studied by ImageJ software. Plasmon induced optical transmission in the UV-Vis region was recorded by an HR2000 + ES spectrometer from Ocean Optics consisting of a broadband halogen/deuterium lamp as a light source. The

transmission spectra were later converted into absorption spectra by using the Beer-Lambert law of optical absorption [156]. The plasmon energy from electron energy loss peak was calculated using the relation: $E_p = \sqrt{E_{max}^2 + \frac{\Delta E^2}{2}}$, where, E_{max} is peak energy at the highest intensity and ΔE is the full width at half-maximum (FWHM) of the energy loss spectra [32].

3.3 Results and Analysis

The first part of this study was motivated to compare the optically excited and Eigen EELS plasmon modes observed for an ensemble of Ag nanoparticles. For this study, we prepared an ensemble of Ag nanoparticles by dewetting Ag thin films of 8 $\pm$ 0.5 nm under UV laser of fluency of 100 mJ/mm^2 in air as the method described by H Krishna et al [157]. The resultant morphology as recorded by SEM and the subsequent histogram showing the size distribution of the nanoparticles are presented in Fig. 3.1(a) and (b) respectively. Following calculation, the average size of the nanoparticles was obtained to be 88 $\pm$ 33 nm. The plasmon induced optical spectrum from those nanoparticles was collected with normally incident broadband light over an area of 500 μm^2 in carbon thin film as substrate, and therefore it represents the ensemble sizes averaged information of the nanoparticles. The optical spectrum has two obvious plasmon peaks of Ag nanoparticles as evident from Fig. 3.1(c) [top dotted red line]. It has been reported that the lower energy peak at $\sim$2.61 eV is a dipole mode polarized parallel to the substrate (in-plane) and the higher energy peak at $\sim$3.53 eV corresponds to quadrupole mode [158]. Next, the average experimental electron energy-loss spectrum of Ag nanoparticles was obtained by summing the energy-loss spectra of individual Ag nanoparticles and then multiplying with the weight percent from their size distribution. The EELS spectra also showed the two plasmon peaks as evident from [the bottom black solid line] the Fig. 3.1(c). The low energy mode (broad peak at 2.58 eV) is in-plane dipole mode while the high energy mode (peak near 3.50 eV) is combination of QP mode and bulk plasmon modes. [159, 160].

The apparent feature, determined by comparing plasmon induced optical absorption and energy-loss spectra of dipole resonance mode, is the linewidth broadening of the dipolar peak obtained from EELS measurements. While the overall width of surface resonance modes

comes from different size distributions of the nanoparticles, the difference between peak positions in EELS and optical resonance modes should be associated with their observed part of the complex dielectric function . The electron energy-loss behavior and optical absorption behavior are described by a function of $\mathrm{Im}(\frac{\epsilon-1}{\epsilon+1})$ and $\mathrm{Im}(\epsilon)$ respectively, ϵ being the complex dielectric function of the system [32]. Another obvious characteristic observation from the EELS was the in-plane dipole mode exhibiting lower degree of surface localization (broader resonance) than a QP mode in the ensemble of nanoparticles.

In order to understand the excitation of plasmon modes from bimetallic nanoparticles, in the next step, we prepared pure Ag and CoAg nanoparticles from the dewetting of the Ag (∼5nm) and Co (∼3 nm)/Ag (∼5 nm) on carbon substrates. Their morphology and subsequent size distributions are shown in Fig 3.2(a) and (b). From histograms obtained from SEM images of nanoparticle distributions, the average diameter of the particles were calculated to be 66 ± 22 nm for Ag nanoparticles and major axis (longitudinal) was calculated to be 94 ± 33 nm for CoAg nanoparticles. For elliptical (major axis) analysis, the average circularity of 0.83 was used as obtained from ImageJ by the method described by Yasuhiro et al [161]. The representative optical absorption spectra for average particle diameter of ∼66 nm (Ag), ∼88 nm (Ag) and major axis of ∼94 nm (CoAg) in the energy range from 1.40 eV to 4.1 eV is shown in Fig. 3.2(c). For Ag and CoAg compositions with different particle size distributions, in the absorbance spectra, minima was observed at ∼3.88 eV wavelength for all sizes, which corresponds to the characteristic energy of Ag due to interband transitions. A relatively weak quadrupole resonance mode was observed at ∼3.53 eV for pure Ag nanoparticles with an average diameter of ∼66 nm and ∼88 nm , while the resonance at ∼3.56 eV was observed for CoAg nanoparticles with size distribution of ∼94 nm (major axis) respectively. The strong in-plane dipole mode was observed at 2.84 eV for Ag nanoparticles of average size ∼66 nm, while the peak at 2.61 eV and 2.58 eV was observed for Ag and CoAg nanoparticles of sizes ∼88 nm and ∼94 nm as evident from Fig. 3.2(c). Further, the full width at half maxima (FWHM) of those dipole resonance curves were calculated as follows: 0.77 eV for Ag ($D_{ave} \sim 66$ nm), 1.01 eV for Ag (D_{ave} ∼88 nm) and 1.70 eV for CoAg [D_{ave} ∼94 nm (major axis)]. One of the evident results from the observation is that with increasing size of the nanoparticles, there was a red-shift as well as an increase in linewidth

(FWHM) of the resonance curves. Moreover, while the in-plane dipole LSPR for Ag and CoAg of comparable sizes are similar in peak energy position, the intriguing contrast is the broadening of the resonance curves for CoAg. Accounting the small red shift of the CoAg compared to Ag particles with 88 nm diameter, we can conclude that the dipole resonance is associated with the total dimension of the CoAg particle and not the silver portion alone. We also observed that FWHM broadened by 0.21 eV for an average diameter increase of 22 nm among pure Ag nanoparticles, while it broadened by 0.71 eV for only an increase of 6 nm from Ag to CoAg nanoparticles. So this increased broadening in CoAg nanoparticles compared to Ag nanoparticles can not be introduced by the particle size distribution.

In order to shed further light on the broadening of the optical spectra from CoAg nanoparticles compared to Ag nanoparticles of identical sizes, the crystallinity and plasmonic properties of these CoAg nanoparticles were studied with STEM-EELS. Fig. 3.3(a) shows a Z-contrast image of a selected CoAg bimetallic nanoparticle. The dark and bright sides in the figure represent the Co and Ag respectively. The high resolution transmission electron micrograph of the interface region of the CoAg particle [as denoted by the red dashed square in Fig. 3.3(a)] is shown in Fig. 3.3(b). The crystallinity of the particle was determined by the fast Fourier transform (FFT) of images obtained from Co [left inset in Fig. 3.3(b)] and Ag [right inset in Fig. 3.3(b)] region. From FFT diffractograms , we observed that the crystal structure of the interface is well defined and not polycrystalline as in previous studies. Further, crystal structures of both sides were face centered cubic (FFC) with a common [100] direction for this epitaxial interface.

The EELS spectra taken from three regions in Fig. 3.3(a) viz. (1) the surface of the Co side with dark cyan color (Co side), (2) the surface of Ag with red color (Ag side) and (3) the triple point with blue color (triple point), are presented in Fig. 3.3(c). The summary of features in the EELS obtained from the all three regions are presented in Table 3.1. As evident from Table 3.1, the plasmon induced in-plane dipole energy mode was observed near 2.25 $\pm$ 0.05 eV for all probed regions which was red shifted compared to the optically observed position (2.58 eV). This shift originates in the particle size, because the investigated CoAg nanoparticle has longitudinal diameter of 120 nm while the average diameter of CoAg nanoparticles investigated optically was 94 nm. Another important observation was the

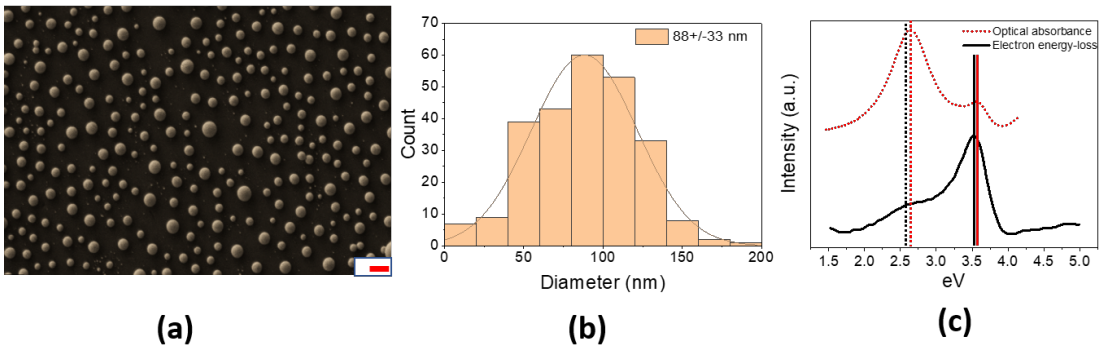

Figure 3.1: (a) A SEM micrograph of nanoparticles fabricated by laser dewetting of Ag (8 nm) thin film. [The scale bar is 200 nm] (b) the size distribution of the nanoparticles showing the average diameter of the particles 88 ± 33 nm. (c) comparison of optical absorption spectrum with average energy loss spectrum for Ag nanoparticles of same size and distribution.

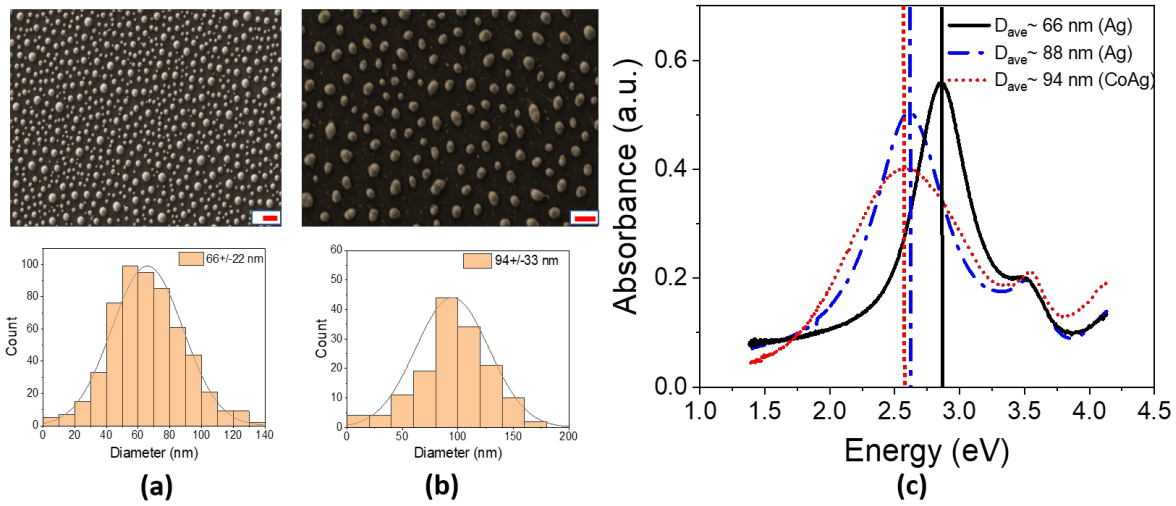

Figure 3.2: (a) (Top)SEM micrograph showing the arrangement and distribution of nanoparticles following dewetting of Ag (5 nm) thin film. [The scale bar is 200 nm], (bottom) the size distribution of the nanoparticles showing the average diameter of the particles 66 ± 22 nm. (b) (top)SEM micrograph showing the arrangement and distribution of nanoparticles following dewetting of Ag (5 nm)/Co(3 nm) thin film. [The scale bar is 200 nm] (bottom) the size distribution of the nanoparticles showing the average major axis of the particles 88 ± 33 nm.(c) Interband transition minima (∼3.88 eV), quadrupolar (3.51-3.54 eV) and in-plane dipolar LSPR positions (2.85 eV-2.58 eV) as a function of energy for nanoparticle arrays with sizes of ∼66 nm (Ag), ∼88 nm (Ag) and ∼94 nm (CoAg).

difference in the intensity and width of the observed in-plane dipolar peaks in the EELS obtained from different regions of the particle: Ag side, triple point and Co side. Moreover, the electron-energy loss at $\sim$3.60 $\pm$ 0.15 eV was observed strongly only from the electrons beam at the Ag side and triple points, and rather weak for the electron beam from the Co side. This peak at the near ultraviolet region corresponds to QP mode [159]. Correlating this observation with the general results obtained from optical absorption spectra, we found that the quadrupole mode (observed in optical excitation) should be integrated into the quasiplanar mode in such particles for the given energy resolution.

Of particular interest from the electron energy-loss spectra obtained near from the triple point was the emergence of an additional electron energy-loss mode at $\sim$2.73 eV. This peak was observed to be localized more than the in-plane dipole mode and less than QP plasmon mode. Further investigation confirmed that the peak becomes progressively weaker as the EELS are taken either in Co or in Ag side, thereby confirming the origination of peak from interface of Co and Ag as shown in Fig 3.4(a), (b) and (c). Surprisingly, this peak was absent from optical spectra from an ensemble of CoAg nanoparticles with normal incidence. The compelling reason is that the plasmon oscillation associated with interface could be an out-of-plane oscillation. Since the incident light source in our optical experiment is normal to the substrate, the electric field vector associated with it should only be able to excite in-plane dipole mode. However, a swift electron beam can excite both in-plane and out of plane plasmon oscillation [162].

3.4 Discussion

The electric field due to swift electron beam passing nearby the nanoparticles induce surface plasmon oscillation in the metallic system [162]. The schematic image for the plasmon oscillation direction for CoAg nanoparticles is shown in Fig. 3.5. From electron energy-loss spectra, we observed the QP mode at 3.60 $\pm$ 0.15 eV, which is more localized compared to in-plane dipole at 2.25 $\pm$ 0.05 eV from the CoAg nanoparticle. Under more scrutiny in Table **??**, we saw that both the QP plasmon mode and in-plane dipole mode varies slightly with the location of beam position near the nanoparticles. Basically, one expects the resonance

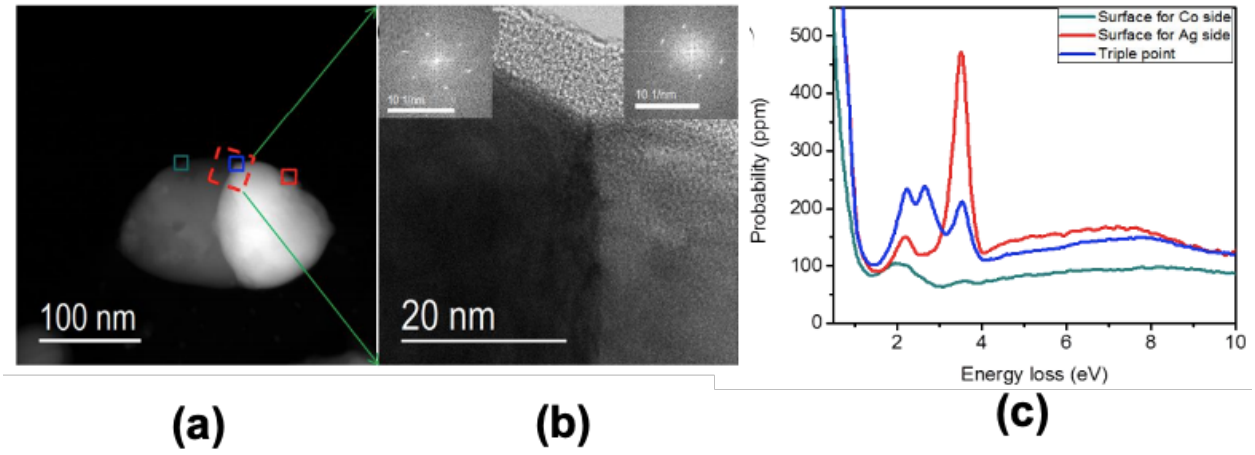

Figure 3.3: (a) Z-contrast image of the epitaxial CoAg bimetallic nanoparticle. The dark side is Co, the bright side is Ag (b) The HRTEM image from the red dashed square region in figure (a). Inset shows the FFT from Ag and Co side respectively to right and left (c) The experimental EELS spectra for the surface of Co side (dark cyan), the surface of Ag side (red) and the triple point (blue), respectively. And the spectra were taken from the regions corresponding to the marked square areas in (a) with the same color. [1]

Table 3.1: LSPR peaks positions, width, plasmon energy, area and quality factor from the EELS spectra in Figure 3.3 [1]

Plasmon modes		Ag	Tripple point	Co
In-plane dipole	Position (E_{max})	2.17	2.19	1.98
	Width (eV)	0.64	0.58	1.65
	Plasmon energy (eV)	2.22	2.23	2.30
	Area (ppm)	172.01	221.63	157.96
	Quality factor (Q)	3.39	3.77	1.20
Interface	Position (E_{max})		2.71	
	Width (eV)		0.52	
	Plasmon energy (eV)		2.73	
	Area (ppm)		205.09	
	Quality factor (Q)		5.29	
Quasi-plannar	Position (E_{max})	3.45	3.53	3.64
	Width (eV)	0.50	0.63	1.24
	Plasmon energy (eV)	3.47	3.56	3.74
	Area (ppm)	316.60	230.99	56.41
	Quality factor (Q)	6.90	5.60	2.93

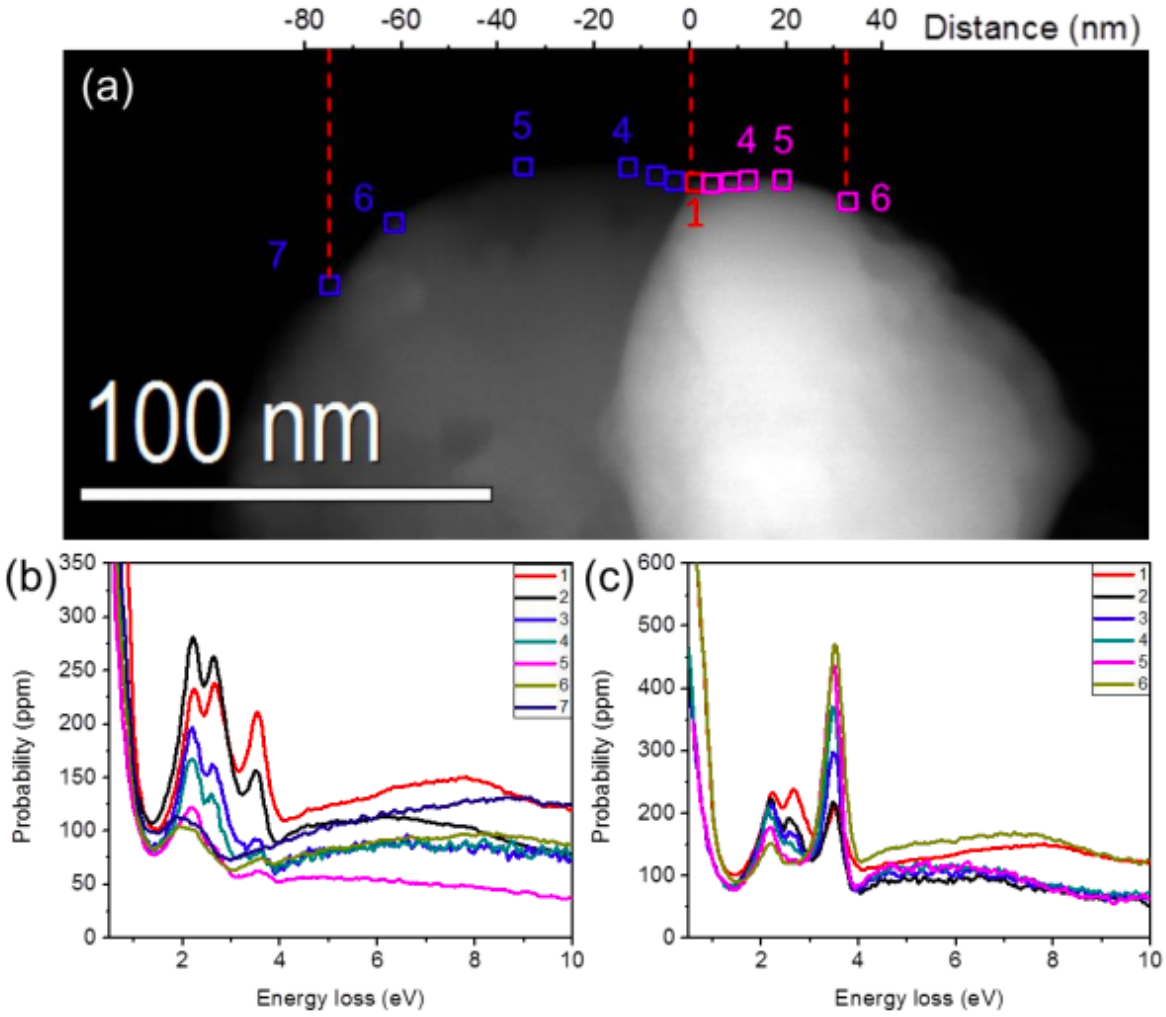

Figure 3.4: (a) Z-contrast image of AgCo NP. The selected regions of the surface were divided by Co side (blue squares) and Ag side (pink squares) from the triple point. The distance of the selected region from the triple point was indexed above the Z- contrast image. (b) and (c) Experimental EELS spectra of the LSPR were taken from the surface of the Co side and Ag side, respectively. All the taken regions were numbered in (a) [1]

energy of in-plane dipole and QP mode on such plasmonic systems is identical irrespective of the beam position. This is because, in the bimetallic system like CoAg, there are two possible ways of plasmon energy interaction from one metal to another metal viz. by (i) resonance energy transfer and (ii) direct electron transfer [163]. Since, there is no relative energy gap between two metallic contacts, the only possible resonance energy mechanism is by charge transfer. In other words, the electrons cloud in the Co side and Ag side interact in such a way that they oscillate as a whole entity in the same phase. This argument was further verified from our optical excitation experiment in which pure Ag and CoAg systems of comparable sizes have similar in-plane dipole plasmon resonance frequency. However, due to the screening effect and relatively low density of charges in the Co side, the plasmon resonance was damped while it was excited from the electron beam on the Co side as evident from Fig. 3.3(c). The other contribution for small change (∼0.15 eV) in plasmon energy with different positions can be attributed to the radiation damage of the electron beam in carbon substrates over a period of measurement time [160]. It should be noted that the isolated Eigen dipole energy of intrinsic Co's oscillator does not fall in the UV-Vis-NIR energy range (1.5 eV-4.2 eV) studied here.

As we well identified and characterized the in-plane dipole, quadrupole and QP modes by using photons and electrons sources, the emergence of an additional peak only at or near the triple point of Co, Ag and vacuum is surprising. We hypothesize that this highly localized peak observed in the CoAg nanoparticle could be due to independent oscillation of modified plasma with intrinsic frequency of $\omega_{CoAg} = \sqrt{\frac{N_{CoAg}e^2}{\epsilon m^*}}$ along the interface regions, where N_{CoAg} and m*are modified charge density and effective electron mass in the interface due to modified chemistry in the interface. We further characterized the quality factor of this peak by comparing it with in-plane dipole and QP mode. As we summarized in Table 3.1. the quality factor of this interface plasmon resonance is higher than the dipole mode but less than the QP mode.

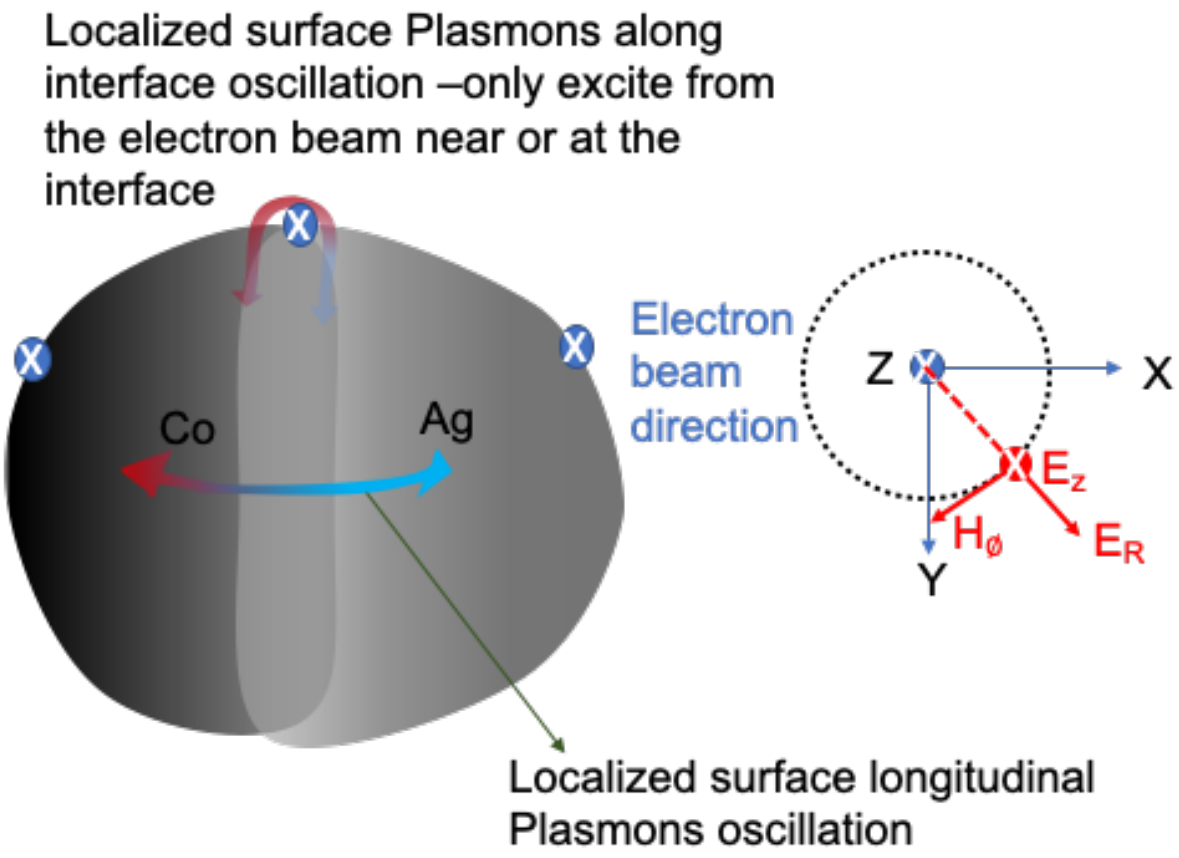

Figure 3.5: Schematic of plasma oscillation in CoAg nanoparticle

3.5 Acknowledgment

The authors acknowledge support by NSF grant ECCS1607874 and U.S. Department of Energy, Office of Science, Basic Energy Sciences, Materials Sciences and Engineering Division. The authors also want to thank Dr. Abhinav Malasi for experimental assistance.

Chapter 4

Nano-second switchable LSPR in Ag nanoparticles by morphology changing

(Published in IOP Nanotechnology 31 (2020) 355503 [102])

4.1 Introduction

Metallic nanoparticles exhibit unique properties when their size is less than or comparable to the incident light wavelength. One of these properties is the localized surface plasmon resonance (LSPR), where collective oscillation of free surface electron gas by incident electromagnetic field result in specific wavelength absorption. This specific wavelength depends on the refractive index (RI) of the surrounding medium, composition of the metal, and the geometrical features of the particle such as its shape and aspect ratio [13, 28, 37, 39, 164]. The role of RI on plasmonic behavior has been well studied in applications towards LSPR based sensing, solar energy harvesting, and biomolecular detection [4, 114, 115, 116, 117, 165, 166, 167, 168, 169, 170]. Amongst the next generation of plasmonic effects that are being sought after, one is the active control of LSPR in fast time scales. The ultra-fast control of LSPR tuning in relation to optical switching in specific wavelength regions can potentially lead to applications in smart windows, optical biosensing, optical filtering and photochromic effects [4, 39, 164, 171].

Another mechanism that has been used to modulate the LSPR characteristics, such as resonance wavelength and intensity is by modifying the surrounding media, such as by changing the dielectric properties, modifying the charge carrier density, and spacing between the nanoscale materials. The local dielectric environment and the resulting refractive index can be changed in many ways. For instance, the refractive indices of dye molecules have been altered within the time scale of a few seconds under exposure by a HeCd laser with subsequent LSPR shift from the supporting Au nanorods of $\sim$ 20 nm in the visible wavelength [119]. Phase-change materials like Germanium Antimony Telluride (Ge_3Sb_2Te6) also offers reversible refractive index response to femtosecond pulsed laser heating with $\sim$ 1000 nm shift in the resonance wavelength in the mid-infrared regime, as seen with Au or Al plasmonics rods [120, 121]. Changing the gap between nearby plasmonic nanoparticles has been demonstrated with negatively charged Au nanoparticles covered with bis(p- sulfonatophenyl)-phenylphosphine and plasmonic shifts of $\sim$ 50 nm in visible range have been achieved in the time scale of a few seconds [122]. Graphene has recently been realized as a tunable plasmonic media due to electrically-controllable charged carrier density but appears to be limited to switching in the millisecond to second time scales due to RC phase delay [123].

4.2 Methods

4.2.1 Dynamic Maxwell Garnett Theory

The Maxwell-Garnet (M-G) theory has been applied to model the optical properties of nanocomposite materials such as metallic islands or metallic nanoparticles embedded in a host dielectric comprised partially of a solid substrate and a surrounding media like air [57, 172, 173, 174]. In this model, the effective complex dielectric function ε_{eff} for the system is given by:

$$\varepsilon_{eff} = \varepsilon_{host}\frac{[L\varepsilon_m + (1-L)\varepsilon_{host} + f(1-L)(\varepsilon_m - \varepsilon_{host})}{L\varepsilon_m + (1-L)\varepsilon_{host} - fL(\varepsilon_m - \varepsilon_{host})} \tag{4.1}$$

where, $\varepsilon_{host} = \sigma\varepsilon_{substrate} + (1-\sigma)\varepsilon_o$ is the effective dielectric contribution of the host medium composed of air and substrate weighted by the factor σ. The weighting factor σ is the ratio of particle contact area to the substrate to the particle surface area exposed to air. The complex dielectric function of metallic particles is given by ε_m and f is the particle filling factor given by the volume fraction of nanoparticles within the system. L is the depolarization factor of nanoparticles. The dynamic form of the M-G theory [175] proposes a wavelength dependent depolarization factor for the bigger particle of radius r, defined as

$$L_{eff} = L - \frac{1}{3}K^2r^2 - \frac{2}{3}iK^3r^3 \tag{4.2}$$

Here, $K = \frac{2\pi r\sqrt{\varepsilon_{host}}}{\lambda}$ and r is radius of the nanoparticles. Thus, retardation as well as damping induced radiation loss is included in the L_{eff}. The transmission spectra of nanoparticle system is obtained by matrix transformation method with the extinction spectrum calculated by $E = Log(T_o/T_{Ag})$, where T_o and T_{Ag} are the effective transmittance of silver free and silver nanoparticle composite system respectively.

This effective medium theory predicts several interesting optical and plasmonic properties of the nanocomposite systems, including change in plasmonic resonance wavelength due to change in particle shape (depolarization factors), volume fraction as well as due to change in the weighting factor σ as a result of particle shape or contact angle changes. For instance, Fig. 4.1(a) shows the extinction spectra for different values of σ, for particles of fixed radius $r = 25$ nm and volume fraction of $f = 0.2$. The different values of σ correspond to changing the particle contact angle with the substrate. For example, $\sigma = 0$ represents a perfect spherical particle, i.e. contact angle of 180°, while $\sigma = 0.5$ represents a hemispherical particle with contact angle of 90°. As Fig. 4.1(a) shows, the peak in the extinction spectra corresponding to the dipolar plasmon resonance from the nanoparticles red shifts with decreasing contact angle. This is consistent with the fact that the contact area of the particle with the substrate, which has higher dielectric function than air, increases with decreasing contact angle, thus producing a red shift. Another useful result shown in the inset of Fig. 4.1(a) is that for

nanoparticles of similar volume, the resonance peak shifts to higher wavelengths for the particle with larger contact angle.

In Fig. 4.1(b), the extinction spectra for various volume fraction is shown for particles with fixed contact angle (i.e. fixed $\sigma = 0.1$) and radius $r = 25$ nm . The key results are the substantial change in the intensity of the extinction spectra and the relative change in intensity of the dipolar to quadrupolar peaks. The overall intensity increases with increasing volume fraction f, consistent with the increased optical scattering as the number of nanoparticles per unit volume is increased. While a slight red shift in the wavelength position of the dipolar or quadrupolar plasmonic peaks is seen, the relative intensity of the two peaks changes significantly, with the quadrupolar dominating at lower fractions and the dipolar at larger fractions. Overall, the key takeaways from the modeling results are that increasing the particle contact angle and/or size, increases the plasmonic resonance wavelength position, while changing volume fraction changes the intensity significantly.

4.2.2 Experiments

Ag films of 9 ± 0.2 nm thickness were deposited in a base vacuum pressure of 2×10^{-8} torr on fused Quartz substrates at room temperature by the e-beam evaporation method (Model Mantis QUAD-EV-C). Prior to deposition, the substrates were cleaned ultrasonically in ethanol, acetone and DI water, for 30 minutes at each step respectively. After deposition, the films were stored in a metallic box placed within a desiccator. Single pulse laser irradiation under glycerol fluid was performed on the Ag film with a 266 nm UV laser having a pulse width of 9 ns (Model Quanta-Ray Pro-Series Nd:YAG LASER). The single pulse irradiation was performed at normal incidence by the linearly polarized laser beam of area 1 mm^2. This technique was developed recently to synthesize near-spherical nanoparticles on quartz substrates via a dewetting process, as reported in ref. [138]. The resulting nanostructures were then investigated by high resolution imaging using a ZEISS Merlin scanning electron microscope (SEM) in plan and side view orientations. Plasmon induced optical transmission in the UV-Vis region were recorded by an HR2000 + ES spectrometer from Ocean Optics consisting of a broadband halogen/deuterium lamp as a light source. The transmission spectra were later converted into absorption spectra by using the Beer-Lambert law of optical

absorption. The nanostructures obtained under glycerol irradiation were near-spherical in shape with a contact angle of $166^\circ \pm 9$ as evidenced by SEM imaging and analyzed by ImageJ [176]. This sample was again irradiated by a single laser pulse in air and the resulting morphology and optical properties were studied. These nanostructures were near-hemispherical in shape, with a contact angle of $103^\circ \pm 7$. The laser fluence used for these experiments was 80 mJ/cm^2 for the glycerol as well as air irradiations. The hemispherical shaped nanoparticles were subsequently irradiated under glycerol by a single pulse and its optical absorption spectra and shape were studied. This cycle of air+glycerol irradiation was repeated up to ten times and corresponding absorption spectra were studied. The schematic diagram of the experimental process is shown in the Figure 4.2.

4.3 Results

The first part of the study was to investigate the contact angle switching behavior following irradiation by a single nanosecond laser pulse. The Ag thin films of thickness 9 ± 0.2 nm were prepared and subjected to pulsed laser irradiation. The morphology of the as-prepared film and the corresponding absorption spectra are shown in supplementary materials. The as-prepared film did not possess distinct spatially separated particles. In addition, the film did not exhibit any plasmon induced resonance in the visible region. The typical morphology of Ag nanoparticles synthesized by laser dewetting of the Ag thin film under glycerol is shown in Figure 4.3(a). Figure 4.3(b) is the side view SEM showing the near-spherical nature of the particles while Figure 4.3(c) is the histogram showing the particle size distribution. The average diameter of the spherical particles was calculated to be 51 ± 23 nm. This system was exposed to a single laser pulse of fluence of 80 mJ/cm^2 in air environment. The morphology of the resulting particles is shown in Figure 4.3(d) while the side view SEM image of the nanoparticles is shown in Figure 4.3(e). The major differences from the initial nanoparticle characteristics is the increase in average particle size (with decrease in number density), as evident comparing Figure 4.3(a) and (d) as well as an increase in contact angle to a nearly hemispherical shape, as seen in Figure 4.3(e). Figure 4.3(f) shows a histogram for the particle size distribution, confirming an increased average diameter of 102 ± 32 nm. From

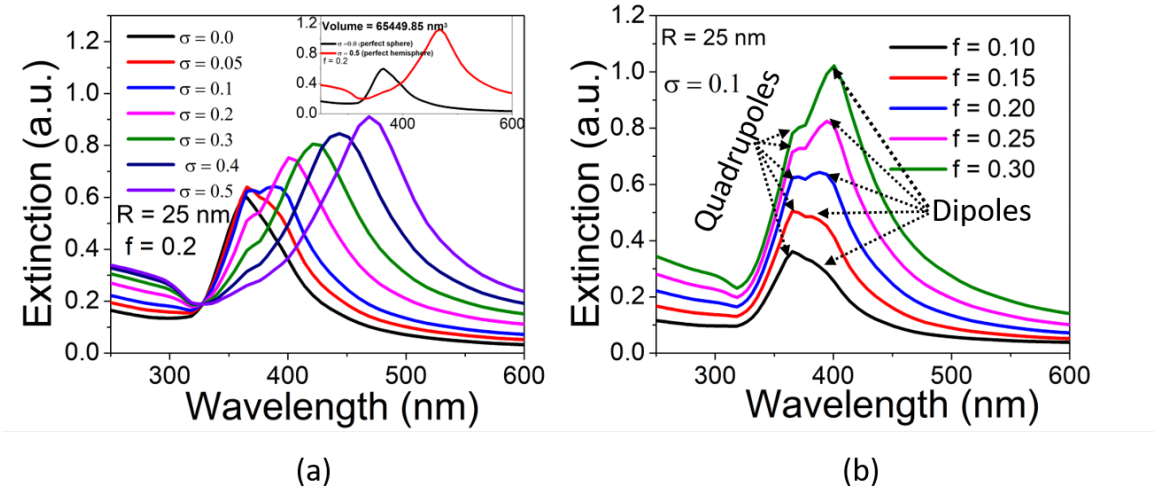

Figure 4.1: Extinction spectra of (a) nanoparticles with radius $r = 25$ nm, $f = 0.2$ and different σ values. Inset shows the extinction spectra for perfect sphere and hemisphere of constant volume (b) nanoparticles of different f values but constant $r = 25$ nm and $\sigma = 0.1$, as predicted by dynamic Maxwell -Garnett theory.

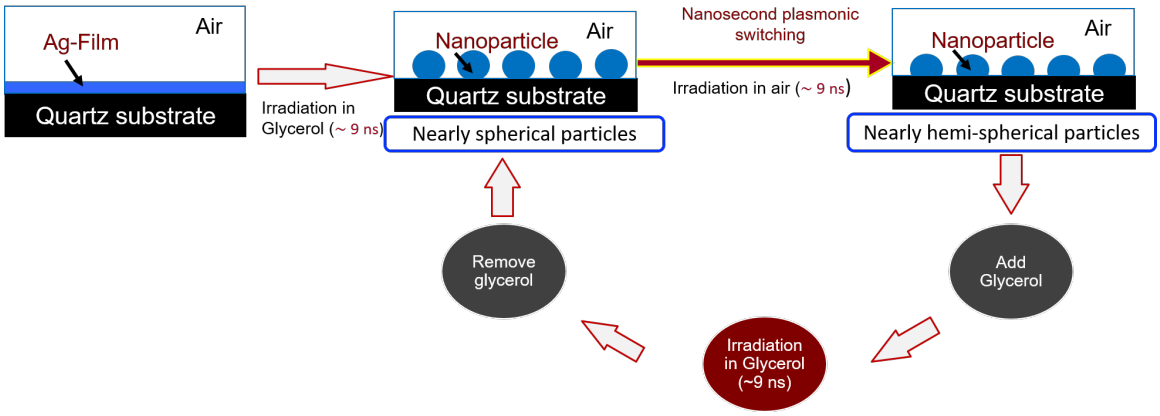

Figure 4.2: Schematic diagram of the experimental procedure involved in creating spherical nanoparticles, switching the contact angle to hemispherical case by using single pulse laser irradiation in air, and resetting the contact angle to spherical shape by single pulse irradiation in glycerol

these experimental measurements, it was clear that the particle contact angle was changing from the initial spherical to hemispherical shape following a single pulse irradiation in air, and was also accompanied by an increase in the particle diameter.

The plasmon induced absorption spectra for the two systems (i.e. near-spherical and air-irradiated near-hemispherical case) are shown in Figure 4.4(a). As evident from Figure 4.4(a), the intensity as well as position of the LSPR dipole and quadrupole modes changed dramatically in going from the spherical to hemispherical system. The dipolar plasmon position red shifted and its intensity increased in going from the spherical to hemispherical case. On the other hand, the quadrupolar plasmonic peak position blue shifted while its intensity decreased in going from the spherical to hemispherical case. The hemispherical particles have more flat surface along the substrate making less efficient quadrupole polarization. This can also be explained theoretically by the higher value of depolarization factor ($\frac{1}{2.19}$) in hemispherical case than in spherical case ($\frac{1}{3}$) in transverse direction although the vertical dimension is almost same in both cases [177]. This result established that the shape change was accompanied by a large change in the optical plasmonic properties, namely wavelength and intensity change of the plasmonic resonances.

In the next phase of our experiments, we investigated the ability to reset the optical properties of the system back to its initial state as well as test whether it is possible to reuse this system for multiple cycles of optical switching. We subjected the near-hemispherical system to laser irradiation under glycerol with a single laser pulse and plasmon induced absorbance for the resulting system was recorded. In Figure 4.4(a), the result of this "resetting" single pulse is shown by comparing its optical behavior to that of the original near-spherical system as well as the first switched state (i.e. the near-hemispherical state). The "reset" system has quite similar optical spectrum in terms of wavelength positions to the original near-spherical system. However, the intensity of the reset system appears lower than the original near-spherical state. In Figure 4.4(b), the representative optical data from first, fifth and tenth switching and reset cycles, are shown. The optical data for all optical cycles (1 to 10) is presented in the supplementary materials. Like cycle 1, the subsequent cycles show similar plasmonic resonance positions for the reset state (shown by blue curves)

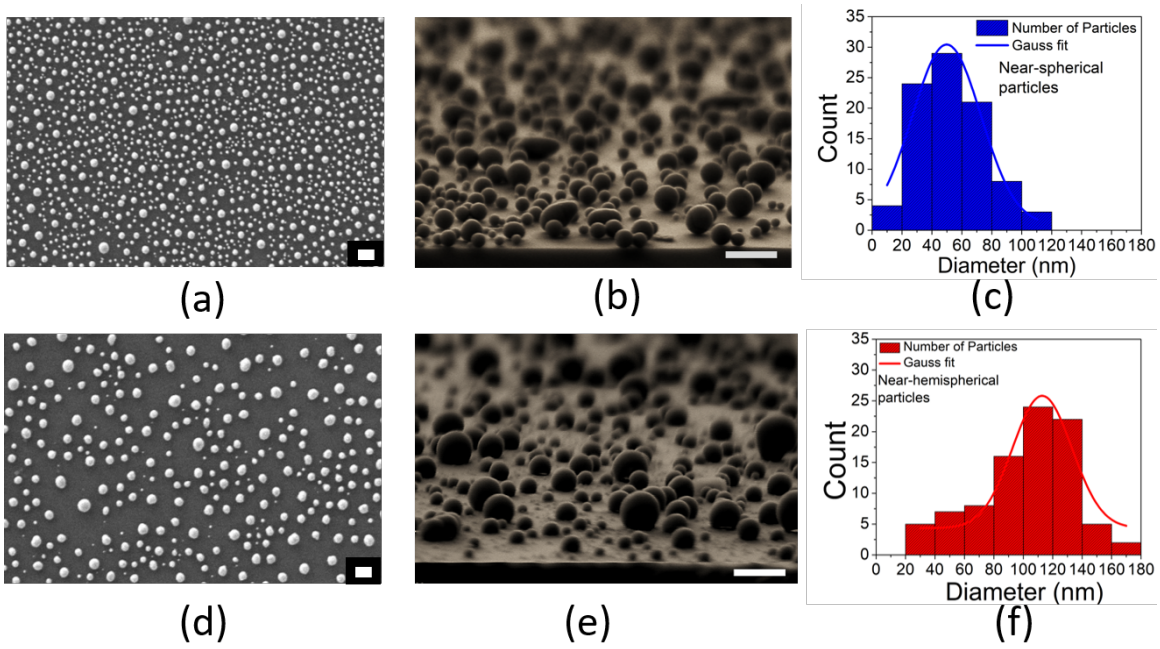

Figure 4.3: (a) Plan view SEM image of Ag nanoparticles synthesized under glycerol. (b) Side view SEM image showing that the nanoparticles have nearly spherical shape due to the large contact angle. (c) Histogram of particles in (a) showing the size distribution. (d) Plan view SEM image of nanoparticles following irradiation of system (a) in air. (b) Side view SEM image showing that the nanoparticles have nearly hemispherical shape. (e) Histogram of particles in (d) showing the size distribution (the scale bars in the figures are 200 nm)

or switched state (shown by red curves), while the intensity decreases significantly with increasing number of cycles.

4.4 Analysis and discussion

The goal of this work was to study switching and reversibility of plasmon induced resonance absorption modes in silver nanoparticle arrays mainly arising due to setting and resetting of contact angles of Ag nanoparticles following melting by a single pulse laser. We have built our switching idea based on a newly discovered effect in which the shape of the particle can be changed based on the conditions under when the particle is irradiated. In a recent work by our group [138], we demonstrated that Ag nanoparticles fabricated by laser melting in air, water and glycerol environments yielded significantly different shapes, with the glycerol leading to a near-spherical shape, while air produced near-hemispherical shape particles. This shape difference was attributed to different interfacial energies involved, with the glycerol-substrate and glycerol-Ag interfacial energies being larger than the air-substrate and air-Ag interfacial energy, this leading to higher contact angles for the glycerol case, as predicted by Young's equation [178].

Figure 4.5 (a) and (b) shows the SEM image and histogram of the nanoparticle size distribution following the tenth switching process. The analysis of the volume of the nanoparticles after the first and tenth switching process showed the significant detachment/loss of nanoparticles. Indeed, we observed the loss of 65 $\pm$ 1 % by volume. The most likely reason for this loss is the weak adhesion of Ag nanoparticles with the underlying substrate, making it easy for the near-spherical nanoparticles to be removed during laser irradiation in the glycerol ambient (setting/resetting process). This reason was further supported by analysis of volume of the particles before and after the first switching process (irradiated in air) where the loss in particles by volume was found to be 0.3 %. This small discrepancy in volume falls within the uncertainty value obtained during analysis. In essence, we didn't see loss of any particles by volume in switching process (irradiation in air) while an average of 6.5 % of the particles by volumes were lost during each set/reset process (irradiation in glycerol).

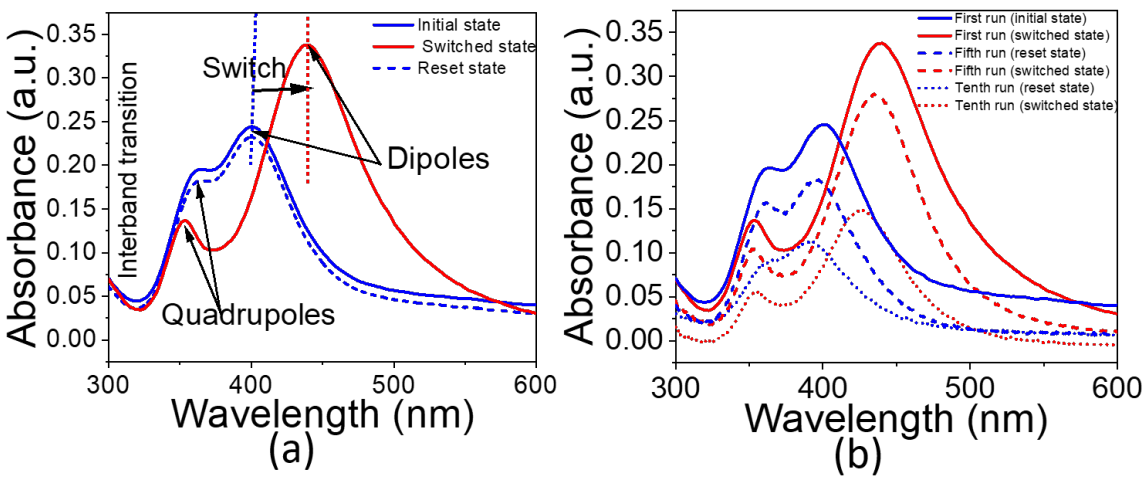

Figure 4.4: LSPR resonant absorption spectra of (a) first set, switched and reset states (b) first, fifth and tenth cycle of set/reset and switched states

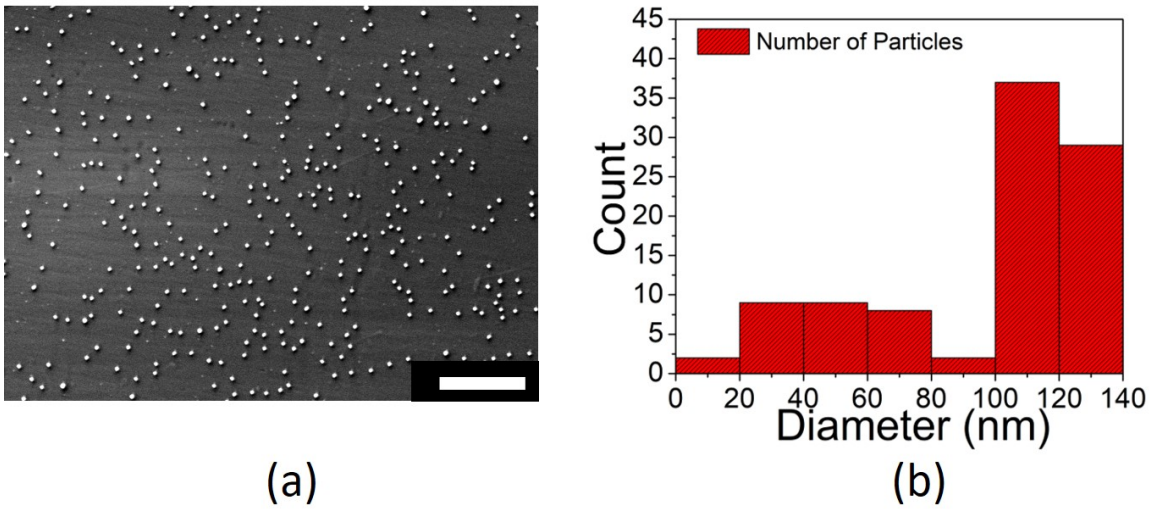

Figure 4.5: (a) Plan view SEM image of Ag nanoparticles after the 10 cycles (the scale bar is 1 μm) (b) Histogram of particles showing size distribution with average particles diameter 103 $\pm$ 33 nm.

Despite the material loss, our results provide some very useful overall findings that can guide future investigations of cyclic plasmonic switching of resonance wavelengths and intensities in plasmonically passive substrates like fused Qz. From Figure 4.4(a), we confirmed that the resonance plasmonic wavelength location as well as the intensity, changes substantially under the single pulse switching from the initial array comprising of near-spherical particles Figure 4.3(b) to the near-hemispherical case as shown in Figure 4.3(d). The dipolar peak red shifted from 399 nm to 439 nm, while the dipole resonance intensity increased by $45 \pm 5\,\%$. Both these findings are consistent with the contact angle change effect, as also predicted by the dynamic form of M-G theory, shown previously in Figure 4.1(a). However, the investigation of resetting the switched near-hemispherical system back to the near-spherical state revealed that while the resonance peak positions, as shown by the dashed line in Figure 4.4(a), appeared to match quite well with the original state [solid blue line in Figure 4.4(a)] a clear decrease in intensity was observed. This effect was further compounded over multiple cycles of switching and resetting, as observed in Figure 4.4(b).

Fig. 4.6(a), compares the experimental and simulated optical absorbance spectra of Ag nanoparticles in quartz substrate for the first cycle from which the effective volume fraction was calculated to be 0.19. The bulk real and imaginary component of refractive indices of Ag for our simulations was taken from Johnson et al[15]. The simulated optical spectra more or less overlap the experimental spectra and we attributed the small mismatch to the surface oxidation of the system, which was not taken into consideration in the simulation. After optimization of the simulated spectra with experimental spectra for each cycle (supplementary materials), the effective volume fraction for every cycle was calculated. Thus obtained effective volume fractions were used to compute the complex refractive indices for each set/reset and switched cycles which are shown in Figure 4.6 (b)-(e). The refractive indices of the plasmonic system provide useful information about the optical properties of the system. The real part of the dielectric function gives the information about the polarization of the system while the imaginary part controls the dissipation of the energy into the medium [179]. We found a systematic decrease in complex refractive index near the LSPR resonance wavelength following each cycle, which is attributed to the change in effective volume fraction due to a decrease in the particles by volume. Quantitatively, the imaginary

values of refractive indices decreased by 54 % in case of near-spherical particles and 58 % in case of near-hemispherical particles in their resonance wavelengths when the effective volume fractions decreased by 63.5 %. The other important observation was that the real values of refractive indices for the near-spherical particles (0.92) are smaller than the refractive indices for the near-hemispherical particles (1.02), near their resonance wavelengths. In addition, the near-hemispherical particles show larger difference in the refractive indices over the visible range (0.91 at 400 nm to 1.18 at 470 nm). Physically, this effect could be explained by local field enhancement as the near-hemispherical particles have more sharp edge in contact with the substrate as compared to the spherical particles where most of the hot electrons concentrate.

To better quantify the plasmonic behavior with switching and resetting over multiple cycles, the measured change in wavelength position for the dipolar and quadrupolar peaks were studied. The location of the dipole and quadrupole wavelengths for each of the switched and reset states during the 10 cycles is shown in Figure 4.7(a). From this, it was evident that a small but systematic change in the position of the dipolar and quadrupolar resonance was clearly occurring following each cycle. The blue shift in dipole resonance peak for the near-hemispherical particles [closed red squares in Figure 4.7(a)] following 10 cycles of switching was 12 ± 0.6 nm corresponding to an average blue shift of 1.2 nm per cycle while that for the near-spherical particles [closed blue sphere in Figure 4.7(a)] following 10 cycles of resetting was 9 ± 0.4 nm with an average blue shift of ~ 0.9 nm per cycle. The average shift of quadrupolar peaks were ~ 0.3 nm per cycle for both hemispherical and spherical particles. To understand the reason for this change, ,the *overall* dipole and quadrupole wavelength shifts occurring for each switching cycle, i.e. from near-spherical to near-hemispherical state, is shown in Figure 4.7(b). Average shifts over the 10 cycles of 38.5 ± 1.6 nm and 10 ± 0.5 nm were found for the dipolar and quadrupolar peaks respectively. However, a small but systematic decrease in dipolar wavelength shift (filled green squares in figure) with a slope of -0.5 nm/cycle and in quadrupolar wavelength (filled purple triangles in figure), with a slope of 0.1 nm/cycle was evident over the 10 cycles. This small but systematic shift in the resonance position was attributed to a change in the volume fraction of particles after each switching as well as resetting step. To support this idea, a similar change in dipolar

and quadrupolar shift was obtained from the dynamic M-G theory computed for change in effective volume fraction for near-spherical and near-hemispherical particle arrays for each cycle, and this is shown in Figure 4.7(c). Quantitatively, the systematic decrease in dipole shift of 0.5 nm and quadrupole shift of 0.1 nm was obtained for the 6.35 % change in effective volume fraction of the particles. In essence, the dynamic form of M-G theory predicts the decrease in effective refractive index with decrease in effective volume fraction of the particles resulting in blue shift of the resonance position. While we have observed a small increase in the average size of particles, as shown in Figure 4.5, the decrease in effective refractive index due to detachment of the particles during irradiation under glycerol ambient of the system appears to largely account for the overall small blue shift of the system in set/reset and switched states following each cycle.

Next, the stability of the system in terms of intensity of the resonant dipole and quadrupole intensity over the 10 cycles was analyzed. Figure 4.8(a) shows the changes in resonant dipole and quadrupole intensities over the 10 cycles studied here. Overall, the dipole intensity of the near-spherical [filled blue sphere in Figure 4.8(a)] and near-hemispherical particle [filled red squares in Figure 4.8(a)] decreased by 41 $\pm$1.2%and 58 $\pm$1.5% respectively while quadrupole intensities [filled triangles in Figure 4.8(a)] decreased by 56 $\pm$1.4% and 61 $\pm$1.8 % respectively. This intensity change behavior was fitted with dynamic M-G theory when there is a decrease in the volume fraction of particles as shown in Figure 4.8(b). Quantitatively, this overall decrease in dipole and quadrupole intensities of near-spherical and near-hemispherical particles state over ten cycles was attributed for 63.5 $\pm$0.5% decrease in effective volume fraction of the particles obtained according to the dynamic M-G theory. This value obtained from dynamic M-G theory is close to the experimental value of 65 $\pm$1% which was obtained by SEM image analysis from Figure 4.3 (e) and 4.5 (a). The discrepancy of $\sim$ 1.5 % from the dynamic M-G theory can be attributed to boundary effect and the homogeneity of the distribution of the particles in the medium [180]. In effect, the overall scattering strength of the nanoparticle array decreases as the number of particles per unit volume (i.e. the volume fraction) goes down.

Our analysis provides an interesting consequence of the particle contact angle in the context of the plasmon intensity. Hemispherical particles generally combine a high surface

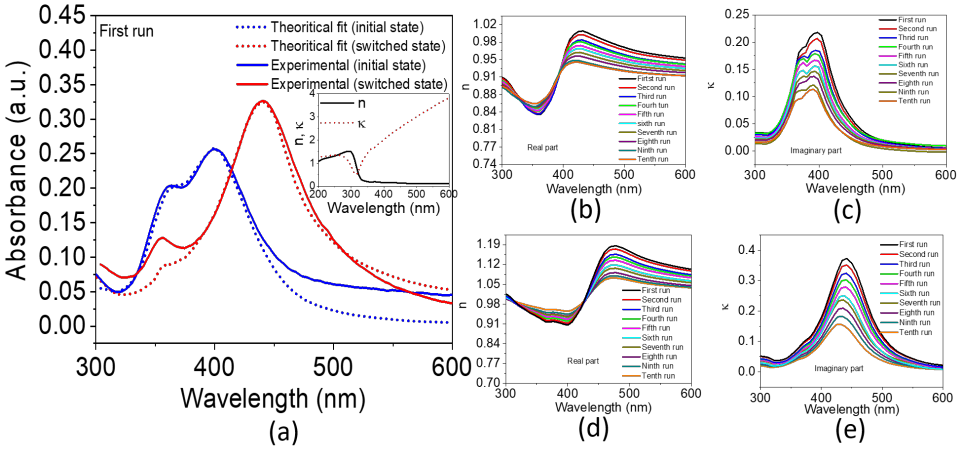

Figure 4.6: (a) Measured and simulated absorption spectra of Ag nanoparticles in Qz for the initial state and first switched state. The inset shows the bulk real and imaginary component of refractive indices taken as a reference for those simulations [15], (b) the real and (c) imaginary components of refractive indices for the near-spherical particles in Quartz for each set/reset state, (d) the real and (e) imaginary components of refractive indices for the near-hemispherical particles in Quartz for each switched state.

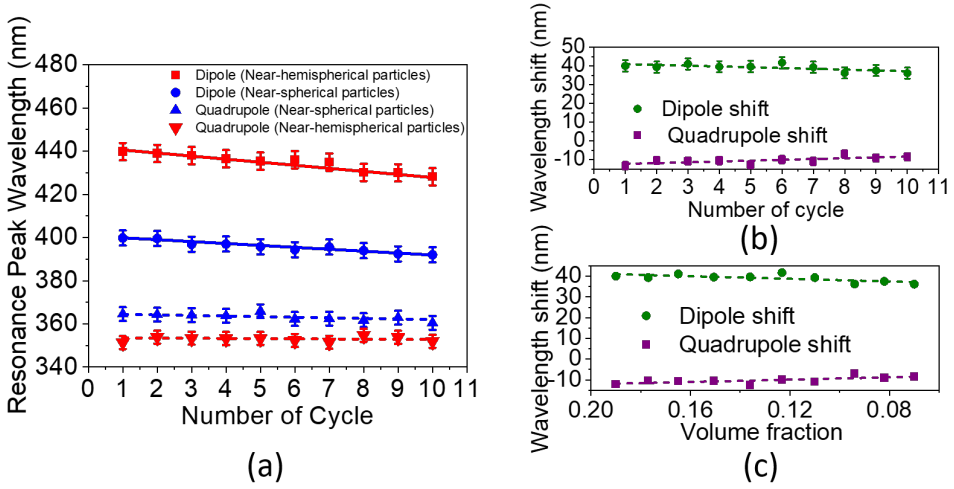

Figure 4.7: The variation of resonant (a) dipole and quadrupole peak wavelength (b) the experimentally measured change in net dipole and quadrupole shift with increasing number of cycle (c) the theoretically calculated change in net dipole and quadrupole shift from near-spherical case to near-hemispherical case with varying volume fraction according to dynamic M-G theory.

to volume ratio along with a strong dipole resonance intensity [181] making them useful in plasmonic applications. However, the choice of which contact angle to use for a given plasmonic application is also linked to the the wavelength range of interest. As we found here through a detailed analysis of the plasmon intensity in the wavelength range from 300 nm to 600 nm, there is more intense plasmon induced absorption by the spherical particles over the hemispherical particles for wavelengths below 400 nm, provided that the volume density is kept the same, as shown in Figure 4.9.

4.5 Acknowledgement

The authors acknowledge support by NSF grant ECCS-1607874. V.P.S acknowledges support by CBET-1402962 whereas, G.D acknowledge support by U.S. Department of Energy, Office of Science, Basic Energy Sciences, Materials Sciences and Engineering Division.

4.6 Supplementary materials

Figure 4.10 shows the asprepared Ag (9 nm) thin film on quartz substrate and its corresponding optical transmission. spectra. Figure 4.11 shows the optical transmission spectra for the various cycles of laser irradiation.

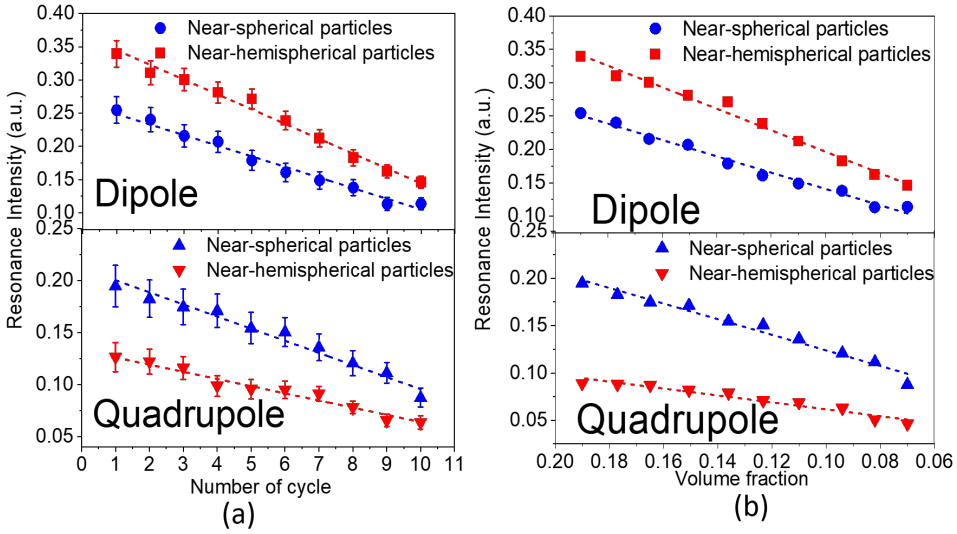

Figure 4.8: The variation of (a) dipole and quadrupole intensity for near-spherical and near-hemispherical particles with increasing number of cycle. The variation(b) dipole quadrupole intensity for near-spherical and near-hemispherical particles with decrease in volume fraction calculated from dynamic M-G theory.

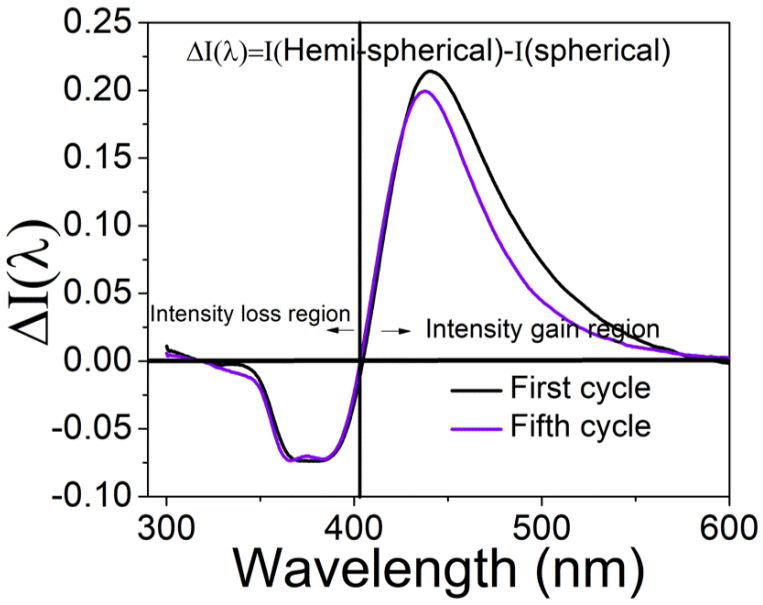

Figure 4.9: Overall plasmon induced absorption spectrum changes in the switching process as a function of wavelength

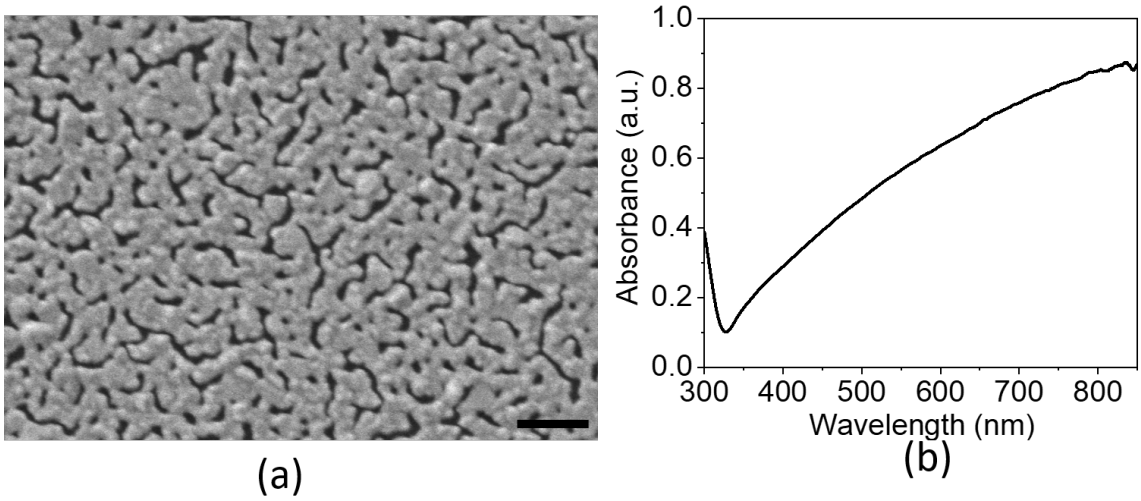

Figure 4.10: (a) As-prepared Ag thin film of thickness 9 nm (scale bar is 200 nm) (b) corresponding transmission optical spectra

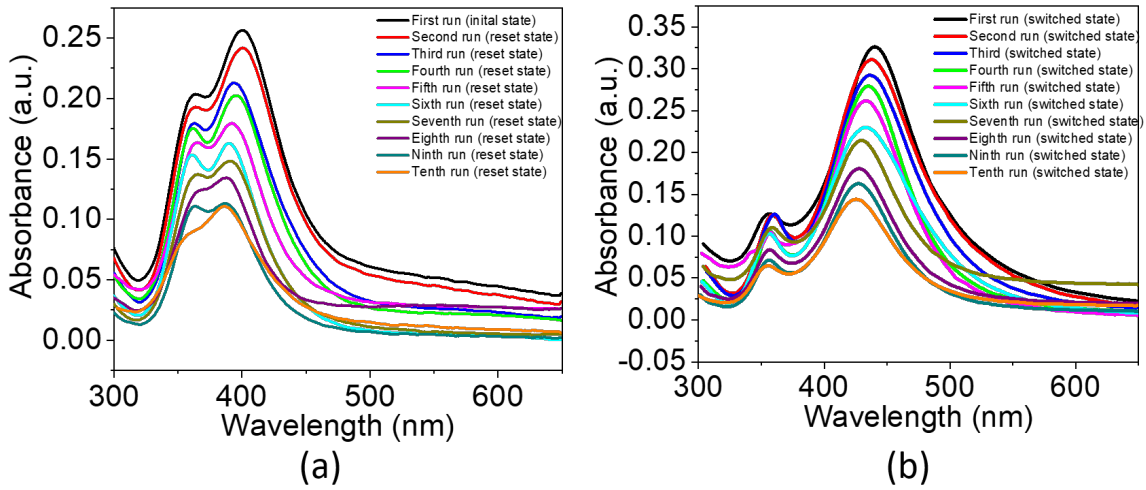

Figure 4.11: (a) As-prepared Ag thin film of thickness 9 nm (scale bar is 200 nm) (b) corresponding transmission optical spectra

Chapter 5

Bimetallic Fe-Ag arrays with extraordinary nonlinear refraction and nonlinear Faraday rotation at telecommunication wavelength (1550 nm)

5.1 Introduction

In this work, we report the discovery of giant negative nonlinear refraction and nonlinear Faraday rotation at 1550 nm using an array of bimetallic Fe-Ag nanopyramids. This system exhibited a large third order nonlinear refractive index (n_2 = -2.32 cm^2/GW) and nonlinear figure of merit (F = 2.3). The same system also exhibited a photoinduced nonlinear Faraday rotation up to 2.5 radian/μm at a magnetic field of 0.5 T. The nonlinear response was dependent on the degree of overlap of the Fe nanopyramid on the Ag nanopyramid which influences the strength of plasmon induced dipoles on the Ag nanopyramid. This nanoscale system opens up a rich new set of possibilities in utilizing magneto-plasmonic materials to miniaturize future multifunctional devices at telecommunication wavelengths.

One class of interesting metallic systems are bimetallic plasmonic nanostructures which show either improved materials stability and/or unusual optical and magneto-optical properties in terms of activity and stability arising from synergetic effects. In the past, metals like Fe, Co, Ni, Pt, Pd and Al have been combined with the noble metals Ag, Au and Cu to enhance the plasmonic and magneto-plasmonic properties. For example, ferroplasmons have been discovered in Ag-Co bimetallic nanoparticles, in which strong surface plasmons have been observed in the Co side of the metallic system while preserving its ferromagnetism [22, 23]. Additionally, the Ag-Co and Ag-Fe system have also demonstrated reduced degradation rate of plasmonic signals due to oxidation of silver thus leading to very stable plasmonic behavior over long periods of time [13, 23]. Fe_2O_3-Au core shell nanoparticles have been reported to have a high Faraday rotation at resonant frequency ascribed to spectral overlap of magneto-optical transition to plasmonic resonance [62].

5.2 Methods

5.2.1 Angle-resolved nanosphere lithography

To fabricate the pyramidal metallic nanostructures from the nanosphere lithography, the polystyrene beads of diameter 500 nm were used to mask the quartz substrates by the technique used by Prasad et. al [13]. The partial overlapping in nanopyramids was achieved by tilting the masked substrates on the sample holder away to the metallic vapor direction. To achieve 90 % overlapped in between Fe and Ag sample holder was tilted away by 1° to vapor direction, while to achieve 30 %, the sample holder was tilted away by 5°.

5.2.2 EELS fit

In order to quantify the plasmon peak position and peak area- Gaussian peaks and Lorentzian peaks were fit to the data. A multiplication of the Lorentzian functions was used to approximate the zero loss peak. A fit of zero loss peak is shown in Figure 5.1.

The summation of gaussian peaks were used to produce noise free models of the electron energy-loss spectra. Inelastic scattering in ppm (parts per million) was calculated using the

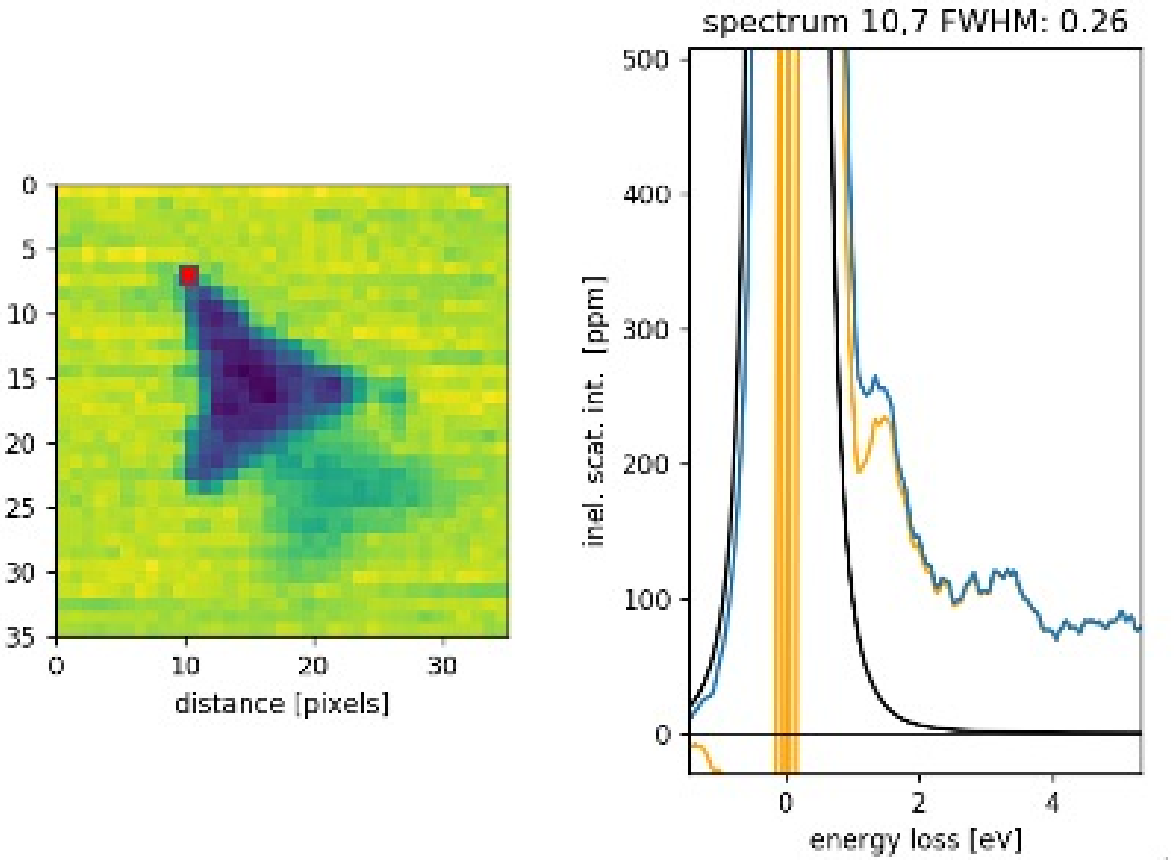

Figure 5.1: Fit spectra of zero-loss spectrum peak (black solid line) taken from red box.

relation: $\frac{I \times 10^6}{I_0}$ Where I is the beam current in a pixel from the spectrum and I_0 is the incident beam current. The Gaussian peak corresponding to the dipole plasmon peak position was used to analyze the area and peak intensity (in ppm) of plasmon loss for corresponding position (A, B and C). A representative of fit data is shown in Figure 5.2.

5.3 Results

5.3.1 Nonlinear optical properties

We studied nonlinear optical properties of nanopyramidal systems viz. pure Ag, pure Fe and Fe-Ag (with 30% and 90% overlap) at 1550 nm whose surface plasmons induced resonant absorption was at 750 nm (except for pure Fe pyramidal system). The third order optical nonlinearities were studied by f-scan methods, particularly transmission f-scan and reflection f-scan, which are modifications of the conventional z-scan method [182, 183, 184]. These methods allow us to measure the nonlinear index of refraction (n_2) in reflection and the nonlinear absorption or two photon absorption coefficient (β) in transmission modes. The electric field ($\mathbf{E}$) dependent polarization ($\mathbf{P}$) of a nonlinear system can be expressed as

$$\mathbf{P} = \chi_E^{(1)}\mathbf{E} + \mathbf{P_{NL}} = \chi_E^{(1)}\mathbf{E} + \chi_{EE}^{(2)}\mathbf{EE} + \chi_{EEE}^{(3)}\mathbf{EEE} + \chi_{EEEE}^{(4)}\mathbf{EEEE} + ... \qquad (5.1)$$

where, $\chi^{(i)}(i$=1,2,3...) is the i^{th} order nonlinear susceptibility of the nonlinear system. The real part of the $\chi_{EEE}^{(3)}$ is related to n_2 while imaginary part is related to β. Figure 5.3(a) and (b) show results for transmission and reflection f-scans for the pure Fe, pure Ag and Fe-Ag nanopyramidal systems. Two immediate features are evident from Figure 5.3(a) and (b). First, the Fe-Ag system exhibited significantly enhanced nonlinear absorption and refraction as compared to the pure Ag, which in turn was much higher than pure Fe. Second, the Fe-Ag system showed the opposite sign for the nonlinear refraction as compared to pure Ag. A large value for the nonlinear refraction of n_2^{Fe-Ag} = -2.32 cm^2/GW and nonlinear absorption coefficient of β^{Fe-Ag} = 6.5×10^3 cm/GW were obtained for the Fe-Ag system with 30 % overlap. For the Fe-Ag system with 90 % overlap, n_2^{Fe-Ag} = -1.02 cm^2/GW and β^{Fe-Ag} = 9.5×10^{3}cm/GW were obtained. Whereas, for the pure Ag system, the nonlinear refraction

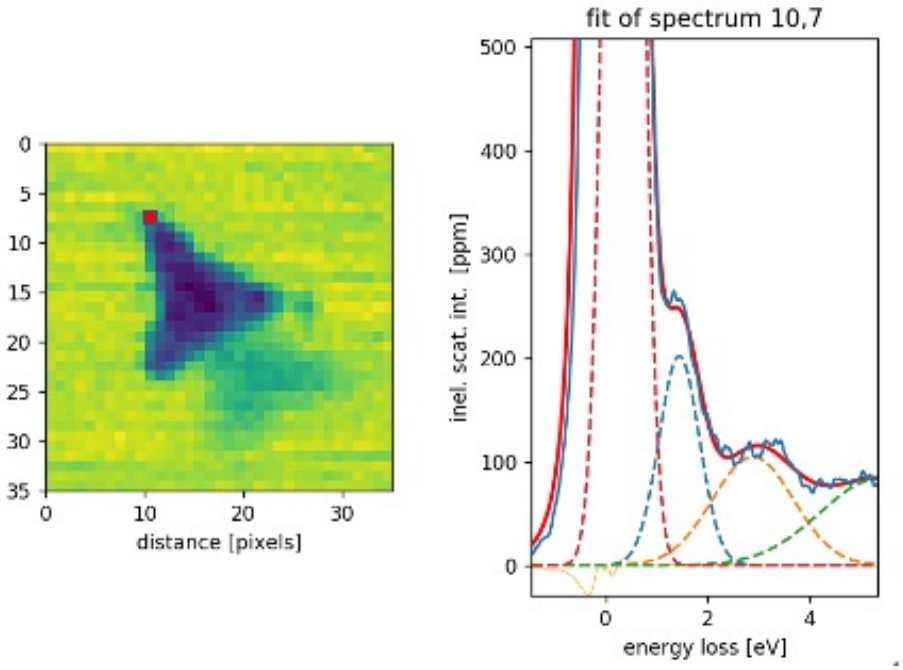

Figure 5.2: A representative of fitting of plasmon-loss peak for the spectrum data taken from the red box

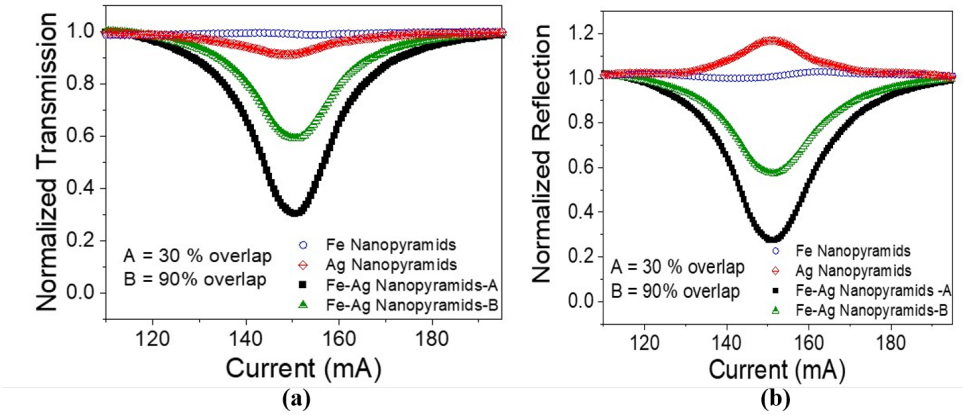

Figure 5.3: (a)normalized transmission and (b) normalized reflection of Fe, Ag and Fe-Ag nanopyramidal arrays

of n_2^{Ag} = 0.19 cm^2/GW and nonlinear absorption coefficient of β^{Ag} = 6.7×10^2 cm/GW were obtained. For the pure Fe system the nonlinear response was negligible. The n_2^{Fe-Ag} value is 3 to 4 orders of magnitude larger than those typically reported in the literature for metallic nanostructures, which range in the order of 10^{-4} cm^2/GW to 10^{-1}cm^2/GW [83, 108, 109, 110].

5.3.2 Plasmonics and microstructure

In order to understand the origin of large optical nonlinearity observed in the Fe-Ag nanopyramidal system, we investigated the plasmon induced linear optical behavior and electron energy-loss behavior. The plasmon induced linear optical absorption properties of the nanopyramidal system [pure Ag, pure Fe, Fe-Ag (30 % and 90 % overlap)] were measured using normally incident broadband light. We saw that the pure Ag has a sharper dipole resonance curve followed by Fe-Ag (∼30 % overlap) and Fe-Ag (∼90 % overlap) at 750 nm (near the energy of two photons at 1550 nm) as shown in Figure 5.4(a). The dipole resonance peaks at 750 nm were achieved in each pyramidal system by controlling the thickness of the Ag pyramids which was ∼17 nm while the height of the Fe pyramids in each case was ∼9 nm. The representative SEM image of pure Ag and 30 % overlapped Fe-Ag nanopyramidal system is shown in Figure 5.4(b) and (c). The pure Fe nanopyramidal system didn't show any significant absorption features in the wavelength region studied here. Moreover, we didn't see any linear absorption feature in the 1550 nm in all nanopyramidal systems as evident from the inset of Figure 5.4(a). The enhancement in optical nonlinearity observed in the pure Ag or the Fe-Ag system compared to that of the pure Fe system was attributed to matching of the two photon resonance conditions. The plasmonic systems (Ag and Fe-Ag) had plasmon induced resonance peak wavelengths at 750 nm which is near the fundamental frequency for two photons at 1550 nm. However, the large enhancement in the Fe-Ag system over the Ag system was completely unexpected since the plasmon induced dipole resonance is more damped in the Fe-Ag system compared to the Ag system, as evident from Figure 5.4(a). Nevertheless, this analysis firmly established that the matching of two photon resonance conditions partially contributed to the observed optical nonlinearity, as

pure Ag, and Fe-Ag nanopyramidal system had significantly higher optical nonlinearity than pure Fe.

One of the reasons for the large nonlinear optical responses from Fe-Ag nanopyramidal array could be a synergistic effect between Fe metal and Ag metal nanopyramids. To explore the system further, we investigated the electron energy-loss spectra from those nanostructures as shown in Figure 5.5(a), (b) an (c). The dipole induced electron energy-loss peaks were observed at 1.60 ± 0.02 eV in each case, slightly shifted from the observed optical absorbance at 1.65 ± 0.01 eV (750 nm). This difference in observed electron energy-loss and optical absorbance peak comes from their observed part of the dielectric function. In case of EELS, we observe $\mathrm{Im}(\frac{\epsilon-1}{\epsilon+1})$, while in optical absorption we observe $\mathrm{Im}(\epsilon)$, ϵ being the complex dielectric function of the system [32]. To analyze the energy-loss behavior from the corner of Ag nanopyramids, the features in electron energy-loss peak from Ag corners [marked as A, B, C in Figure 5.5] of each Ag, Fe-Ag (30 % overlap) and Fe-Ag (90 % overlap) were quantified in terms of peak intensity and area [in parts per million (ppm)]. We found that the peak intensity of pure Ag nanopyramids were higher than that of Fe-Ag, and the Fe-Ag (30 % overlap) had higher peak intensity than Fe-Ag (90 % overlap). Further, peak intensity and peak area of Ag corners (B and C) adjacent to the Fe overlap were smaller than free corner (A). Moreover, 30 % overlapped Fe-Ag nanopyramids had significantly larger intensity and area (at B and C corners) than 90 % overlapped Fe-Ag nanopyramids as summarized in Table 5.1.

What was apparent from the optical and EELS analysis of nanopyramidal system was that the surface plasmon dipoles are stronger for the 30 % overlapped as compared to the 90 % overlapped case. The plasmon induced oscillating dipole causes an induced electric displacement field across the Fe as in Figure 5.5(d). The magnitude of displacement field is proportional to the plasmonic dipole strength. The displacement field developed across the ferromagnetic medium could control the magnetization of ferromagnetic material through magneto-electric effect. In other words, the dipole induced local electric field act on the electrons of the ferromagnetic material which produces magneto-electric (M-E) effect with moment $\mathbf{T} \sim \mathbf{P} \times \mathbf{M}$, where $\mathbf{P}$ and $\mathbf{M}$ are plasmon dipole induced electric polarization and magnetization of ferro-electrons in Fe nanopyramids. This moment is expected to control

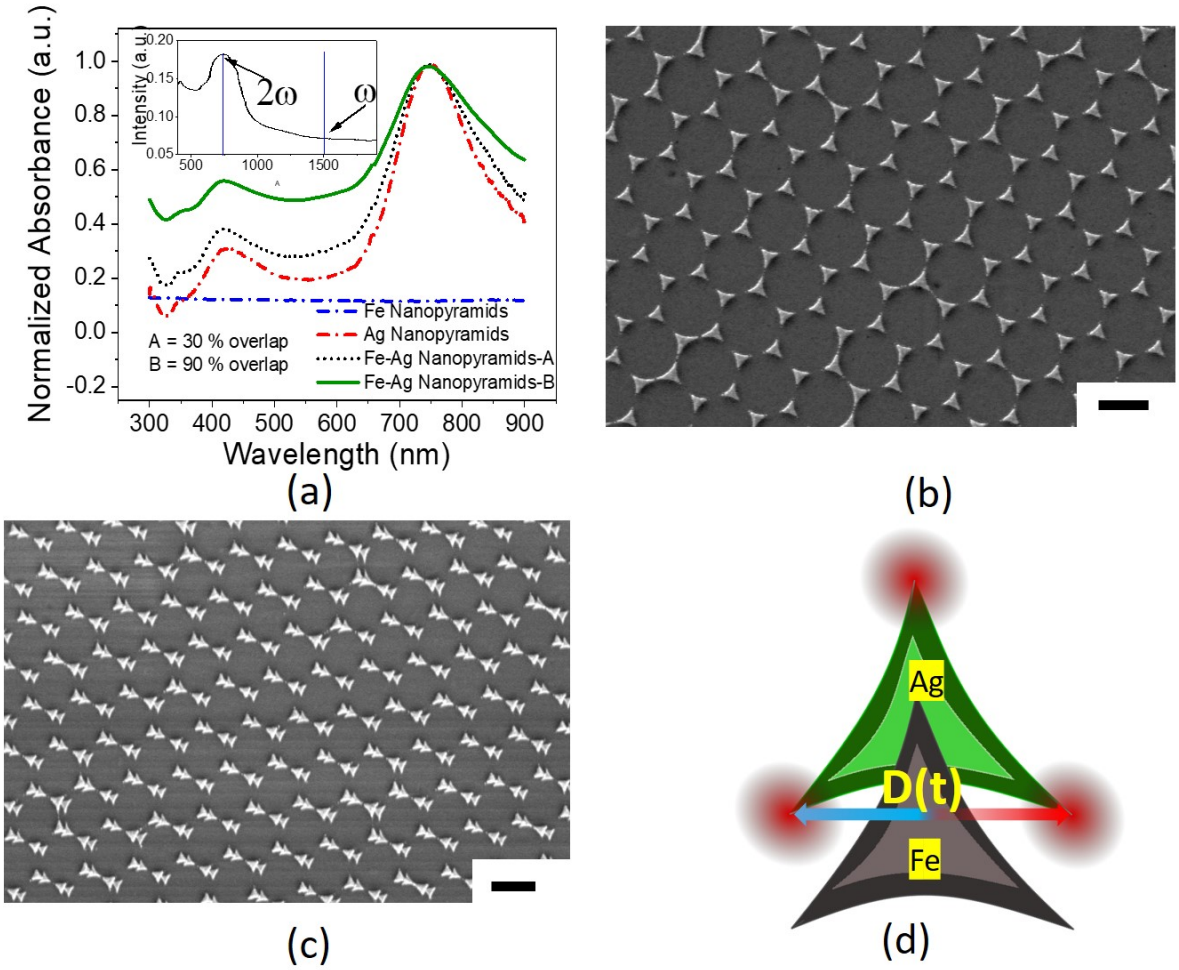

Figure 5.4: (a) Normalized plasmon induced linear absorption spectra of Fe, Ag and Fe-Ag (30 % and 90 % overlap) nanopyramidal systems. Inset shows the linear absorption of the Fe-Ag system from 400 to 2000 nm. (b) A representative scanning electron micrograph (SEM) image of pure Ag and (c) Fe-Ag (30 % overlapped system) (the scale bar is 500 nm) (d)The schematic of oscillating displacement field D(t) in the Fe pyramid induced by surface plasmon dipoles of a Ag nanopyramid

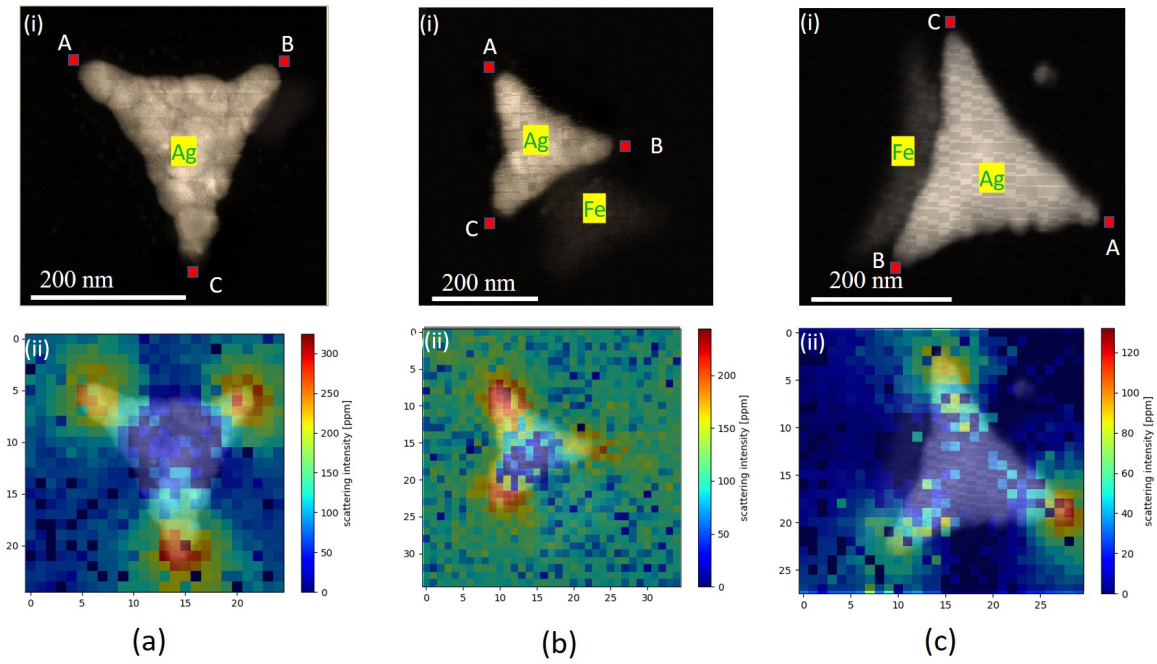

Figure 5.5: (i) Z-contrast imaging and (ii) EELS intensities of (a) pure Ag, (b) Fe-Ag (30 % overlapped), (c) Fe-Ag (90 % overlapped) nano pyramids at peak intensity of 1.60 ± 0.02 eV.

Table 5.1: The measurement average EELS peak intensity and average EELS peak area from Ag and Fe-Ag nanopyramids as marked regions A, B, C in Figure 5.5 (ppm stands for part per million)

Peak at 1.60 eV	Pure Ag			Fe-Ag (30 % overlap)			Fe-Ag (90 % overlap)		
	A	B	C	A	B	C	A	B	C
Peak intensity (ppm)	232.2	235.5	240.0	180.2	165.4	168.2	120.2	86.9	90.5
Area (ppm)	95.6	97.8	102.7	181.9	166.6	169.1	74.7	66.5	67.0

the third order optical nonlinearity in nanomaterials [185, 186]. So, the plasmon induced effect in ferromagnetic material like M-E effect could be an important factor, apart from matching of the two photon resonance conditions, for enhancement of the nonlinear optical behavior in Fe-Ag nanopyramidal system.

5.3.3 Nonlinear Faraday rotation

Given the above hypothesis, we explored the possibility of magnetic effects on the nonlinear behavior of this system by employing both the f-scan and polarization rotation measurements simultaneously, as suggested by Frey et al [142]. The Fe-Ag system, which showed large values of n_2 and β (i.e. 30 % overlap Fe-Ag), the nonlinear Faraday rotation at 1550 nm was studied. In the presence of external static magnetic field, the polarization of the system can be expressed as

$$\mathbf{P} = \chi_E^{(1)}\mathbf{E} + \mathbf{P}_{\mathbf{NL}}^{H} = \chi_E^{(1)}\mathbf{E} + \chi_{EH}^{(2)}\mathbf{EH} + \chi_{EEE}^{(3)}\mathbf{EEE} + \chi_{EEEH}^{(4)}\mathbf{EEEH} + ... \tag{5.2}$$

Here, $\chi_{EH}^{(2)}$ is the second-order nonlinear susceptibility which is related to linear Faraday rotation/magnetic circular dichroism (MCD) while $\chi_{EEEH}^{(4)}$ is the fourth-order nonlinear susceptibility which describes nonlinear Faraday (polarization) rotation. Figure 5.6(a) (in inset) and (b) are the experimental transmittance at 0.5 T and photo-induced (nonlinear) Faraday rotation at different intensities along with fitted data using equations (9) and (10) respectively. For fit, first, we calculated the third-order nonlinear susceptibility in terms of the two photon absorption coefficient (β) which was obtained to be $\chi_i^3 = \beta\frac{n^2c\lambda}{8\pi^3} = 9.4 \times 10^{-8}$ esu. Then, χ_i^4 was obtained by fitting equation Eq. 2.18 at 0.5 T. We found the value for the nonlinear fourth order susceptibility to be $\chi_i^4 = 6.5 \times 10^{-12}$ esu. The value obtained for χ_i^4 is 6 orders of magnitude larger than in dilute semiconductors [96].

5.4 Discussion

The nonlinear optical processes in metallic nanostructures are generally governed by various excitations like multiphoton absorption, thermal scattering, interband and intraband

transitions and geometry [187, 188, 189] . In our experiment, we ruled out the possibility of thermal scattering, by using a very low energy pulse of 0.4 nJ/pulse, with an average power of 20 mW on the sample, along with a repetition rate of 50 MHz, which put the system in a relatively low intensity regimen. Also the excitation wavelength of 1550 nm was far away from the plasmon resonance and therefore, low linear absorption and consequently low heating of the nanostructures is expected. Additionally, the enhancement of two photon absorption (by four times) of Fe-Ag nanoparticles over that of pure Ag nanoparticles in off-resonant wavelength was attributed to the interband and intraband transition of Fe-metals which subsequently reduced the absorption saturation effect of Fe-Ag system over pure Ag [190]. Surprisingly, we observed that the Fe-Ag nanopyramidal system has an enhancement of about 10 times that of the Ag system at lower photon energy (1550 nm). Another important observation of the optical nonlinearity of the Fe-Ag system over pure Ag was negative value of n_2 which indicates the Fe-Ag system is self-defocusing while the pure Ag system is self-focusing. This is likely due to the difference in local optical response/polarization of Fe and Ag nanopyramids with incident laser fields as discussed above. Of particular interest was the same Fe-Ag system with the large value of nonlinear (photo-induced) Faraday rotation and nonlinear magneto-optical susceptibility at the same wavelength. While the EELS results strongly suggest a contribution from plasmon induced activity in the origin of the giant nonlinear properties of this metallic system, other mechanisms may still be important. For instance, one can expect the enhancement in the optical nonlinearity of the Fe-Ag system due to evanescent wave intensification at the magnetic/nonmagnetic interface through Schoch effect (magnetoelastic origin) and/or Goos-Hänchen effect (electromagnetic origin) [191, 192]. The observation of large optical nonlinearity and strong nonlinear (photo-induced) polarization rotation effect on this system at the same wavelength of 1550 nm is very unique and clearly suggests an exciting system for further exploration.

5.5 Acknowledgment

The authors want to acknowledge support by NSF Grant ECCS-1607874. HG acknowledge financial support from SIUE. GD acknowledge support by U.S. Department of Energy, Office of Science, Basic Energy Sciences, Materials Sciences and Engineering Division.

Supplementary Material

5.5.1 Nonlinear optical properties

Fig. 5.7 presents the comparison of localized surface plasmon resonances (LSPR) and nonlinear optical properties for Ag nanopyramids at off-resonant conditions. First, LSPR at ∼750 nm and ∼710 nm respectively were achieved by controlling the height of Ag nanopyramidal arrays which were ∼17 nm and ∼25 nm respectively. The plasmon induced linear absorption spectra are as shown in Fig. 5.7(a). From Fig. 5.7(b) and (c) which are the transmission f-scan and reflection f-scan at 1550 nm respectively, it is clear that matching of two photons resonance condition affects both the nonlinear transmission and reflection. In conclusion, matching of two-photon resonances condition enhance the third order nonlinear refraction (n_2) and two-photon absorption coefficient (β).

5.5.2 Linear optical properties of Fe and Co nanopyramidal arrays

The transmission spectra of pure Fe and pure Co nanopyramidal arrays of similar structures and heights (∼9 nm). are presented in Fig. 5.8. However some researches has claimed the modified optical spectra in Co attributed to hexagonal arrays due to triangular tips or lattice structures, our results clearly suggest that the optical spectra on such structure at visible region is clearly material dependent [193]. Iron doesn't show any absorbance features in visible region.

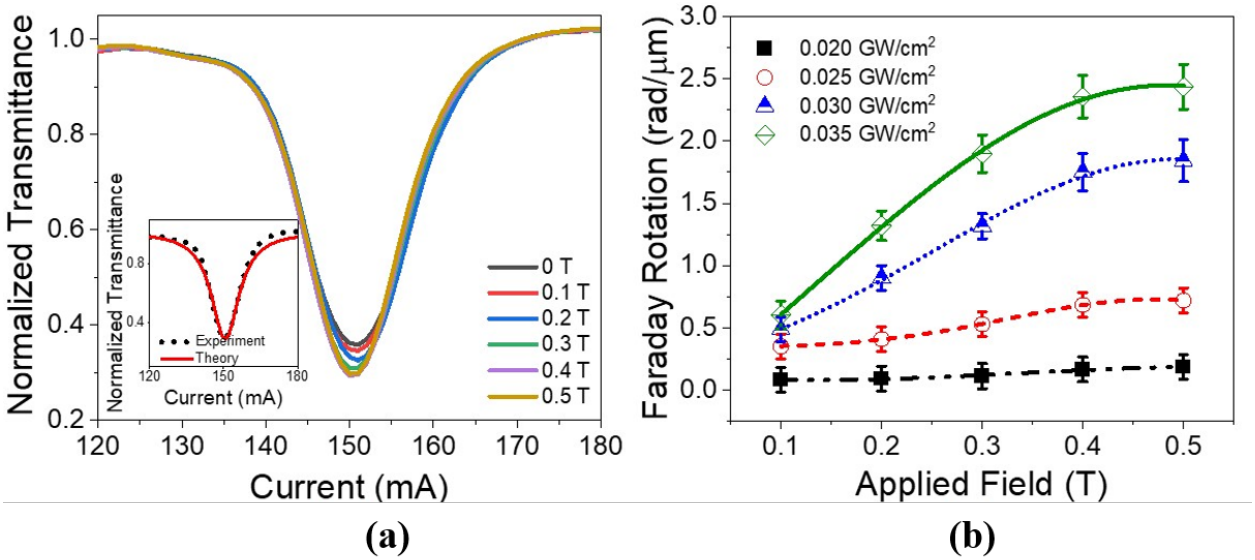

Figure 5.6: (a)Normalized transmission at different B-field, inset shows the normalized transmittance for 0.5 T and the thoretical fitting using Eq. 2.18 and the experimental value found for $\chi_i^{(3)}$ (b) Normalized polarization rotation with respect to magnetic field at different laser intensities. The solid and dotted lines are fitted curves for Faraday rotation using Eq. 2.18 and Eq. 2.15

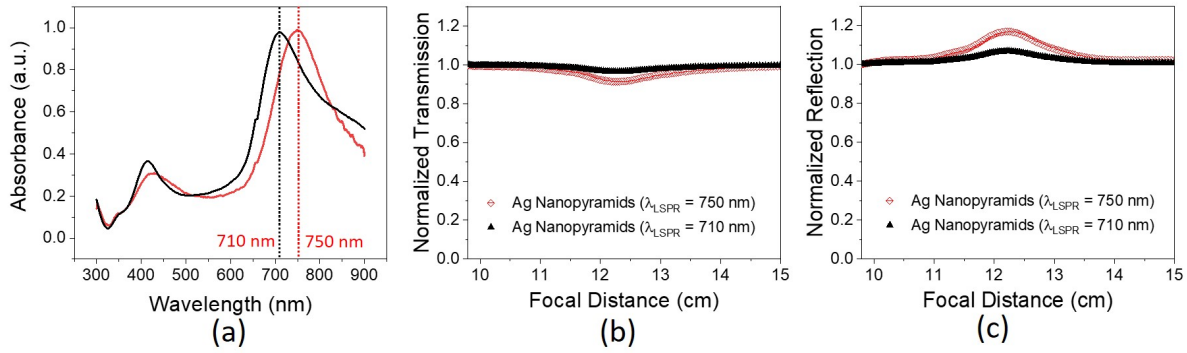

Figure 5.7: (a) Normalized plasmon induced linear absorption spectra of Ag nanopyramidal arrays with height $\sim$ 17 nm (resonance at $\sim$750 nm) and $\sim$ 25 nm (resonance at $\sim$710 nm) (b) normalized transmission f-scan and (c) normalized reflection f-scan of Ag arrays with dipole induced plasmon resonance at $\sim$750 nm and $\sim$710 nm.

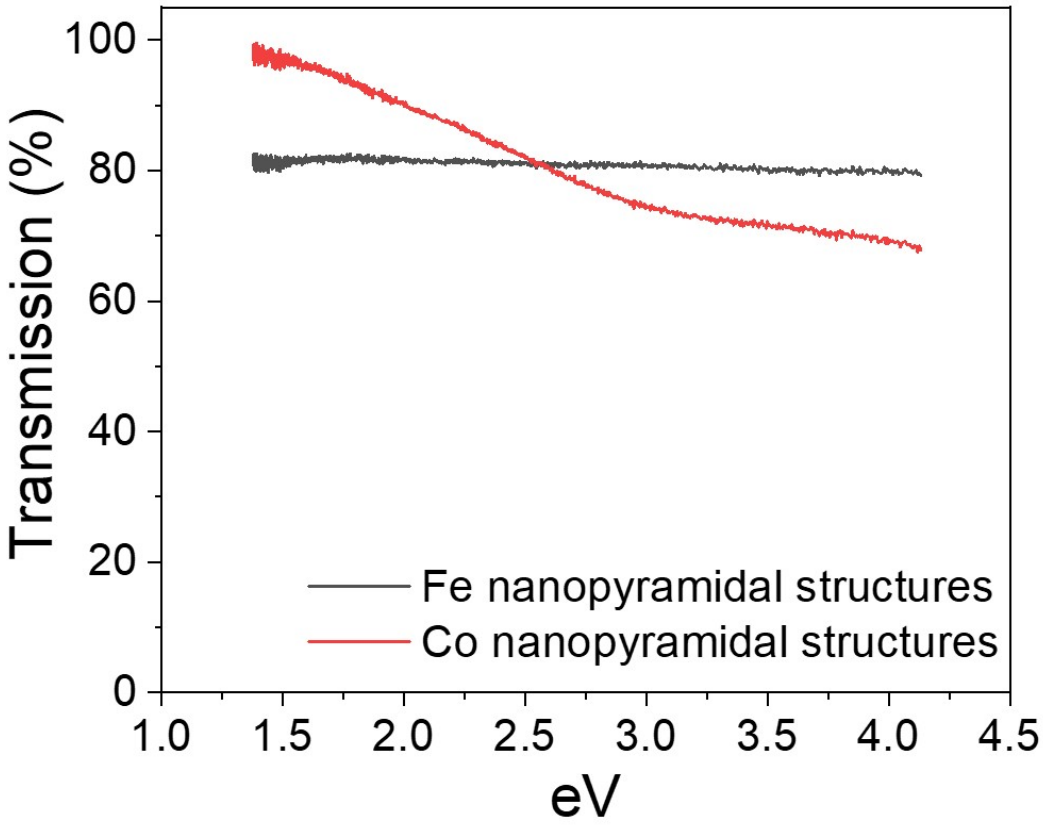

Figure 5.8: (a) Transmission spectra of Fe and Co nanopyramidal arrays of similar structures and heights.

5.5.3 EELS study of Fe-Ag nanopyramids

The EELS study shows absence of any plasmon loss from Fe nanopyramids. The EELS measurement shows only the damping of dipolar resonance at adjacent corners of Ag (∼1.6 eV) (presented on table in main manuscript) and hexapolar plasmon resonance at the side of Ag (∼2.5 eV) which is overlapped with Fe nanopyramid as in Fig 5.10(b) [side F]. We didn't see any unusual plasmon-loss features in Fe as well as Ag nanopyramids.

5.5.4 Detecting the oxidation state of Fe in Fe nanopyramidal arrays

The EELS measurement near the Fe -L and O-K energy in Fe nanopyramid clearly shows that the Fe is in pure Fe state (no oxide formation). This is evident from O-K feature in EELS spectra measured in Fe nanopyramid and expected at 532 eV is absent as shown in Fig .5.10. This confirms the no dielectric layer formation in our experiment.

5.5.5 Faraday rotation

The raw data for nonlinear Faraday rotation measurement is presented in Fig. 5.11.

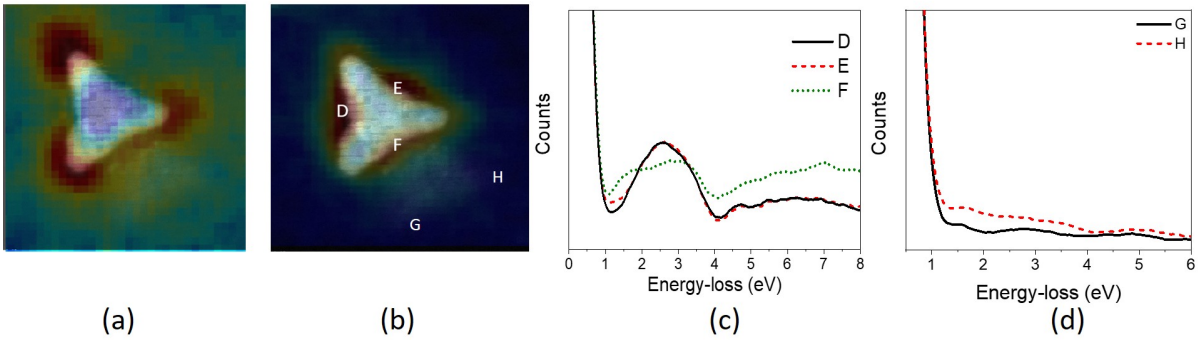

Figure 5.9: (a) EELS intensity map at 1.6 eV with adjacent averaging, B) EELS intensity map at 2.5 eV with adjacent averaging (c) the EELS intensity at hexpolar corner D, E and F (d) the EELS intensity measured form G and H (Fe pyramidal corners)

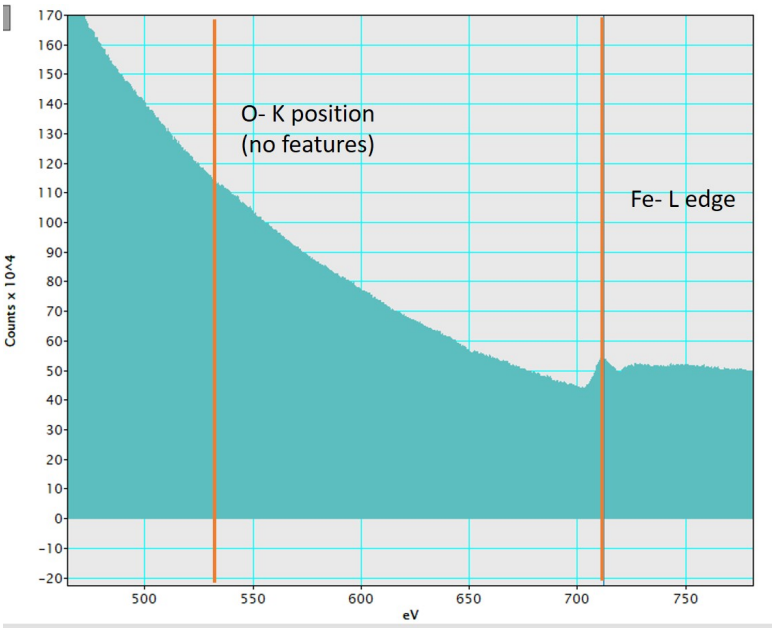

Figure 5.10: (a) EELS of Fe-L and O-K edges in Fe nanopyramid

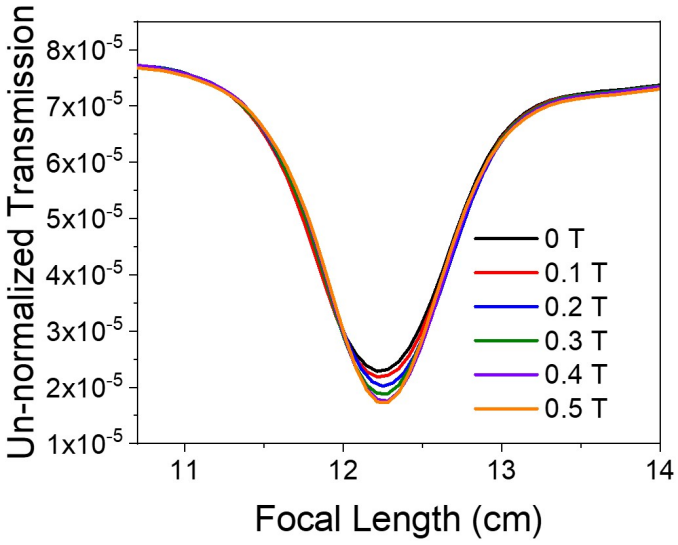

Figure 5.11: Un-normalized transmission with respect to magnetic field in Faraday rotation set-up

Chapter 6

Summary and future work

A summary of the primary outcomes of this dissertation work are described below.

6.1 Summary

Detection of localized interface plasmons

We studied the surface and interface plasmons of bimetallic Co-Ag nanoparticles with epitaxial interface at high energy and spatial resolution by STEM-EELS. We found the emergence of an additional localized electron energy-loss peak originated only at or near the metal-metal interface regions from the Co-Ag nanoparticle. This energy-loss peak with Eigen mode in between in-plane dipole and QP plasmon mode confirms the novelty of the origin. Furthers, we observed a progressive weakening of the energy-loss peak as the monochromatic electron beam traversed away from the triple point either in Ag or in Co sides, further confirming that the energy-loss behavior should be a function of the interface. The peak was more localized than in-plane dipole when excited by fast electrons beam and we attribute it to be due to modified plasma oscillations owing to effective mass and charge density in the interface region. The peak was not distinctly observable from the ensemble of such bimetallic particles by normally incident light. The most likely reason is due to the out-of-plane nature of the interface charge oscillation.

Switchable surface plasmons from resettable contact angle in plasmonic nanostructures

We have investigated the potential to reversibly and repeatedly switch plasmonic properties based on nanosecond laser pulse tuning of the contact angle of Ag nanoparticles synthesize on quartz substrates. The contact angle of the nanoparticles could be reversibly changed between near-spherical and near-hemispherical shapes under a single nanosecond laser pulse by heating either in a glycerol ambient (which produced the near-spherical shape) or in air (which produces the near-hemispherical shape). This contact angle changing resulted in a reversible shift of the dipolar resonance of 38.5 $\pm$ 1.6 nm with an accompanying change in intensity consistent with a shape effect that could be explained by the dynamic Maxwell-Garnet effective medium model. Over multiple cycles in each set/reset and switched state, a small but systematic shift in the plasmon wavelength as well as decrease in overall intensity was observed and attributed to a loss of material due to the laser melting process. Overall, this study establishes that one could switch and reset the desired modes of the LSPR in plasmonically active metallic nanoparticles within nanosecond time scales in plasmonically passive substrates.

Nonlinear optical and magneto-optical behavior of bimetallic plasmonic structures in telecommunication wavelength

We investigated the nonlinear optical and magneto-optical properties of bi-metallic nanopyramidal systems in telecommunication wavelength. We found that the large value of nonlinear optical and magneto-optical coefficients are due to two photon absorption phenomena which is further enhanced due to plasmon induced synergistic effect between two metallic systems. We further found that the partially overlapped Fe-Ag system exhibits a negative and large value of third order refractive index, two photon absorption coefficient and nonlinear Faraday rotation unlike pure Ag or Fe nanopyramidal system. Moreover, the nonlinear responses in Fe-Ag systems are strongly dependent on the overlapping extent and in turn the plasmon induced dipole strength across the ferromagnetic material. This strongly indicates the enhancement of third order nonlinearity in Fe-Ag nanopyramidal systems due to the plasmon

induced activity in Fe metals like magneto-electric effect which depends on the plasmon induced polarization and magnetization of ferromagnetic material.

6.2 Future work

Detection of localized interface plasmons

The localized interface plasmon behavior with different size and different metallic systems can be studied. Further, a comprehensive understanding of interface plasmonic can be developed by considering interface bonding, effective mass and electron charge at interfaces of metals, semiconductors or dielectrics.

Switchable surface plasmons from resettable contact angle in plasmonic nanostructures

The resettable contact angle behavior due to laser heating of plasmonic nanostructures in different fluids like in water or engine oil can be explored. This behavior allows selective absorption of optical spectra. Also, the tuning mechanism analysis from different shape of the nanoparticles can also be studied. Plasmon induced optical transmission spectra and switching mechanism starting from hexagonal nanopyramidal arrays in air and water medium are shown in Figure 6.1.

Nonlinear optical and magneto-optical behavior of bimetallic plasmonic structures in telecommunication wavelength

A systematic study in of bimetallic nanopyramids with respect to overlap and nonlinear responses can be performed to optimize the behavior. Also such responses from other material system can be explored.

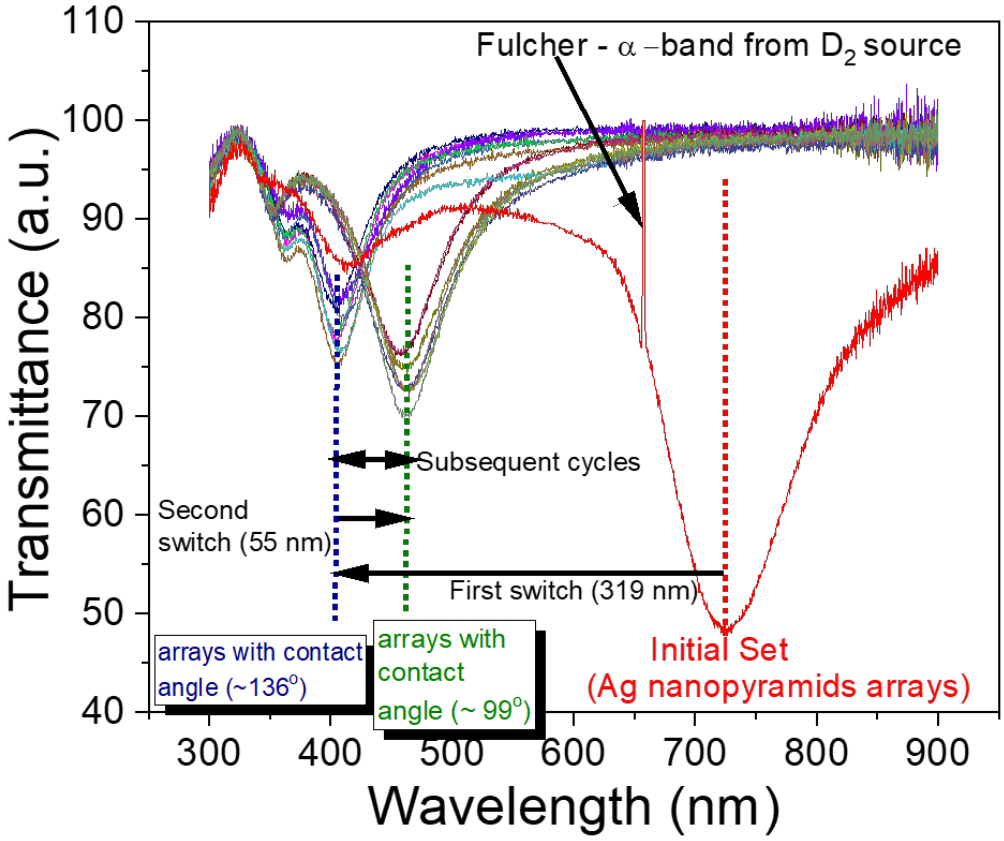

Figure 6.1: Plasmon induced optical transmission spectra and tunability for hexagonal arrays

Bibliography

[1] Jingxuan Ge. Excitations of quasi-particles in nanostructured systems. 2017. xi, xv, 51, 59, 60

[2] Jamie M Fitzgerald, Prineha Narang, Richard V Craster, Stefan A Maier, and Vincenzo Giannini. Quantum plasmonics. *Proceedings of the IEEE*, 104(12):2307–2322, 2016. xii, 3, 4

[3] Feng Wang and Y Ron Shen. General properties of local plasmons in metal nanostructures. *Physical review letters*, 97(20):206806, 2006. xii, 8

[4] Jeffrey N Anker, W Paige Hall, Olga Lyandres, Nilam C Shah, Jing Zhao, and Richard P Van Duyne. Biosensing with plasmonic nanosensors. In *Nanoscience And Technology: A Collection of Reviews from Nature Journals*, pages 308–319. World Scientific, 2010. xii, 9, 28, 64

[5] Xianmao Lu, Matthew Rycenga, Sara E Skrabalak, Benjamin Wiley, and Younan Xia. Chemical synthesis of novel plasmonic nanoparticles. *Annual review of physical chemistry*, 60:167–192, 2009. xii, 10

[6] Benjamin J Wiley, Sang Hyuk Im, Zhi-Yuan Li, Joeseph McLellan, Andrew Siekkinen, and Younan Xia. Maneuvering the surface plasmon resonance of silver nanostructures through shape-controlled synthesis, 2006. xii, 10

[7] Benjamin J Wiley, Yeechi Chen, Joseph M McLellan, Yujie Xiong, Zhi-Yuan Li, David Ginger, and Younan Xia. Synthesis and optical properties of silver nanobars and nanorice. *Nano letters*, 7(4):1032–1036, 2007. xii, 10

[8] Zhihong Nie, Alla Petukhova, and Eugenia Kumacheva. Properties and emerging applications of self-assembled structures made from inorganic nanoparticles. *Nature nanotechnology*, 5(1):15–25, 2010. xii, 24, 25

[9] Zhihong Nie, Daniele Fava, Eugenia Kumacheva, Shan Zou, Gilbert C Walker, and Michael Rubinstein. Self-assembly of metal–polymer analogues of amphiphilic triblock copolymers. *Nature materials*, 6(8):609–614, 2007. xii, 25

[10] H Krishna, N Shirato, C Favazza, and R Kalyanaraman. Energy driven self-organization in nanoscale metallic liquid films. *Physical Chemistry Chemical Physics*, 11(37):8136–8143, 2009. xiii, 25

[11] A De Ninno, A Gerardino, B Girarda, G Grenci, and L Businaro. Top-down approach to nanotechnology for cell-on-chip applications. *Biophysics and Bioengineering Letters*, 3(2), 2010. xiii, 26

[12] Katherine A Willets and Richard P Van Duyne. Localized surface plasmon resonance spectroscopy and sensing. *Annu. Rev. Phys. Chem.*, 58:267–297, 2007. xiii, 5, 34

[13] Venkatanarayana P Sandireddy, Krishna P Koirala, Humaira Taz, and Ramki Kalyanaraman. Thermal and plasmonic stabilization of silver nanostructures using a bilayer anchoring technique. *ACS applied materials & interfaces*, 10(39):33630–33639, 2018. xiii, 5, 36, 37, 64, 82

[14] Abhinav Malasi, Jingxuan Ge, Connor Carr, Hernando Garcia, Gerd Duscher, and Ramki Kalyanaraman. Two-dimensionally ordered plasmonic and magnetic nanostructures on transferable electron-transparent substrates. *Particle & Particle Systems Characterization*, 32(10):970–978, 2015. xiii, 36, 38, 53

[15] Peter B Johnson and R-WJPrB Christy. Optical constants of the noble metals. *Physical review B*, 6(12):4370, 1972. xvi, 74, 77

[16] Stanislav B Glybovski, Sergei A Tretyakov, Pavel A Belov, Yuri S Kivshar, and Constantin R Simovski. Metasurfaces: From microwaves to visible. *Physics reports*, 634:1–72, 2016. 1

[17] Xiaoyang Duan, Simon Kamin, and Na Liu. Dynamic plasmonic colour display. *Nature communications*, 8(1):1–9, 2017. 1

[18] Wenjiang Fan, Benjamin J Lawrie, and Raphael C Pooser. Quantum plasmonic sensing. *Physical Review A*, 92(5):053812, 2015. 1

[19] Mark S Tame, KR McEnery, ŞK Özdemir, Jinhyoung Lee, Stefan A Maier, and MS Kim. Quantum plasmonics. *Nature Physics*, 9(6):329–340, 2013. 1

[20] Jung-Hwan Song, Søren Raza, Jorik van de Groep, Ju-Hyung Kang, Qitong Li, Pieter G Kik, and Mark L Brongersma. Nanoelectromechanical modulation of a strongly-coupled plasmonic dimer. *Nature Communications*, 12(1):1–7, 2021. 1

[21] Xiaoguang Li, Ao Teng, Mustafa M Özer, Jian Shen, Hanno H Weitering, and Zhenyu Zhang. Plasmonic excitations in ultrathin metal films on dielectric substrates. *New Journal of Physics*, 16(6):065014, 2014. 1

[22] Ritesh Sachan, S Yadavali, N Shirato, H Krishna, V Ramos, Gerd Duscher, Stephen J Pennycook, AK Gangopadhyay, H Garcia, and R Kalyanaraman. Self-organized bimetallic ag–co nanoparticles with tunable localized surface plasmons showing high environmental stability and sensitivity. *Nanotechnology*, 23(27):275604, 2012. 2, 28, 82

[23] Ritesh Sachan, Abhinav Malasi, Jingxuan Ge, Sagar Yadavali, Hare Krishna, Anup Gangopadhyay, Hernando Garcia, Gerd Duscher, and Ramki Kalyanaraman. Ferroplasmons: Intense localized surface plasmons in metal-ferromagnetic nanoparticles. *ACS nano*, 8(10):9790–9798, 2014. 2, 28, 31, 52, 82

[24] Martti Kauranen and Anatoly V Zayats. Nonlinear plasmonics. *Nature photonics*, 6(11):737–748, 2012. 2, 11

[25] Ian Freestone, Nigel Meeks, Margaret Sax, and Catherine Higgitt. The lycurgus cup—a roman nanotechnology. *Gold bulletin*, 40(4):270–277, 2007. 2

[26] Michael Faraday. On the relations of gold and other metals to light. *Proceedings of the Royal Society of London*, (8):356–361, 1857. 2

[27] Gustav Mie. Beiträge zur optik trüber medien, speziell kolloidaler metallösungen. *Annalen der physik*, 330(3):377–445, 1908. 2, 5

[28] Stefan Alexander Maier. *Plasmonics: fundamentals and applications*. Springer Science & Business Media, 2007. 3, 5, 64

[29] David Pines. Collective energy losses in solids. *Reviews of modern physics*, 28(3):184, 1956. 3

[30] Rufus H Ritchie. Plasma losses by fast electrons in thin films. *Physical review*, 106(5):874, 1957. 3

[31] EA Stern and RA Ferrell. Surface plasma oscillations of a degenerate electron gas. *Physical Review*, 120(1):130, 1960. 3, 28, 52

[32] Ray F Egerton. *Electron energy-loss spectroscopy in the electron microscope*. Springer Science & Business Media, 2011. 3, 6, 15, 43, 54, 55, 87

[33] L Marton and Lewis B Leder. Energy loss of electrons in passage through thin films. *Physical Review*, 94(1):203, 1954. 3

[34] Heinz Raether. Solid state excitations by electrons. In *Springer Tracts in Modern Physics, Volume 38*, pages 84–157. Springer, 1965. 3

[35] P Berini, R Charbonneau, N Lahoud, and G Mattiussi. Characterization of long-range surface-plasmon-polariton waveguides. *Journal of Applied Physics*, 98(4):043109, 2005. 3

[36] Pierre Berini and Israel De Leon. Surface plasmon–polariton amplifiers and lasers. *Nature photonics*, 6(1):16–24, 2012. 3

[37] Joseph M Luther, Prashant K Jain, Trevor Ewers, and A Paul Alivisatos. Localized surface plasmon resonances arising from free carriers in doped quantum dots. *Nature materials*, 10(5):361, 2011. 5, 64

[38] Anne-Laure Baudrion, Antoine Perron, Alessandro Veltri, Alexandre Bouhelier, Pierre-Michel Adam, and Renaud Bachelot. Reversible strong coupling in silver nanoparticle arrays using photochromic molecules. *Nano letters*, 13(1):282–286, 2013. 5

[39] Borja Sepúlveda, Paula C Angelomé, Laura M Lechuga, and Luis M Liz-Marzán. Lspr-based nanobiosensors. *nano today*, 4(3):244–251, 2009. 5, 64

[40] Burak Gerislioglu, Liangliang Dong, Arash Ahmadivand, Huatian Hu, Peter Nordlander, and Naomi J Halas. Monolithic metal dimer-on-film structure: New plasmonic properties introduced by the underlying metal. *Nano Letters*, 20(3):2087–2093, 2020. 5

[41] Haiying Xu, Caixia Kan, Changzong Miao, Changshun Wang, Jingjing Wei, Yuan Ni, Beibei Lu, and Daning Shi. Synthesis of high-purity silver nanorods with tunable plasmonic properties and sensor behavior. *Photonics Research*, 5(1):27–32, 2017. 5

[42] Julia M Bingham, Katherine A Willets, Nilam C Shah, David Q Andrews, and Richard P Van Duyne. Localized surface plasmon resonance imaging: simultaneous single nanoparticle spectroscopy and diffusional dynamics. *The Journal of Physical Chemistry C*, 113(39):16839–16842, 2009. 5

[43] Marc P Raphael, Joseph A Christodoulides, James B Delehanty, James P Long, Pehr E Pehrsson, and Jeff M Byers. Quantitative lspr imaging for biosensing with single nanostructure resolution. *Biophysical journal*, 104(1):30–36, 2013. 5

[44] Yunliang Shao, Shuping Xu, Xianliang Zheng, Ye Wang, and Weiqing Xu. Optical fiber lspr biosensor prepared by gold nanoparticle assembly on polyelectrolyte multilayer. *Sensors*, 10(4):3585–3596, 2010. 5

[45] Jiangping Chen, Se Shi, Rongxin Su, Wei Qi, Renliang Huang, Mengfan Wang, Libing Wang, and Zhimin He. Optimization and application of reflective lspr optical fiber biosensors based on silver nanoparticles. *Sensors*, 15(6):12205–12217, 2015. 5

[46] Adam D McFarland and Richard P Van Duyne. Single silver nanoparticles as real-time optical sensors with zeptomole sensitivity. *Nano letters*, 3(8):1057–1062, 2003. 5

[47] Yu-Quan Chen and Chia-Jung Lu. Surface modification on silver nanoparticles for enhancing vapor selectivity of localized surface plasmon resonance sensors. *Sensors and Actuators B: Chemical*, 135(2):492–498, 2009. 5

[48] Martin J Mulvihill, Xing Yi Ling, Joel Henzie, and Peidong Yang. Anisotropic etching of silver nanoparticles for plasmonic structures capable of single-particle sers. *Journal of the American Chemical Society*, 132(1):268–274, 2010. 5

[49] Joseph Parisi, Liang Su, and Yu Lei. In situ synthesis of silver nanoparticle decorated vertical nanowalls in a microfluidic device for ultrasensitive in-channel sers sensing. *Lab on a Chip*, 13(8):1501–1508, 2013. 5

[50] César Clavero. Plasmon-induced hot-electron generation at nanoparticle/metal-oxide interfaces for photovoltaic and photocatalytic devices. *Nature Photonics*, 8(2):95–103, 2014. 5, 52

[51] Koichi Awazu, Makoto Fujimaki, Carsten Rockstuhl, Junji Tominaga, Hirotaka Murakami, Yoshimichi Ohki, Naoya Yoshida, and Toshiya Watanabe. A plasmonic photocatalyst consisting of silver nanoparticles embedded in titanium dioxide. *Journal of the American Chemical Society*, 130(5):1676–1680, 2008. 5

[52] Darija Domazet Jurašin, Marija Ćurlin, Ivona Capjak, Tea Crnković, Marija Lovrić, Michal Babič, Daniel Horák, Ivana Vinković Vrček, and Srećko Gajović. Surface coating affects behavior of metallic nanoparticles in a biological environment. *Beilstein Journal of Nanotechnology*, 7(1):246–262, 2016. 5

[53] WL Bade. Drude-model calculation of dispersion forces. i. general theory. *The Journal of Chemical Physics*, 27(6):1280–1284, 1957. 5, 15

[54] Kathryn M Mayer and Jason H Hafner. Localized surface plasmon resonance sensors. *Chemical reviews*, 111(6):3828–3857, 2011. 6

[55] Boris Luk'yanchuk, Nikolay I Zheludev, Stefan A Maier, Naomi J Halas, Peter Nordlander, Harald Giessen, and Chong Tow Chong. The fano resonance in plasmonic nanostructures and metamaterials. *Nature materials*, 9(9):707–715, 2010. 6

[56] Jonathan A Fan, Chihhui Wu, Kui Bao, Jiming Bao, Rizia Bardhan, Naomi J Halas, Vinothan N Manoharan, Peter Nordlander, Gennady Shvets, and Federico Capasso. Self-assembled plasmonic nanoparticle clusters. *science*, 328(5982):1135–1138, 2010. 6

[57] Stephan Link and Mostafa A El-Sayed. Spectral properties and relaxation dynamics of surface plasmon electronic oscillations in gold and silver nanodots and nanorods, 1999. 7, 65

[58] NC Panoiu, WEI Sha, DY Lei, and GC Li. Nonlinear optics in plasmonic nanostructures. *Journal of Optics*, 20(8):083001, 2018. 11

[59] VK Valev, N Smisdom, AV Silhanek, B De Clercq, W Gillijns, M Ameloot, VV Moshchalkov, and Thierry Verbiest. Plasmonic ratchet wheels: switching circular dichroism by arranging chiral nanostructures. *Nano letters*, 9(11):3945–3948, 2009. 11

[60] Leonardo de S Menezes, Lúcio H Acioli, Melissa Maldonado, Jawad Naciri, Nicholas Charipar, Jake Fontana, Diego Rativa, Cid B de Araújo, and Anderson SL Gomes. Large third-order nonlinear susceptibility from a gold metasurface far off the plasmonic resonance. *JOSA B*, 36(6):1485–1491, 2019. 11

[61] Ivan S Maksymov. Magneto-plasmonic nanoantennas: basics and applications. *Reviews in Physics*, 1:36–51, 2016. 12

[62] Prashant K Jain, Yanhong Xiao, Ronald Walsworth, and Adam E Cohen. Surface plasmon resonance enhanced magneto-optics (supremo): Faraday rotation enhancement in gold-coated iron oxide nanocrystals. *Nano letters*, 9(4):1644–1650, 2009. 12, 82

[63] Lei Wang, Cesar Clavero, Zachary Huba, Kyler J Carroll, Everett E Carpenter, Diefeng Gu, and Rosa A Lukaszew. Plasmonics and enhanced magneto-optics in core- shell co-ag nanoparticles. *Nano letters*, 11(3):1237–1240, 2011. 12

[64] Francesco Pineider, Ceesar de Juliaan Fernaandez, Valeria Videtta, Elvio Carlino, Awni Al Hourani, Fabrice Wilhelm, Andrei Rogalev, P Davide Cozzoli, Paolo Ghigna, and Claudio Sangregorio. Spin-polarization transfer in colloidal magnetic-plasmonic au/iron oxide hetero-nanocrystals. *ACS nano*, 7(1):857–866, 2013. 12

[65] Wei Zheng. Nonlinear optical studies of photoelastic effect and magneto-plasmonics. 2014. 12

[66] John David Jackson. *Classical electrodynamics*. John Wiley & Sons, 2007. 13

[67] M Haddad, F Jonsson, R Frey, and C Flytzanis. Nonlinear optical gyrotropy. *NONLINEAR OPTICS-READING-*, 23(3/4):251–268, 2000. 13, 16, 20, 21

[68] Mildred Dresselhaus, Gene Dresselhaus, Stephen B Cronin, and A Gomes Souza Filho. *Solid State Properties*. Springer, 2018. 14

[69] DM Roessler. Kramers-kronig analysis of reflectance data: Iii. approximations, with reference to sodium iodide. *British Journal of Applied Physics*, 17(10):1313, 1966. 15

[70] eg PA Franken, Alan E Hill, CW el Peters, and G Weinreich. Generation of optical harmonics. *Physical Review Letters*, 7(4):118, 1961. 16

[71] Robert W Boyd. *Nonlinear optics*. Academic press, 2020. 17

[72] Chung-Lun Wu, Yung-Hsiang Lin, Sheng-Pin Su, Bo-Ji Huang, Cheng-Ting Tsai, Huai-Yung Wang, Yu-Chieh Chi, Chih-I Wu, and Gong-Ru Lin. Enhancing optical nonlinearity in a nonstoichiometric sin waveguide for cross-wavelength all-optical data processing. *Acs Photonics*, 2(8):1141–1154, 2015. 22

[73] Mansoor Sheik-Bahae, Ali A Said, David J Hagan, MJ Soileau, and Eric W Van Stryland. Nonlinear refraction and optical limiting in. *Optical engineering*, 30(8):1228–1236, 1991. 22

[74] Richard D Schaller, Justin C Johnson, Kevin R Wilson, Lynn F Lee, Louis H Haber, and Richard J Saykally. Nonlinear chemical imaging nanomicroscopy: from second and third harmonic generation to multiplex (broad-bandwidth) sum frequency generation near-field scanning optical microscopy, 2002. 22

[75] Michael Scalora, Jonathan P Dowling, Charles M Bowden, and Mark J Bloemer. Optical limiting and switching of ultrashort pulses in nonlinear photonic band gap materials. *Physical review letters*, 73(10):1368, 1994. 22

[76] T Morioka, S Kawanishi, H Takara, and M Saruwatari. Multiple-output, 100 gbit/s all-optical demultiplexer based on multichannel four-wave mixing pumped by a linearly-chirped square pulse. *Electronics Letters*, 30(23):1959–1960, 1994. 22

[77] Dirk Jalas, Nabeel Hakemi, Matteo Cherchi, Mikko Harjanne, Alexander Yu Petrov, and Manfred Eich. Faraday rotation in silicon waveguides. In *2017 IEEE 14th International Conference on Group IV Photonics (GFP)*, pages 141–142. IEEE, 2017. 22

[78] R Dekker, A Driessen, T Wahlbrink, C Moormann, J Niehusmann, and M Först. Ultrafast kerr-induced all-optical wavelength conversion in silicon waveguides using 1.55 μm femtosecond pulses. *Optics express*, 14(18):8336–8346, 2006. 22

[79] PA Andrekson, NA Olsson, JR Simpson, T Tanbun-Ek, RA Logan, and M Haner. 16 gbit/s all-optical demultiplexing using four-wave mixing. *Electronics Letters*, 27(11):922–924, 1991. 22

[80] Rafael Drampyan, Andrew D Greentree, and AV Durrant. Two field nonlinear faraday rotation in rubidium vapor in a doppler-free geometry. *Optics communications*, 276(2):251–260, 2007. 22, 23

[81] Florian Wolfgramm, Alessandro Cere, Federica A Beduini, Ana Predojević, Marco Koschorreck, and Morgan W Mitchell. Squeezed-light optical magnetometry. *Physical review letters*, 105(5):053601, 2010. 22

[82] Yi Hua, Kavita Chandra, Duncan Hieu M Dam, Gary P Wiederrecht, and Teri W Odom. Shape-dependent nonlinear optical properties of anisotropic gold nanoparticles. *The journal of physical chemistry letters*, 6(24):4904–4908, 2015. 22

[83] Kai Wang, Hua Long, Ming Fu, Guang Yang, and Peixiang Lu. Size-related third-order optical nonlinearities of au nanoparticle arrays. *Optics express*, 18(13):13874–13879, 2010. 22, 27, 86

[84] Fei Zhao, Hao-Ling Sun, Gang Su, and Song Gao. Synthesis and size-dependent magnetic properties of monodisperse eus nanocrystals. *small*, 2(2):244–248, 2006. 22

[85] M Dinu, Francesco Quochi, and H Garcia. Third-order nonlinearities in silicon at telecom wavelengths. *Applied physics letters*, 82(18):2954–2956, 2003. 22

[86] Han Zhang, Stéphane Virally, Qiaoliang Bao, Loh Kian Ping, Serge Massar, Nicolas Godbout, and Pascal Kockaert. Z-scan measurement of the nonlinear refractive index of graphene. *Optics letters*, 37(11):1856–1858, 2012. 22

[87] Xiang Qi, Yupeng Zhang, Qingdong Ou, Son Tung Ha, Cheng-Wei Qiu, Han Zhang, Yi-Bing Cheng, Qihua Xiong, and Qiaoliang Bao. Photonics and optoelectronics of 2d metal-halide perovskites. *Small*, 14(31):1800682, 2018. 22

[88] Manish Chhowalla, Zhongfan Liu, and Hua Zhang. Two-dimensional transition metal dichalcogenide (tmd) nanosheets. *Chemical Society Reviews*, 44(9):2584–2586, 2015. 22

[89] Pengfei Li, Yao Chen, Tieshan Yang, Ziyu Wang, Han Lin, Yanhua Xu, Lei Li, Haoran Mu, Bannur Nanjunda Shivananju, Yupeng Zhang, et al. Two-dimensional ch3nh3pbi3 perovskite nanosheets for ultrafast pulsed fiber lasers. *ACS applied materials & interfaces*, 9(14):12759–12765, 2017. 22

[90] Jingying Liu, Yunzhou Xue, Ziyu Wang, Zai-Quan Xu, Changxi Zheng, Bent Weber, Jingchao Song, Yusheng Wang, Yuerui Lu, Yupeng Zhang, et al. Two-dimensional ch3nh3pbi3 perovskite: Synthesis and optoelectronic application. *ACS nano*, 10(3):3536–3542, 2016. 22

[91] Renzhi Ma and Takayoshi Sasaki. Nanosheets of oxides and hydroxides: ultimate 2d charge-bearing functional crystallites. *Advanced materials*, 22(45):5082–5104, 2010. 22

[92] Khant Minn, Aleksei Anopchenko, Jingyi Yang, and Ho Wai Howard Lee. Excitation of epsilon-near-zero resonance in ultra-thin indium tin oxide shell embedded nanostructured optical fiber. *Scientific reports*, 8(1):2342, 2018. 22

[93] Kostya S Novoselov, D Jiang, F Schedin, TJ Booth, VV Khotkevich, SV Morozov, and Andre K Geim. Two-dimensional atomic crystals. *Proceedings of the National Academy of Sciences*, 102(30):10451–10453, 2005. 22

[94] Yunzhou Xue, Yupeng Zhang, Yan Liu, Hongtao Liu, Jingchao Song, Joice Sophia, Jingying Liu, Zaiquan Xu, Qingyang Xu, Ziyu Wang, et al. Scalable production of a few-layer mos2/ws2 vertical heterojunction array and its application for photodetectors. *Acs Nano*, 10(1):573–580, 2015. 22

[95] RW Cooper, WA Crossley, JL Page, and RF Pearson. Faraday rotation in yig and tbig. *Journal of Applied Physics*, 39(2):565–567, 1968. 22

[96] J Frey, R Frey, C Flytzanis, and R Triboulet. Observation of nonlinear faraday processes in cdmnte diluted magnetic semiconductors. *Optics communications*, 84(1-2):76–80, 1991. 23, 27, 90

[97] LM Barkov, DA Melik-Pashayev, and MS Zolotorev. Nonlinear faraday rotation in samarium vapor. *Optics communications*, 70(6):467–472, 1989. 23

[98] Vasily V Temnov, Gaspar Armelles, Ulrike Woggon, Dmitry Guzatov, Alfonso Cebollada, Antonio Garcia-Martin, Jose-Miguel Garcia-Martin, Tim Thomay, Alfred Leitenstorfer, and Rudolf Bratschitsch. Active magneto-plasmonics in hybrid metal–ferromagnet structures. *Nature Photonics*, 4(2):107, 2010. 23

[99] Jessie Yao Chin, Tobias Steinle, Thomas Wehlus, Daniel Dregely, Thomas Weiss, Vladimir I Belotelov, Bernd Stritzker, and Harald Giessen. Nonreciprocal plasmonics enables giant enhancement of thin-film faraday rotation. *Nature communications*, 4:1599, 2013. 23

[100] Wei Zheng, Xiao Liu, Aubrey T Hanbicki, Berend T Jonker, and Gunter Lüpke. Nonlinear magneto-plasmonics. *Optical Materials Express*, 5(11):2597–2607, 2015. 23

[101] DC Marinica, AK Kazansky, Peter Nordlander, Javier Aizpurua, and Andrei G Borisov. Quantum plasmonics: nonlinear effects in the field enhancement of a plasmonic nanoparticle dimer. *Nano letters*, 12(3):1333–1339, 2012. 23

[102] Krishna Prasad Koirala, Venkatanarayana Prasad Sandireddy, Hernando Garcia, Gerd Duscher, and Ramki Kalyanaraman. Nanosecond switchable localized

surface plasmonsthrough resettable contact angle behavior in silvernanoparticles. *Nanotechnology*, 2020. 23, 52, 64

[103] Yaqiong Qin, Xiaohui Ji, Jing Jing, Hong Liu, Hongli Wu, and Wensheng Yang. Size control over spherical silver nanoparticles by ascorbic acid reduction. *Colloids and Surfaces A: Physicochemical and Engineering Aspects*, 372(1-3):172–176, 2010. 24

[104] Srikanth Singamaneni, Valery N Bliznyuk, Christian Binek, and Evgeny Y Tsymbal. Magnetic nanoparticles: recent advances in synthesis, self-assembly and applications. *Journal of Materials Chemistry*, 21(42):16819–16845, 2011. 24

[105] Shangjr Gwo, Hung-Ying Chen, Meng-Hsien Lin, Liuyang Sun, and Xiaoqin Li. Nanomanipulation and controlled self-assembly of metal nanoparticles and nanocrystals for plasmonics. *Chemical Society Reviews*, 45(20):5672–5716, 2016. 24

[106] Beomseok Kim, Steven L Tripp, and Alexander Wei. Self-organization of large gold nanoparticle arrays. *Journal of the American Chemical Society*, 123(32):7955–7956, 2001. 24

[107] Bansi Dhar Malhotra and Md Azahar Ali. Nanomaterials in biosensors: fundamentals and applications. *Nanomaterials for Biosensors*, page 1, 2018. 24

[108] Minjoung Kyoung and Minyung Lee. Nonlinear absorption and refractive index measurements of silver nanorods by the z-scan technique. *Optics communications*, 171(1-3):145–148, 1999. 27, 86

[109] Carlos Torres-Torres, Néstor Peréa-López, Jorge Alejandro Reyes-Esqueda, Luis Rodríguez-Fernández, Alejandro Crespo-Sosa, Juan Carlos Cheang-Wong, and Alicia Oliver. Ablation and optical third-order nonlinearities in ag nanoparticles. *International journal of nanomedicine*, 5:925, 2010. 27, 86

[110] Baolong Yu, Congshan Zhu, Fuxi Gan, Xiaochum Wu, Guilan Zhang, Guoqing Tang, and Wenju Chen. Optical nonlinearities of fe2o3 nanoparticles investigated by z-scan technique. *Optical Materials*, 8(4):249–254, 1997. 27, 86

[111] Jérémy Butet, TV Raziman, Kuang-Yu Yang, Gabriel D Bernasconi, and Olivier JF Martin. Controlling the nonlinear optical properties of plasmonic nanoparticles with the phase of their linear response. *Optics express*, 24(15):17138–17148, 2016. 28

[112] Jérémy Butet and Olivier JF Martin. Fano resonances in the nonlinear optical response of coupled plasmonic nanostructures. *Optics express*, 22(24):29693–29707, 2014. 28

[113] Yong Zhang, Jing Jing Wang, Kyle E Ballantine, Paul R Eastham, and Werner J Blau. Hybrid plasmonic nanostructures with unconventional nonlinear optical properties. *Advanced Optical Materials*, 2(4):331–337, 2014. 28

[114] Niels Verellen, Pol Van Dorpe, Chengjun Huang, Kristof Lodewijks, Guy AE Vandenbosch, Liesbet Lagae, and Victor V Moshchalkov. Plasmon line shaping using nanocrosses for high sensitivity localized surface plasmon resonance sensing. *Nano letters*, 11(2):391–397, 2011. 28, 64

[115] Yang Tian and Tetsu Tatsuma. Mechanisms and applications of plasmon-induced charge separation at tio2 films loaded with gold nanoparticles. *Journal of the American Chemical Society*, 127(20):7632–7637, 2005. 28, 64

[116] Si Chen, Mikael Svedendahl, Mikael Käll, Linda Gunnarsson, and Alexandre Dmitriev. Ultrahigh sensitivity made simple: nanoplasmonic label-free biosensing with an extremely low limit-of-detection for bacterial and cancer diagnostics. *Nanotechnology*, 20(43):434015, 2009. 28, 64

[117] Koray Aydin, Vivian E Ferry, Ryan M Briggs, and Harry A Atwater. Broadband polarization-independent resonant light absorption using ultrathin plasmonic super absorbers. *Nature communications*, 2:517, 2011. 28, 64

[118] Krishna Prasad Koirala, Jingxuan Ge, Ramki Kalyanaraman, and Gerd Duscher. Direct detection of highly localized metal-metal interface plasmons from bimetallic nanoparticles. *Plasmonics*, pages 1–8, 2021. 28, 51

[119] Tian Ming, Lei Zhao, Manda Xiao, and Jianfang Wang. Resonance-coupling-based plasmonic switches. *Small*, 6(22):2514–2519, 2010. 29, 65

[120] Ann Katrin U Michel, Dmitry N Chigrin, Tobias WW Mas, Kathrin Schonauer, Martin Salinga, Matthias Wuttig, and Thomas Taubner. Using low-loss phase-change materials for mid-infrared antenna resonance tuning. *Nano letters*, 13(8):3470–3475, 2013. 29, 65

[121] Ann-Katrin U Michel, Peter Zalden, Dmitry N Chigrin, Matthias Wuttig, Aaron M Lindenberg, and Thomas Taubner. Reversible optical switching of infrared antenna resonances with ultrathin phase-change layers using femtosecond laser pulses. *ACS Photonics*, 1(9):833–839, 2014. 29, 65

[122] Yiding Liu, Xiaogang Han, Le He, and Yadong Yin. Thermoresponsive assembly of charged gold nanoparticles and their reversible tuning of plasmon coupling. *Angewandte Chemie International Edition*, 51(26):6373–6377, 2012. 29, 65

[123] Weilu Gao, Gang Shi, Zehua Jin, Jie Shu, Qi Zhang, Robert Vajtai, Pulickel M Ajayan, Junichiro Kono, and Qianfan Xu. Excitation and active control of propagating surface plasmon polaritons in graphene. *Nano letters*, 13(8):3698–3702, 2013. 29, 65

[124] S Debrus, J Lafait, M May, N Pinçon, D Prot, C Sella, and J Venturini. Z-scan determination of the third-order optical nonlinearity of gold: silica nanocomposites. *Journal of Applied Physics*, 88(8):4469–4475, 2000. 29

[125] HH Abu-Safe, R Al-Esseili, M Sarollahi, M Refaei, H Naseem, M Zamani-Alavijeh, T AlAbdulaal, and ME Ware. Thermally-induced nonlinear optical properties of silver nano-films near surface plasmon resonance. *Optical Materials*, 105:109858, 2020. 29

[126] Promod Kumar, Mohan Chandra Mathpal, Jai Prakash, Gangareddy Jagannath, WD Roos, and HC Swart. Plasmonic and nonlinear optical behavior of nanostructures in glass matrix for photonics application. *Materials Research Bulletin*, 125:110799, 2020. 29

[127] Junhong Deng, Yutao Tang, Shumei Chen, Kingfai Li, Anatoly V Zayats, and Guixin Li. Giant enhancement of second-order nonlinearity of epsilon-near-zero medium by a plasmonic metasurface. *Nano Letters*, 20(7):5421–5427, 2020. 29

[128] Xia Wang, Linhua Yao, Sen Li, and Menghao Cai. Extraordinarily large third-order optical nonlinearity in au nanorods under nanowatt laser excitation. *The Journal of Physical Chemistry C*, 124(12):6838–6844, 2020. 29

[129] Nadia Mattiucci, Giuseppe D'Aguanno, and Mark J Bloemer. Long range plasmon assisted all-optical switching at telecommunication wavelengths. *Optics letters*, 37(2):121–123, 2012. 29

[130] Yi Chen and Chong Han. Channel modeling and analysis for wireless networks-on-chip communications in the millimeter wave and terahertz bands. In *IEEE INFOCOM 2018-IEEE Conference on Computer Communications Workshops (INFOCOM WKSHPS)*, pages 651–656. IEEE, 2018. 30

[131] Evelyn L Hu, Mark Brongersma, and Adra Baca. Applications: nanophotonics and plasmonics. In *Nanotechnology Research Directions for Societal Needs in 2020*, pages 417–444. Springer, 2011. 30

[132] John F O'Hara, Sabit Ekin, Wooyeol Choi, and Ickhyun Song. A perspective on terahertz next-generation wireless communications. *Technologies*, 7(2):43, 2019. 30

[133] Christopher C Davis and Thomas E Murphy. Fiber-optic communications. *IEEE Signal Processing Magazine*, 28(4):147–150, 2011. 30

[134] Song-Jin Im, Chol-Song Ri, Kum-Song Ho, and Joachim Herrmann. Third-order nonlinearity by the inverse faraday effect in planar magnetoplasmonic structures. *Physical Review B*, 96(16):165437, 2017. 30

[135] Stanislav Kolodny, Dmitry Yudin, and Ivan Iorsh. Resonant spin wave excitation in magnetoplasmonic bilayers using short laser pulses. *Nanoscale*, 11(4):2003–2007, 2019. 30

[136] Ryan Freeman, Robert Lemasters, Tomi Kalejaiye, Feng Wang, Guanxiong Chen, Jinjun Ding, Mingzhong Wu, Vladislav E Demidov, Sergej O Demokritov, Hayk Harutyunyan, et al. Brillouin light scattering of spin waves inaccessible with free-space light. *Physical Review Research*, 2(3):033427, 2020. 30

[137] CA Foss. Gabor, jr.; hornyak, l.; stockert, ja; martin. *J. Phys. Chem*, 98:2963, 1994. 31

[138] VP Sandireddy, KP Koirala, and R Kalyanaraman. In-situ contact angle tuning of silver nanostructures by laser heating in different fluid ambient. *Langmuir: the ACS journal of surfaces and colloids*, 2019. 32, 39, 67, 72

[139] Michael D Abràmoff, Paulo J Magalhães, and Sunanda J Ram. Image processing with imagej. *Biophotonics international*, 11(7):36–42, 2004. 41

[140] David Nečas and Petr Klapetek. Gwyddion: an open-source software for spm data analysis. *Open Physics*, 10(1):181–188, 2012. 41

[141] Michael J McClain, Andrea E Schlather, Emilie Ringe, Nicholas S King, Lifei Liu, Alejandro Manjavacas, Mark W Knight, Ish Kumar, Kenton H Whitmire, Henry O Everitt, et al. Aluminum nanocrystals. *Nano letters*, 15(4):2751–2755, 2015. 43

[142] J Frey, Robert Frey, Christopher Flytzanis, and R Triboulet. Theoretical and experimental investigation of nonlinear faraday processes in diluted magnetic semiconductors. *JOSA B*, 9(1):132–142, 1992. 48, 90

[143] Matthew J Kale and Phillip Christopher. Plasmons at the interface. *Science*, 349(6248):587–588, 2015. 52

[144] Shijing Tan, Adam Argondizzo, Jindong Ren, Liming Liu, Jin Zhao, and Hrvoje Petek. Plasmonic coupling at a metal/semiconductor interface. *Nature Photonics*, 11(12):806–812, 2017. 52

[145] Chuancheng Jia, Xinxi Li, Na Xin, Yao Gong, Jianxin Guan, Linan Meng, Sheng Meng, and Xuefeng Guo. Interface-engineered plasmonics in metal/semiconductor heterostructures. *Advanced Energy Materials*, 6(17):1600431, 2016. 52

[146] MA Noginov, G Zhu, M Bahoura, J Adegoke, CE Small, BA Ritzo, VP Drachev, and Vladimir M Shalaev. Enhancement of surface plasmons in an ag aggregate by optical gain in a dielectric medium. *Optics letters*, 31(20):3022–3024, 2006. 52

[147] Cheng Sun. On the plasmonic properties of ag@ sio 2@ graphene core-shell nanostructures. *Plasmonics*, 13(5):1671–1680, 2018. 52

[148] Jun Wang, Gang Wang, and Changlong Liu. Plasmonic behaviors of two-dimensional ag/sio 2 nanocomposite gratings: Roles of gap diffraction and localized surface plasmon resonance absorption. *Plasmonics*, 14(4):921–928, 2019. 52

[149] Yuko Tachibana, Kouji Kusunoki, and Hisashi Ohsaki. Optical properties of ag/dielectric-material multilayers. *Vacuum*, 74(3-4):555–559, 2004. 52

[150] Nianqiang Wu. Plasmonic metal–semiconductor photocatalysts and photoelectrochemical cells: a review. *Nanoscale*, 10(6):2679–2696, 2018. 52

[151] Xinyu Huang, Hongbo Li, Chunfeng Zhang, Shijing Tan, Zhangzhang Chen, Lan Chen, Zhenda Lu, Xiaoyong Wang, and Min Xiao. Efficient plasmon-hot electron conversion in ag–cspbbr 3 hybrid nanocrystals. *Nature communications*, 10(1):1–8, 2019. 52

[152] Ali Sobhani, Mark W Knight, Yumin Wang, Bob Zheng, Nicholas S King, Lisa V Brown, Zheyu Fang, Peter Nordlander, and Naomi J Halas. Narrowband photodetection in the near-infrared with a plasmon-induced hot electron device. *Nature communications*, 4(1):1–6, 2013. 52

[153] Jian Zhu. Surface plasmon resonance from bimetallic interface in au–ag core–shell structure nanowires. *Nanoscale research letters*, 4(9):977, 2009. 52

[154] P Jewsbury and P Summerside. The nature of interface plasmon modes at bimetallic junctions. *Journal of Physics F: Metal Physics*, 10(4):645, 1980. 52

[155] Chao Zhang, Bao-Qin Chen, Zhi-Yuan Li, Younan Xia, and Yue-Gang Chen. Surface plasmon resonance in bimetallic core–shell nanoparticles. *The Journal of Physical Chemistry C*, 119(29):16836–16845, 2015. 52

[156] Donald F Swinehart. The beer-lambert law. *Journal of chemical education*, 39(7):333, 1962. 54

[157] H Krishna, R Sachan, J Strader, C Favazza, Mikhail Khenner, and Ramki Kalyanaraman. Thickness-dependent spontaneous dewetting morphology of ultrathin ag films. *Nanotechnology*, 21(15):155601, 2010. 54

[158] Xiaotong Liu, Dabing Li, Xiaojuan Sun, Zhiming Li, Hang Song, Hong Jiang, and Yiren Chen. Tunable dipole surface plasmon resonances of silver nanoparticles by cladding dielectric layers. *Scientific reports*, 5:12555, 2015. 54

[159] Yueying Wu, Guoliang Li, Charles Cherqui, Nicholas W Bigelow, Niket Thakkar, David J Masiello, Jon P Camden, and Philip D Rack. Electron energy loss spectroscopy study of the full plasmonic spectrum of self-assembled au–ag alloy nanoparticles: Unraveling size, composition, and substrate effects. *ACS Photonics*, 3(1):130–138, 2016. 54, 58

[160] Ai Leen Koh, Kui Bao, Imran Khan, W Ewen Smith, Gerald Kothleitner, Peter Nordlander, Stefan A Maier, and David W McComb. Electron energy-loss spectroscopy (eels) of surface plasmons in single silver nanoparticles and dimers: influence of beam damage and mapping of dark modes. *ACS nano*, 3(10):3015–3022, 2009. 54, 61

[161] Yasuhiro Takashimizu and Maiko Iiyoshi. New parameter of roundness r: circularity corrected by aspect ratio. *Progress in Earth and Planetary Science*, 3(1):2, 2016. 55

[162] Toon Coenen, David T Schoen, Benjamin JM Brenny, Albert Polman, and Mark L Brongersma. Combined electron energy-loss and cathodoluminescence spectroscopy on individual and composite plasmonic nanostructures. *Physical Review B*, 93(19):195429, 2016. 58

[163] Minho Kim, Mouhong Lin, Jiwoong Son, Hongxing Xu, and Jwa-Min Nam. Hot-electron-mediated photochemical reactions: Principles, recent advances, and challenges. *Advanced Optical Materials*, 5(15):1700004, 2017. 61

[164] Anne-Laure Baudrion, Antoine Perron, Alessandro Veltri, Alexandre Bouhelier, Pierre-Michel Adam, and Renaud Bachelot. Reversible strong coupling in silver nanoparticle arrays using photochromic molecules. *Nano letters*, 13(1):282–286, 2012. 64

[165] Feng Hao, Peter Nordlander, Yannick Sonnefraud, Pol Van Dorpe, and Stefan A Maier. Tunability of subradiant dipolar and fano-type plasmon resonances in metallic ring/disk cavities: implications for nanoscale optical sensing. *ACS nano*, 3(3):643–652, 2009. 64

[166] Hen Dotan, Ofer Kfir, Elad Sharlin, Oshri Blank, Moran Gross, Irina Dumchin, Guy Ankonina, and Avner Rothschild. Resonant light trapping in ultrathin films for water splitting. *Nature materials*, 12(2):158, 2013. 64

[167] Scott K Cushing, Jiangtian Li, Fanke Meng, Tess R Senty, Savan Suri, Mingjia Zhi, Ming Li, Alan D Bristow, and Nianqiang Wu. Photocatalytic activity enhanced by plasmonic resonant energy transfer from metal to semiconductor. *Journal of the American Chemical Society*, 134(36):15033–15041, 2012. 64

[168] Robert J Walters, Rob VA van Loon, Ihor Brunets, Jurriaan Schmitz, and Albert Polman. A silicon-based electrical source of surface plasmon polaritons. *Nature materials*, 9(1):21, 2010. 64

[169] Pieter Neutens, Liesbet Lagae, Gustaaf Borghs, and Pol Van Dorpe. Electrical excitation of confined surface plasmon polaritons in metallic slot waveguides. *Nano letters*, 10(4):1429–1432, 2010. 64

[170] Martin G Blaber, Anne-Isabelle Henry, Julia M Bingham, George C Schatz, and Richard P Van Duyne. Lspr imaging of silver triangular nanoprisms: correlating scattering with structure using electrodynamics for plasmon lifetime analysis. *The Journal of Physical Chemistry C*, 116(1):393–403, 2011. 64

[171] Evan L Runnerstrom, Anna Llordés, Sebastien D Lounis, and Delia J Milliron. Nanostructured electrochromic smart windows: traditional materials and nir-selective plasmonic nanocrystals. *Chemical communications*, 50(73):10555–10572, 2014. 64

[172] Justin Elser, Robyn Wangberg, Viktor A Podolskiy, and Evgenii E Narimanov. Nanowire metamaterials with extreme optical anisotropy. *Applied physics letters*, 89(26):261102, 2006. 65

[173] Hernando Garcia, Ritesh Sachan, and Ramki Kalyanaraman. Optical plasmon properties of co-ag nanocomposites within the mean-field approximation. *Plasmonics*, 7(1):137–141, 2012. 65

[174] Anil Kumar Pal and D Bharathi Mohan. Sers enhancement, sensitivity and homogeneity studies on bi-metallic ag-cu films through tuning of broad band spr towards red region. *Journal of Alloys and Compounds*, 698:460–468, 2017. 65

[175] Gabor L Hornyak, Charles J Patrissi, and Charles R Martin. Fabrication, characterization, and optical properties of gold nanoparticle/porous alumina composites: The nonscattering maxwell- garnett limit. *The Journal of Physical Chemistry B*, 101(9):1548–1555, 1997. 66

[176] Caroline A Schneider, Wayne S Rasband, and Kevin W Eliceiri. Nih image to imagej: 25 years of image analysis. *Nature methods*, 9(7):671, 2012. 68

[177] Ari Sihvola. Dielectric polarization and particle shape effects. *Journal of Nanomaterials*, 2007(1):5–5, 2007. 70

[178] JN Israelachvili. Intermolecular and surface forces, rev 3rd ed, 2011. 72

[179] Anil Kumar Pal and D Bharathi Mohan. Structural, morphological and optical properties of ag–ago thin films with the effect of increasing film thickness and annealing temperature. *Optical Materials*, 48:121–132, 2015. 74

[180] Oleksandr Zhuromskyy. Applicability of effective medium approximations to modelling of mesocrystal optical properties. *Crystals*, 7(1):1, 2017. 76

[181] Xin Tang, Zhong-Sheng Chen, Yue Li, Zheng Hu, and Yong-Min Yang. Analysis of the dynamic sensitivity of hemisphere-shaped electrostatic sensor's circular array for charged particle monitoring. *Sensors*, 16(9):1403, 2016. 78

[182] Edgar Rueda, Juan H Serna, Abdullatif Hamad, and Hernando Garcia. Two-photon absorption coefficient determination using the differential f-scan technique. *Optics & Laser Technology*, 119:105584, 2019. 84

[183] Juan Serna, Julián Henao, Edgar Rueda, Abdullatif Hamad, and Hernando Garcia. Reflection technique for determination of nonlinear-refractive index of thin-film semiconductors using an electrically focus-tunable lens. In *Frontiers in Optics*, pages JW4A–12. Optical Society of America, 2019. 84

[184] H Garcia, J Serna, and E Rueda. Bulk znse and cds two-photon absorption measurement with an f-scan nonlinear absorption spectrometer. *OSA Continuum*, 3(3):498–504, 2020. 84

[185] Chol-Song Ri, Song-Jin Im, Ji-Song Pae, Kum-Song Ho, Yong-Ha Han, and Joachim Herrmann. Nanoscale magnetization and third-order nonlinearity by the plasmon-induced inverse faraday effect in graphene-covered semiconductors. *Physical Review B*, 100(15):155404, 2019. 90

[186] Y Tokura. Multiferroics toward strong coupling between magnetization and polarization in a solid. *Journal of Magnetism and Magnetic Materials*, 310(2):1145–1150, 2007. 90

[187] Alexey V Krasavin, Pavel Ginzburg, and Anatoly V Zayats. Free-electron optical nonlinearities in plasmonic nanostructures: A review of the hydrodynamic description. *Laser & Photonics Reviews*, 12(1):1700082, 2018. 91

[188] Akio Kawasaki, Boris Braverman, Edwin Pedrozo-Peñafiel, Chi Shu, Simone Colombo, Zeyang Li, Özge Özel, Wenlan Chen, Leonardo Salvi, André Heinz, et al. Geometrically asymmetric optical cavity for strong atom-photon coupling. *Physical Review A*, 99(1):013437, 2019. 91

[189] Yuri Kivshar. Engineered metaoptics forge new nonlinear devices. *LASER FOCUS WORLD*, 55(3):39–41, 2019. 91

[190] Kishore Sridharan, Tamio Endo, Sang-Geun Cho, Jongryoul Kim, Tae Joo Park, and Reji Philip. Single step synthesis and optical limiting properties of ni–ag and fe–ag bimetallic nanoparticles. *Optical Materials*, 35(5):860–867, 2013. 91

[191] OV Prikhodko, OS Sukhorukova, SV Tarasenko, and VG Shavrov. Evanescent wave intensification in surface spin-wave acoustics and magnetic/nonmagnetic interface electrodynamics. *Bulletin of the Russian Academy of Sciences: Physics*, 79(6):712–714, 2015. 91

[192] Henri J Lezec and Tineke Thio. Diffracted evanescent wave model for enhanced and suppressed optical transmission through subwavelength hole arrays. *Optics express*, 12(16):3629–3651, 2004. 91

[193] Evangelos Th Papaioannou, Hui Fang, Blanca Caballero, Eser Metin Akinoglu, Michael Giersig, Antonio García-Martín, and Paul Fumagalli. Role of interactions in the magneto-plasmonic response at the geometrical threshold of surface continuity. *Optics Express*, 25(26):32792–32799, 2017. 92

Vita

Krishna Prasad Koirala was born in rural district of Nepal, Syangja, on December 19, 1988, the son of Mrs. Radhika Koirala and Mr. Narayan Prasad Koirala. He received degree for Master of Science in physics from Tribhuvan University, Nepal, in the year 2015. In the Fall of 2015, he joined the doctoral program in Department of Physics and Astronomy in the University of Tennessee, Knoxville.